Geophys. J. Int. (2008) **175,** 301–345 doi: 10.1111/j.1365-246X.2008.03907.x

Spectral-element simulations of wave propagation in porous media

Christina Morency* and Jeroen Tromp*

Seismological Laboratory, California Institute of Technology, Pasadena, CA 91125, *USA. E-mail: cmorency@gps.caltech.edu*

Accepted 2008 June 29. Received 2008 June 27; in original form 2008 January 7

SUMMARY

We present a derivation of the equations describing wave propagation in porous media based upon an averaging technique which accommodates the transition from the microscopic to the macroscopic scale. We demonstrate that the governing macroscopic equations determined by Biot remain valid for media with gradients in porosity. In such media, the well-known expression for the change in porosity, or the change in the fluid content of the pores, acquires two extra terms involving the porosity gradient. One fundamental result of Biot's theory is the prediction of a second compressional wave, often referred to as 'type II' or 'Biot's slow compressional wave', in addition to the classical fast compressional and shear waves. We present a numerical implementation of the Biot equations for 2-D problems based upon the spectral-element method (SEM) that clearly illustrates the existence of these three types of waves as well as their interactions at discontinuities. As in the elastic and acoustic cases, poroelastic wave propagation based upon the SEM involves a diagonal mass matrix, which leads to explicit time integration schemes that are well suited to simulations on parallel computers. Effects associated with physical dispersion and attenuation and frequency-dependent viscous resistance are accommodated based upon a memory variable approach. We perform various benchmarks involving poroelastic wave propagation and acoustic–poroelastic and poroelastic–poroelastic discontinuities, and we discuss the boundary conditions used to deal with these discontinuities based upon domain decomposition. We show potential applications of the method related to wave propagation in compacted sediments, as one encounters in the petroleum industry, and to detect the seismic signature of buried landmines and unexploded ordnance.

Key words: Computational seismology; Theoretical seismology; Wave propagation.

1 INTRODUCTION

Poromechanics was born in the 1920s with Terzaghi (1923, 1943), a civil engineer, whose concept of effective stress for 1-D porous deformation and its influence on settlement analysis, strength, permeability and erosion of soils, marks the beginning of the engineering branch of Soil Mechanics. Terzaghi's effective stress principle mathematically articulates that the pore fluid bears part of the load applied to a column. The effective stress acting on the soil-solid skeleton is the difference between the total stress and the pore fluid pressure. But it is Biot (1941) who formulated the 3-D theory of soil consolidation, which is nowadays known as the Biot theory of poroelasticity. Subsequently, Biot incorporated inertial terms into the analysis to develop the theory of wave propagation in a fluid-saturated porous medium (Biot 1956a,b, 1962a,b). Biot theory has been extensively used in the petroleum industry, where seismic surveys are performed to determine the physical properties of reservoir rocks. The theory is of broad, general interest when a physical understanding of the coupling between solid and fluid phases is desired.

One fundamental result of Biot theory is the prediction of a second compressional wave, which may attenuate rapidly due to viscous damping, generally referred to as 'type II' or 'Biot's slow compressional wave', in addition to the classical fast compressional and shear waves, confirming the results of Frenkel (1944). Indeed, Frenkel was actually the first to investigate wave propagation in fluid saturated porous media in his study of seismoelectric waves, and to demonstrate the existence of two compressional waves, one characterized by in-phase movement between the solid and the fluid (fast), and the other one by out-of-phase movement (slow). However, Frenkel neglected some aspects compared to the more accepted theory developed by Biot (see Pride 2003; Smeulders 2005, for a more in-depth discussion).

*Now at: Department of Geosciences, Princeton University, Princeton, NJ 08544, USA.

It was only in the 1980s that Biot and Frenkel's prediction of the existence of a slow compressional wave was clearly observed experimentally by Plona (1980) for water-saturated sintered glass beads at ultrasonic frequencies (500 kHz to 2.25 MHz). Experiments at low frequencies (e.g. Van der Grinten *et al.* 1985, for both air and water as pore constituents) and in the limit of zero frequency (e.g. Chandler 1981; Chandler & Johnson 1981) followed. At high frequencies, the first report of a slow compressional wave in water-saturated natural rock is due to Kelder & Smeulders (1997). All these experiments are in good agreement with the theory.

The behaviour of the slow compressional wave is highly frequency-dependent. At low frequencies, the fluid flow in the pores is of Poiseuille type, where viscous forces dominate the flow. In this case, the slow compressional wave behaves like a diffusion phenomenon and is highly attenuated (Biot 1956a). At high frequencies, inertial forces dominate the flow and the slow compressional wave propagates, still exhibiting high attenuation (Biot 1956b). Wave attenuation mechanisms originate from the motion of pore fluid relative to the solid skeleton in the form of viscous and inertial dissipation (Biot 1962b). Geertsma & Smit (1961) also point out the attenuation of the fast compressional wave at low frequencies through mode conversion at discontinuities.

Biot developed his theory based upon the principle of virtual work, ignoring processes at the microscopic level. Moreover, even if the Biot (1962a,b) formulations are claimed to be valid for non-uniform porosity, gradients in porosity are not explicitly incorporated in the original theory. More recent studies focused on averaging techniques (e.g. Whitaker 1999) to derive the macroscopic porous medium equations from the microscale, and made an attempt to derive an expression for the change in porosity (e.g. Pride *et al.* 1992; Sahay *et al.* 2001), but there is still room for clarification of such an expression, and to properly integrate the effects of porosity gradients.

Throughout this paper we aim to present a straightforward derivation of the main equations describing wave propagation in poroelastic media, with a particular emphasis on the effects of gradients in porosity. To that end, we will work with the linearized equations of motion, both at the microscopic and the macroscopic scale. In Section 2, we recall the microscale equations in the solid and the fluid. The macroscopic equations for porous media are derived in Section 4 using the averaging principle described in Section 3. Section 5 is dedicated to two simple cases, the static problem and Darcy flow, to develop some intuition for the form of the 'drag force' arising from porosity gradients. In Section 6, we determine a macroscopic expression for the 'interfacial strain' and present a complete expression for the change in porosity. In Section 7, we use a Gedanken experiment to constrain the remaining unknowns present in the interfacial strain formulation, thus obtaining the complete poroelastic constitutive relationships. The macroscopic equations of motion are presented in Section 8, where we consider implementations with and without frequency-dependent dissipation. In particular, we consider the effects of physical dispersion and attenuation, as well as frequency-dependent viscous resistance. Finally, we summarize the full set of macroscopic equations for the problem of wave propagation in porous media and express the various wave speeds in such complex media in Sections 9 and 10.

In Section 11, we describe a numerical implementation of wave propagation in porous media. First, we establish the weak form of the governing equations. Next, we determine the spatial discretization of this variational problem using a spectral-element method (SEM) (Komatitsch 1997; Komatitsch & Tromp 1999). As in a finite-element method (FEM), the mesh represents a subdivision of the model volume in terms of a number of finite elements, at which level the problem is approximated. The difference between a FEM and a SEM lies in the use of higher-degree Lagrange polynomials to interpolate functions on the elements. As a result, the SEM retains the ability of a FEM to handle complex geometries while keeping the strength of exponential convergence and accuracy resulting from the use of high-degree polynomials (e.g. Chaljub *et al.* 2007; De Basabe & Sen 2007). We will see that, as for acoustic and elastic problems, the combination of Lagrange interpolation with Gauss–Lobatto–Legendre (GLL) quadrature leads to a diagonal mass matrix, and thus to fully explicit time integration schemes.

In Section 13, we present 2-D benchmarks to support our implementation. The first benchmark is a simple test of wave propagation in a homogeneous porous medium, using an explosive source. As expected by the theory, we observe two types of compressional waves. The numerical solution is compared to an analytical solution derived by Dai *et al.* (1995) and shows excellent agreement. For subsequent benchmarks we focus on more complex media and discuss the boundary conditions at acoustic–poroelastic and poroelastic–poroelastic discontinuities. In each case, we use a domain decomposition technique to ensure the continuity of traction and displacement at an interface involving only (poro)elastic media, and the continuity of traction and the normal component of displacement at an interface involving a fluid. Finally, in Section 14 we present sample applications of potential interest for modelling wave propagation in compacted sediments, for example, in petroleum industry settings or for the detection of buried landmines and unexploded ordnance.

2 MICROSCOPIC EQUATIONS OF MOTION

We begin by summarizing the microscopic equations of motion in the solid and the fluid. The reader is referred to Aki & Richards (1980) and Carcione (2007) for a detailed introduction to seismic wave propagation. In subsequent sections we will average these microscopic equations to obtain a macroscopic description of wave propagation in porous media.

2.1 Solid

Microscopic conservation of mass in the solid is governed by the continuity equation

$$\partial_t \rho_s + \boldsymbol{\nabla} \cdot (\rho_s \mathbf{v}_s) = 0, \tag{1}$$

where ρ_s denotes the density of the solid, and $\mathbf{v}_s = \partial_t \mathbf{u}_s$ its velocity. Linearized microscopic conservation of momentum in the solid is determined by

$$\rho_s \partial_t \mathbf{v}_s = \boldsymbol{\nabla} \cdot \mathbf{T}_s. \tag{2}$$

The microscopic solid stress tensor $\mathbf{T}_s$ is related to the microscopic solid strain tensor $\boldsymbol{\epsilon}_s$ through the fourth-order elastic tensor $\mathbf{c}_s$ via Hooke's law

$$\mathbf{T}_s = \mathbf{c}_s : \boldsymbol{\epsilon}_s. \tag{3}$$

The solid strain tensor may be expressed in terms of its isotropic and deviatoric parts as

$$\boldsymbol{\epsilon}_s = \frac{1}{2}\left[\boldsymbol{\nabla}\mathbf{u}_s + (\boldsymbol{\nabla}\mathbf{u}_s)^T\right] = \frac{1}{3}(\boldsymbol{\nabla}\cdot\mathbf{u}_s)\mathbf{I} + \mathbf{d}_s, \tag{4}$$

where $\mathbf{I}$ denotes the identity tensor and $\mathbf{d}_s$ the solid strain deviator

$$\mathbf{d}_s = \frac{1}{2}\left[\boldsymbol{\nabla}\mathbf{u}_s + (\boldsymbol{\nabla}\mathbf{u}_s)^T\right] - \frac{1}{3}(\boldsymbol{\nabla}\cdot\mathbf{u}_s)\mathbf{I}, \tag{5}$$

and a superscript T denotes the transpose.

In an isotropic solid characterized by a bulk modulus κ_s and a shear modulus μ_s the components of the elastic tensor $\mathbf{c}_s$ may be expressed as

$$c^s_{ijkl} = (\kappa_s - {}^2/_3\mu_s)\delta_{ij}\delta_{kl} + \mu_s(\delta_{ik}\delta_{jl} + \delta_{il}\delta_{jk}), \tag{6}$$

and the constitutive relationship (3) becomes

$$\mathbf{T}_s = \kappa_s(\boldsymbol{\nabla}\cdot\mathbf{u}_s)\mathbf{I} + 2\mu_s\mathbf{d}_s. \tag{7}$$

2.2 Fluid

Microscopic conservation of mass in the fluid is governed by the continuity equation

$$\partial_t \rho_f + \boldsymbol{\nabla}\cdot(\rho_f \mathbf{v}_f) = 0, \tag{8}$$

where ρ_f denotes the density of the fluid, and $\mathbf{v}_f = \partial_t \mathbf{u}_f$ its velocity. Linearized microscopic conservation of momentum in the fluid is determined by

$$\rho_f \partial_t \mathbf{v}_f = \boldsymbol{\nabla}\cdot\mathbf{T}_f. \tag{9}$$

The microscopic fluid constitutive relationship is determined by linearized compressible Navier–Stokes theory:

$$\mathbf{T}_f = \kappa_f(\boldsymbol{\nabla}\cdot\mathbf{u}_f)\mathbf{I} + 2\eta_f\partial_t\mathbf{d}_f, \tag{10}$$

where κ_f denotes the bulk modulus of the fluid, η_f its viscosity, and $\partial_t\mathbf{d}_f$ its deviatoric strain rate

$$\partial_t\mathbf{d}_f = \frac{1}{2}\left[\boldsymbol{\nabla}\mathbf{v}_f + (\boldsymbol{\nabla}\mathbf{v}_f)^T\right] - \frac{1}{3}(\boldsymbol{\nabla}\cdot\mathbf{v}_f)\mathbf{I}. \tag{11}$$

It will sometimes be convenient to introduce the fourth-order operator $\mathbf{c}_f$ with components

$$c^f_{ijkl} = \left(\kappa_f - {}^2/_3\eta_f\partial_t\right)\delta_{ij}\delta_{kl} + \eta_f\partial_t(\delta_{ik}\delta_{jl} + \delta_{il}\delta_{jk}), \tag{12}$$

such that we can write (10) in a form similar to (3):

$$\mathbf{T}_f = \mathbf{c}_f : \boldsymbol{\epsilon}_f, \tag{13}$$

where

$$\boldsymbol{\epsilon}_f = \frac{1}{2}\left[\boldsymbol{\nabla}\mathbf{u}_f + (\boldsymbol{\nabla}\mathbf{u}_f)^T\right] = \frac{1}{3}(\boldsymbol{\nabla}\cdot\mathbf{u}_f)\mathbf{I} + \mathbf{d}_f. \tag{14}$$

2.3 Boundary conditions

The fluid and solid are in contact at a fluid–solid interface Σ. Let $\hat{\mathbf{n}}$ denote the unit outward normal to the fluid–solid interface Σ, pointing from the solid to the fluid. At this interface both the microscopic tractions and displacements need to be continuous:

$$\hat{\mathbf{n}}\cdot\mathbf{T}_s = \hat{\mathbf{n}}\cdot\mathbf{T}_f \quad \text{on } \Sigma, \tag{15}$$

and

$$\mathbf{u}_s = \mathbf{u}_f \quad \text{on } \Sigma. \tag{16}$$

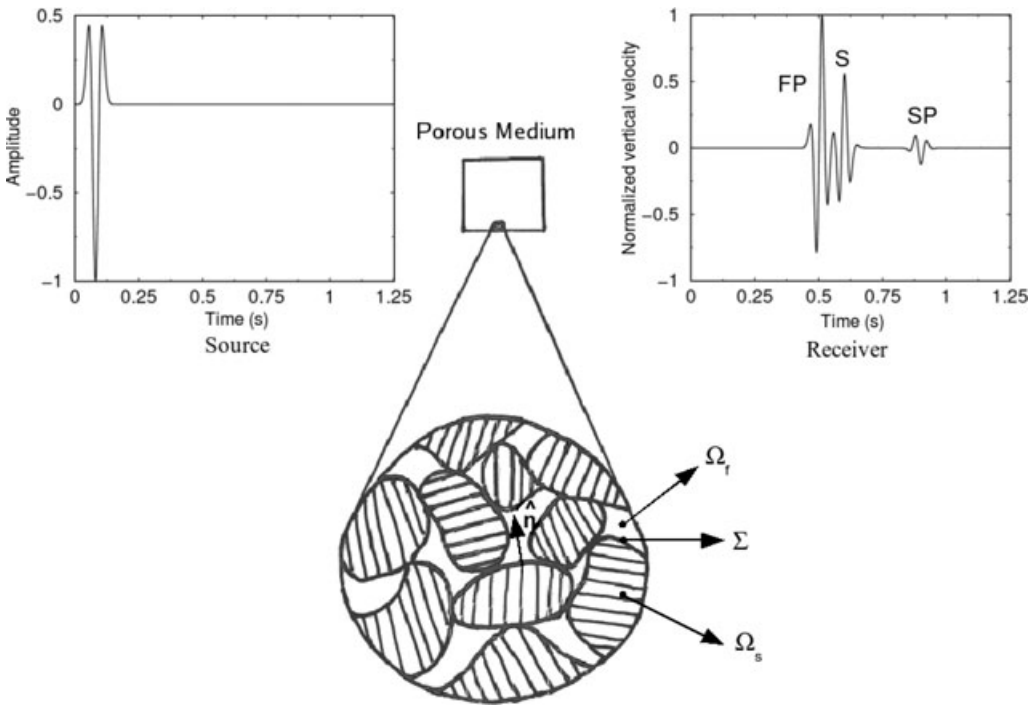

Figure 1. Schematic representation of the waves generated in a poroelastic material: FP denotes the fast compressional wave, *S* the shear wave and SP the slow compressional wave. Also shown is a schematic close-up of the porous medium with volume Ω, which may be subdivided in terms of its solid and fluid parts Ω_s and Ω_f, respectively. The microscopic fluid–solid boundary is denoted by Σ, and the unit normal to this boundary, pointing from the solid to the fluid, is denoted by $\hat{\mathbf{n}}$.

3 AVERAGING

Our next goal is to average the microscopic equations of motion discussed in the previous section to obtain the macroscopic equations of motion. To this end, we introduce formulae to average gradients and rates, which are operators appearing in the microscopic equations. Following Pride & Berryman (1998), we introduce a generic weight function $W(\mathbf{x}-\mathbf{x}')$, where $\mathbf{x}$ and $\mathbf{x}'$ denote position vectors in the porous medium. The function W has a value of one in the vicinity of $\mathbf{x}=\mathbf{x}'$ and monotonically decreases to zero at distances $\mathbf{x}'$ far from $\mathbf{x}$. The model volume Ω may be subdivided in terms of its solid and fluid parts Ω_s and Ω_f, respectively, such that $\Omega=\Omega_s\cup\Omega_f$ (Fig. 1). As already mentioned, the interface between the solid and fluid is denoted by Σ.

We now define the following volume measures of W:

$$V=\int_\Omega W(\mathbf{x}-\mathbf{x}')\,\mathrm{d}^3\mathbf{x}', \tag{17}$$

$$V_s(\mathbf{x})=\int_{\Omega_s} W(\mathbf{x}-\mathbf{x}')\,\mathrm{d}^3\mathbf{x}', \tag{18}$$

$$V_f(\mathbf{x})=\int_{\Omega_f} W(\mathbf{x}-\mathbf{x}')\,\mathrm{d}^3\mathbf{x}'. \tag{19}$$

Note that V is independent of $\mathbf{x}$ because W depends on the difference $\mathbf{x}-\mathbf{x}'$. Thus, the volume over which we average is fixed. Note also that

$$V=V_s(\mathbf{x})+V_f(\mathbf{x}). \tag{20}$$

3.1 Porosity

The porosity ϕ of the macroscopic medium is defined by

$$V_f(\mathbf{x})=\phi(\mathbf{x})V \quad \text{or} \quad V_s(\mathbf{x})=[1-\phi(\mathbf{x})]V. \tag{21}$$

Throughout this paper we will accommodate gradients in porosity, that is, we will not assume that the porosity is constant.

3.2 Volume average

Consider arbitrary microscopic tensor fields Ψ_s and Ψ_f defined in the solid or the fluid, respectively. Their volume averages are defined by

$$\langle\Psi_s\rangle(\mathbf{x}) = \frac{1}{V}\int_{\Omega_s} W(\mathbf{x}-\mathbf{x}')\Psi_s(\mathbf{x}')\,\mathrm{d}^3\mathbf{x}', \tag{22}$$

$$\langle\Psi_f\rangle(\mathbf{x}) = \frac{1}{V}\int_{\Omega_f} W(\mathbf{x}-\mathbf{x}')\Psi_f(\mathbf{x}')\,\mathrm{d}^3\mathbf{x}'. \tag{23}$$

3.3 Phase average

Alternatively, the phase averages of the fields Ψ_s and Ψ_f are defined by

$$\overline{\Psi}_s(\mathbf{x}) = \frac{1}{V_s(\mathbf{x})}\int_{\Omega_s} W(\mathbf{x}-\mathbf{x}')\Psi_s(\mathbf{x}')\,\mathrm{d}^3\mathbf{x}', \tag{24}$$

$$\overline{\Psi}_f(\mathbf{x}) = \frac{1}{V_f(\mathbf{x})}\int_{\Omega_f} W(\mathbf{x}-\mathbf{x}')\Psi_f(\mathbf{x}')\,\mathrm{d}^3\mathbf{x}'. \tag{25}$$

Using the definition of porosity (21), the phase averages (24) and (25) may be related to the volume averages (22) and (23):

$$\langle\Psi_s\rangle = (1-\phi)\overline{\Psi}_s, \qquad \langle\Psi_f\rangle = \phi\overline{\Psi}_f. \tag{26}$$

3.4 Averaging gradients

The gradient of the volume averages (22) and (23) is determined by

$$\begin{aligned}\boldsymbol{\nabla}\langle\Psi_p\rangle(\mathbf{x}) &= \frac{1}{V}\int_{\Omega_p}[\boldsymbol{\nabla}W(\mathbf{x}-\mathbf{x}')]\Psi_p(\mathbf{x}')\,\mathrm{d}^3\mathbf{x}'\\ &= -\frac{1}{V}\int_{\Omega_p}[\boldsymbol{\nabla}'W(\mathbf{x}-\mathbf{x}')]\Psi_p(\mathbf{x}')\,\mathrm{d}^3\mathbf{x}'\\ &= \frac{1}{V}\int_{\Omega_p} W(\mathbf{x}-\mathbf{x}')[\boldsymbol{\nabla}'\Psi_p(\mathbf{x}')]\,\mathrm{d}^3\mathbf{x}' - \frac{1}{V}\int_{\Omega_p}\boldsymbol{\nabla}'[W(\mathbf{x}-\mathbf{x}')\Psi_p(\mathbf{x}')]\,\mathrm{d}^3\mathbf{x}',\end{aligned} \tag{27}$$

where $\boldsymbol{\nabla}'$ denotes the gradient with respect to the $\mathbf{x}'$ coordinates. Thus, using (22) or (23) for the first term and the divergence theorem on the second term, we find

$$\boldsymbol{\nabla}\langle\Psi_p\rangle = \langle\boldsymbol{\nabla}\Psi_p\rangle - \frac{1}{V}\int_{\Sigma} W\hat{\mathbf{n}}'_p\Psi'_p\,\mathrm{d}^2\mathbf{x}', \tag{28}$$

where a subscript p can denote either s (solid) or f (fluid), a prime denotes evaluation at $\mathbf{x}'$, and $\hat{\mathbf{n}}_s = \hat{\mathbf{n}} = -\hat{\mathbf{n}}_f$ denotes the unit normal to the fluid–solid interface Σ, pointing from the solid to the fluid. (28) relates the gradient of the average, $\boldsymbol{\nabla}\langle\Psi_p\rangle$, to the average of the gradient, $\langle\boldsymbol{\nabla}\Psi_p\rangle$.

In terms of the phase averages $\overline{\Psi}_s$ and $\overline{\Psi}_f$, invoking (26), we have alternatively

$$\langle\boldsymbol{\nabla}\Psi_s\rangle = \boldsymbol{\nabla}[(1-\phi)\overline{\Psi}_s] + \frac{1}{V}\int_{\Sigma} W\hat{\mathbf{n}}'\Psi'_s\,\mathrm{d}^2\mathbf{x}', \tag{29}$$

$$\langle\boldsymbol{\nabla}\Psi_f\rangle = \boldsymbol{\nabla}(\phi\overline{\Psi}_f) - \frac{1}{V}\int_{\Sigma} W\hat{\mathbf{n}}'\Psi'_f\,\mathrm{d}^2\mathbf{x}', \tag{30}$$

similar to results obtained by Pride & Berryman (1998).

3.5 Averaging rates

For temporally and spatially variable fields $\Psi_p(\mathbf{x}, t)$, by analogy with the average of a gradient, $\langle\boldsymbol{\nabla}\Psi_p\rangle$, we may obtain the average of a rate, $\langle\partial_t\Psi_p\rangle$, as follows (Whitaker 1999):

$$\partial_t\langle\Psi_p\rangle = \langle\partial_t\Psi_p\rangle + \frac{1}{V}\int_{\Sigma} W\hat{\mathbf{n}}'_p\cdot\mathbf{v}'_p\Psi'_p\,\mathrm{d}^2\mathbf{x}', \tag{31}$$

where the second term accommodates advection of the fluid–solid interface Σ. Thus we obtain in terms of the phase averages $\overline{\Psi}_s$ and $\overline{\Psi}_f$

$$\langle\partial_t\Psi_s\rangle = \partial_t[(1-\phi)\overline{\Psi}_s] - \frac{1}{V}\int_{\Sigma} W\hat{\mathbf{n}}'\cdot\mathbf{v}'_s\Psi'_s\,\mathrm{d}^2\mathbf{x}', \tag{32}$$

$$\langle \partial_t \Psi_f \rangle = \partial_t (\phi \overline{\Psi}_f) + \frac{1}{V} \int_\Sigma W \hat{\mathbf{n}}' \cdot \mathbf{v}'_f \Psi'_f \, \mathrm{d}^2\mathbf{x}', \tag{33}$$

where we have recognized that for time-dependent problems the porosity may vary as a function of time due to relative changes in the solid and fluid volumes Ω_s and Ω_f.

We will use the averaging rules (29) and (30) and (32) and (33) to obtain the macroscopic equations of motion. Terms of the form $\partial_t \Psi_p + \boldsymbol{\nabla} \cdot (\Psi_p \mathbf{v}_p)$ frequently appear in the microscopic equations of continuum mechanics. Note that (29) and (32) imply that

$$\langle \partial_t \Psi_s \rangle + \langle \boldsymbol{\nabla} \cdot (\Psi_s \mathbf{v}_s) \rangle = \partial_t [(1-\phi)\overline{\Psi}_s] + \boldsymbol{\nabla} \cdot [(1-\phi)\overline{\Psi_s \mathbf{v}_s}], \tag{34}$$

and that (30) and (33) imply that

$$\langle \partial_t \Psi_f \rangle + \langle \boldsymbol{\nabla} \cdot (\Psi_f \mathbf{v}_f) \rangle = \partial_t (\phi \overline{\Psi}_f) + \boldsymbol{\nabla} \cdot (\phi \overline{\Psi_f \mathbf{v}_f}), \tag{35}$$

because the interfacial integrals cancel.

3.6 Spatial and temporal derivatives of porosity

The spatial and temporal averages (29) and (32) or (30) and (33) have immediate consequences for porosity. Upon taking the fields Ψ_s or Ψ_f to be constants, we find that the gradient of porosity is determined by

$$\boldsymbol{\nabla} \phi(\mathbf{x}, t) = \frac{1}{V} \int_{\Sigma_t} W(\mathbf{x} - \mathbf{x}') \hat{\mathbf{n}}(\mathbf{x}', t) \, \mathrm{d}^2\mathbf{x}', \tag{36}$$

whereas its temporal derivative is given by

$$\partial_t \phi(\mathbf{x}, t) = -\frac{1}{V} \int_{\Sigma_t} W(\mathbf{x} - \mathbf{x}') \hat{\mathbf{n}}(\mathbf{x}', t) \cdot \mathbf{v}_f(\mathbf{x}', t) \, \mathrm{d}^2\mathbf{x}'. \tag{37}$$

Strictly speaking, as the wavefield moves through the porous material the solid and fluid measures V_s and V_f vary with time, and so does the fluid–solid boundary Σ. So just for clarity, the subscript t on the surface Σ recognizes its temporal variation, as does the explicit dependence of the normal $\hat{\mathbf{n}}$ on t.

4 MACROSCOPIC EQUATIONS

To obtain the macroscopic equations of motion we will make two key assumptions.

(i) The microscopic material properties ρ_s, ρ_f, $\mathbf{c}_s$, κ_f and η_f are constant on the scale of the averaging volume V defined by (17), but these parameters may vary at the macroscale.

(ii) The wavelengths of the waves of interest are large compared to the averaging volume V. For example, for grain sizes on the order of 100 μm, the characteristic diameter of the averaging volume should be larger than 1000 μm, and the minimum wavelength of the waves should be on the order of 1 cm (Pride *et al.* 1992).

4.1 Conservation of mass

Upon applying the averaging rules (29) and (32) to the microscopic continuity equation (1), we obtain the macroscopic equation for the conservation of mass:

$$\partial_t [(1-\phi)\rho_s] + \boldsymbol{\nabla} \cdot [(1-\phi)\rho_s \overline{\mathbf{v}}_s] = 0. \tag{38}$$

This implies that

$$\partial_t \ln \rho_s + \overline{\mathbf{v}}_s \cdot \boldsymbol{\nabla} \ln \rho_s + \partial_t \ln(1-\phi) + \overline{\mathbf{v}}_s \cdot \boldsymbol{\nabla} \ln(1-\phi) + \boldsymbol{\nabla} \cdot \overline{\mathbf{v}}_s = 0. \tag{39}$$

Similarly, upon averaging the microscopic fluid continuity equation (8) based upon (30) and (33) we obtain

$$\partial_t (\phi \rho_f) + \boldsymbol{\nabla} \cdot (\phi \rho_f \overline{\mathbf{v}}_f) = 0, \tag{40}$$

which implies

$$\partial_t \ln \rho_f + \overline{\mathbf{v}}_f \cdot \boldsymbol{\nabla} \ln \rho_f + \partial_t \ln \phi + \overline{\mathbf{v}}_f \cdot \boldsymbol{\nabla} \ln \phi + \boldsymbol{\nabla} \cdot \overline{\mathbf{v}}_f = 0. \tag{41}$$

4.2 Constitutive relationships

Next, we need to average the constitutive relationships. Upon averaging the solid constitutive relation (3) based upon (29) we obtain

$$\langle \mathbf{T}_s \rangle = (1-\phi)\overline{\mathbf{T}}_s = \mathbf{c}_s : \langle \boldsymbol{\epsilon}_s \rangle, \tag{42}$$

where the averaged solid strain tensor is determined by

$$\langle \boldsymbol{\epsilon}_s \rangle = \frac{1}{2}[\langle \boldsymbol{\nabla} \mathbf{u}_s \rangle + \langle (\boldsymbol{\nabla} \mathbf{u}_s)^T \rangle] = \frac{1}{2}[\boldsymbol{\nabla} \langle \mathbf{u}_s \rangle + (\boldsymbol{\nabla} \langle \mathbf{u}_s \rangle)^T] + \mathbf{E}. \tag{43}$$

We have introduced the 'interfacial strain' tensor

$$\mathbf{E} = \frac{1}{V}\int_\Sigma W \frac{1}{2}(\hat{\mathbf{n}}'\mathbf{u}_s' + \mathbf{u}_s'\hat{\mathbf{n}}')\,\mathrm{d}^2\mathbf{x}'. \tag{44}$$

Note from (37) that

$$\mathrm{tr}(\mathbf{E}) = \frac{1}{V}\int_\Sigma W\hat{\mathbf{n}}'\cdot\mathbf{u}_s'\,\mathrm{d}^2\mathbf{x}' = -\Delta\phi \tag{45}$$

is the change in porosity. We may write the interfacial strain in terms of its isotropic and deviatoric parts as

$$\mathbf{E} = -\frac{1}{3}\Delta\phi\,\mathbf{I} + \mathbf{\Gamma}, \tag{46}$$

where $\mathbf{\Gamma}$ is the 'deviatoric interfacial strain'

$$\mathbf{\Gamma} = \frac{1}{V}\int_\Sigma W\left[\frac{1}{2}(\hat{\mathbf{n}}'\mathbf{u}_s' + \mathbf{u}_s'\hat{\mathbf{n}}') - \frac{1}{3}(\hat{\mathbf{n}}'\cdot\mathbf{u}_s')\mathbf{I}\right]\mathrm{d}^2\mathbf{x}'. \tag{47}$$

We thus have

$$(1-\phi)\overline{\mathbf{T}}_s = \mathbf{c}_s : \nabla[(1-\phi)\overline{\mathbf{u}}_s] + \mathbf{c}_s : \mathbf{E}. \tag{48}$$

In a later section we will seek to find an explicit expression for the interfacial strain $\mathbf{E}$ in terms of the macroscopic parameters.

Similarly, upon averaging the fluid constitutive relation (13) we obtain

$$\langle\mathbf{T}_f\rangle = \phi\overline{\mathbf{T}}_f = \mathbf{c}_f : \langle\boldsymbol{\epsilon}_f\rangle. \tag{49}$$

Using the definition (30), the averaged fluid strain tensor is determined by

$$\langle\boldsymbol{\epsilon}_f\rangle = \frac{1}{2}[\nabla\langle\mathbf{u}_f\rangle + (\nabla\langle\mathbf{u}_f\rangle)^T] - \mathbf{E}, \tag{50}$$

where the interfacial strain tensor $\mathbf{E}$ is defined by (44), and where we have used the microscopic boundary condition (16). We thus have

$$\phi\overline{\mathbf{T}}_f = \mathbf{c}_f : \nabla(\phi\overline{\mathbf{u}}_f) - \mathbf{c}_f : \mathbf{E}. \tag{51}$$

4.3 Momentum equations

Averaging the solid conservation of momentum equation (2) and neglecting non-linear terms yields

$$(1-\phi)\rho_s\partial_t\overline{\mathbf{v}}_s = \nabla\cdot[(1-\phi)\overline{\mathbf{T}}_s] + \mathbf{d}, \tag{52}$$

where we have defined the 'drag'

$$\mathbf{d} = \frac{1}{V}\int_\Sigma W\hat{\mathbf{n}}'\cdot\mathbf{T}_s'\,\mathrm{d}^2\mathbf{x}'. \tag{53}$$

We will seek to find an explicit macroscopic expression for this drag force.

Similarly, averaging the fluid conservation of momentum equation (9) yields

$$\phi\rho_f\partial_t\overline{\mathbf{v}}_f = \nabla\cdot(\phi\overline{\mathbf{T}}_f) - \mathbf{d}, \tag{54}$$

where, invoking the microscopic continuity of traction (15), the drag term $\mathbf{d}$ is defined by (53).

It is interesting to note that most derivations of the macroscopic equations of motion for porous media agree up to this point. The challenge now lies in finding macroscopic expressions for the interfacial strain tensor $\mathbf{E}$ and the drag force $\mathbf{d}$.

5 DRAG FORCE

The drag force defined in (53) needs to be expressed in terms of macroscopic quantities. In the following two subsections we will examine simple cases in order to assess the form of this drag force. We will come back to its full expression in subsequent sections.

5.1 Static problem

For the equilibrium configuration, that is, when $\mathbf{u}_s = \mathbf{0}$ and $\mathbf{u}_f = \mathbf{0}$, we have microscopic equilibrium in the solid

$$\nabla\cdot\mathbf{T}_s^0 + \rho_s\mathbf{g} = \mathbf{0}, \tag{55}$$

where $\mathbf{g}$ denotes the gravitational acceleration. In the fluid we have

$$-\nabla p_f^0 + \rho_f\mathbf{g} = \mathbf{0}, \tag{56}$$

where $\mathbf{T}_f^0 = -p_f^0\mathbf{I}$. Averaging (55) based upon (29) and (56) based upon (30) we find

$$\langle\nabla\cdot\mathbf{T}_s^0\rangle + \langle\rho_s\mathbf{g}\rangle = \nabla\cdot[(1-\phi)\overline{\mathbf{T}}_s^0] + \mathbf{d}^0 + (1-\phi)\rho_s\mathbf{g} = \mathbf{0}, \tag{57}$$

$$-\langle\nabla p_f^0\rangle + \langle\rho_f\mathbf{g}\rangle = -\nabla(\phi\overline{p}_f^0) - \mathbf{d}^0 + \phi\rho_f\mathbf{g} = \mathbf{0}, \tag{58}$$

where we have used the microscopic boundary condition (15) to define the 'static drag force', that is, the force exerted by the pore fluid on the solid matrix,

$$\mathbf{d}^0 = \frac{1}{V}\int_\Sigma W\hat{\mathbf{n}}'\cdot\mathbf{T}_s^{0\prime}\,\mathrm{d}^2\mathbf{x}' = -\frac{1}{V}\int_\Sigma W\hat{\mathbf{n}}' p_f^{0\prime}\,\mathrm{d}^2\mathbf{x}'. \tag{59}$$

Upon adding (57) and (58) we find that

$$\boldsymbol{\nabla}\cdot\overline{\mathbf{T}}^0 + \overline{\rho}\mathbf{g} = \mathbf{0}, \tag{60}$$

where we have introduced the 'average static stress'

$$\overline{\mathbf{T}}^0 = (1-\phi)\overline{\mathbf{T}}_s^0 - \phi\overline{p}_f^0\mathbf{I}, \tag{61}$$

and the average density

$$\overline{\rho} = (1-\phi)\rho_s + \phi\rho_f. \tag{62}$$

Since the fluid density ρ_f and gravity $\mathbf{g}$ vary only on the macroscopic scale, we deduce from (56) that the hydrostatic fluid pressure p_f^0 also varies only on the macroscopic scale as well, that is, $p_f^0 = \overline{p}_f^0$. Consequently we may write

$$\mathbf{d}^0 = -\frac{1}{V}\int_\Sigma W\hat{\mathbf{n}}' p_f^{0\prime}\,\mathrm{d}^2\mathbf{x}' = -\overline{p}_f^0\frac{1}{V}\int_\Sigma W\hat{\mathbf{n}}'\,\mathrm{d}^2\mathbf{x}' = -\overline{p}_f^0\boldsymbol{\nabla}\phi, \tag{63}$$

where we have used (36). The hydrostatic pore fluid thus exerts a force $-\overline{p}_f^0\boldsymbol{\nabla}\phi$ in the direction of decreasing porosity. Note that when the pore space is empty, that is, consists of vacuum, or when the porosity is constant, this force vanishes.

5.2 Darcy flow

According to Darcy's law, the rate of fluid flow in a rigid porous material is governed by (e.g. Bear 1972; Dahlen 1990)

$$\phi\eta_f\mathbf{k}^{-1}\cdot\overline{\mathbf{v}}_f = -\boldsymbol{\nabla}\overline{p}_f^{\mathrm{Darcy}} + \rho_f\mathbf{g}, \tag{64}$$

where $\overline{p}_f^{\mathrm{Darcy}}$ denotes the macroscopic fluid pressure, $\mathbf{k}$ the permeability tensor and η_f the viscosity.

Under quasistatic conditions, when inertial forces may be ignored, the microscopic equilibrium condition for the fluid is

$$-\boldsymbol{\nabla}p_f^{\mathrm{Darcy}} + \rho_f\mathbf{g} = \mathbf{0}, \tag{65}$$

where p_f^{Darcy} denotes the microscopic fluid pressure. The corresponding macroscopic condition obtained by averaging (65) is

$$-\boldsymbol{\nabla}(\phi\overline{p}_f^{\mathrm{Darcy}}) - \mathbf{d}^{\mathrm{Darcy}} + \phi\rho_f\mathbf{g} = \mathbf{0}, \tag{66}$$

where we have defined the quasi-static drag force

$$\mathbf{d}^{\mathrm{Darcy}} = \frac{1}{V}\int_\Sigma W\hat{\mathbf{n}}'\cdot\mathbf{T}_f{}'\,\mathrm{d}^2\mathbf{x}'. \tag{67}$$

Upon using Darcy's law (64) in (66), we find an explicit expression for the drag force:

$$\mathbf{d}^{\mathrm{Darcy}} = -\overline{p}_f^{\mathrm{Darcy}}\boldsymbol{\nabla}\phi + \phi^2\eta_f\mathbf{k}^{-1}\cdot\overline{\mathbf{v}}_f. \tag{68}$$

Note that in the absence of flow the Darcy drag (68) reduces to the hydrostatic drag (63).

6 INTERFACIAL STRAIN

In this section, we will express the interfacial strain $\mathbf{E}$ defined by (44) in terms of macroscopic quantities.

6.1 Variational principle

Based upon our experiences with the hydrostatic drag force (63) and the drag force for Darcy flow (68), we anticipate a contribution to the drag force $\mathbf{d}$ defined by (53) of the form $\overline{\mathbf{T}}_f\cdot\boldsymbol{\nabla}\phi$. Thus, the solid macroscopic momentum equation (52) contains the right-hand side terms

$$\boldsymbol{\nabla}\cdot[(1-\phi)\overline{\mathbf{T}}_s] + \overline{\mathbf{T}}_f\cdot\boldsymbol{\nabla}\phi, \tag{69}$$

and the macroscopic fluid momentum equation (54) contains the right-hand side terms

$$\boldsymbol{\nabla}\cdot(\phi\overline{\mathbf{T}}_f) - \overline{\mathbf{T}}_f\cdot\boldsymbol{\nabla}\phi. \tag{70}$$

Note again that when there are no gradients in porosity or when the pore space is empty the drag force $\overline{\mathbf{T}}_f\cdot\boldsymbol{\nabla}\phi$ vanishes. Based upon these considerations, we seek to find a functional $F = F(\overline{\mathbf{u}}_s, \overline{\mathbf{u}}_f, \boldsymbol{\nabla}\overline{\mathbf{u}}_s, \boldsymbol{\nabla}\overline{\mathbf{u}}_f)$ with the following attributes:

$$\frac{\partial F}{\partial\boldsymbol{\nabla}\overline{\mathbf{u}}_s} = (1-\phi)\overline{\mathbf{T}}_s, \tag{71}$$

$$\frac{\partial F}{\partial \nabla \overline{\mathbf{u}}_f} = \phi \overline{\mathbf{T}}_f, \tag{72}$$

$$\frac{\partial F}{\partial \overline{\mathbf{u}}_s} = -\frac{\partial F}{\partial \overline{\mathbf{u}}_f} = -\overline{\mathbf{T}}_f \cdot \nabla \phi, \tag{73}$$

subject to the Maxwell relations

$$\frac{\partial^2 F}{\partial \nabla \overline{\mathbf{u}}_f \partial \nabla \overline{\mathbf{u}}_s} = \frac{\partial^2 F}{\partial \nabla \overline{\mathbf{u}}_s \partial \nabla \overline{\mathbf{u}}_f}, \tag{74}$$

$$\frac{\partial^2 F}{\partial \overline{\mathbf{u}}_f \partial \overline{\mathbf{u}}_s} = \frac{\partial^2 F}{\partial \overline{\mathbf{u}}_s \partial \overline{\mathbf{u}}_f}, \tag{75}$$

$$\frac{\partial^2 F}{\partial \nabla \overline{\mathbf{u}}_f \partial \overline{\mathbf{u}}_s} = \frac{\partial^2 F}{\partial \overline{\mathbf{u}}_s \partial \nabla \overline{\mathbf{u}}_f}, \tag{76}$$

$$\frac{\partial^2 F}{\partial \overline{\mathbf{u}}_f \partial \nabla \overline{\mathbf{u}}_s} = \frac{\partial^2 F}{\partial \nabla \overline{\mathbf{u}}_s \partial \overline{\mathbf{u}}_f}, \tag{77}$$

such that

$$\nabla \cdot \left(\frac{\partial F}{\partial \nabla \overline{\mathbf{u}}_s} \right) - \frac{\partial F}{\partial \overline{\mathbf{u}}_s} = \nabla \cdot [(1-\phi)\overline{\mathbf{T}}_s] + \overline{\mathbf{T}}_f \cdot \nabla \phi = (1-\phi)\nabla \cdot \overline{\mathbf{T}}_s + (\overline{\mathbf{T}}_f - \overline{\mathbf{T}}_s) \cdot \nabla \phi, \tag{78}$$

$$\nabla \cdot \left(\frac{\partial F}{\partial \nabla \overline{\mathbf{u}}_f} \right) - \frac{\partial F}{\partial \overline{\mathbf{u}}_f} = \nabla \cdot (\phi \overline{\mathbf{T}}_f) - \overline{\mathbf{T}}_f \cdot \nabla \phi = \phi \nabla \cdot \overline{\mathbf{T}}_f. \tag{79}$$

The existence and form of this functional may also be established by invoking the principle of virtual work, as we show in Appendix A. By assuming a quadratic form for the functional F involving all possible tensor products between $\overline{\mathbf{u}}_s$, $\overline{\mathbf{u}}_f$, $\nabla \overline{\mathbf{u}}_s$, and $\nabla \overline{\mathbf{u}}_f$, and enforcing the constraints (71)–(77), it may be shown that this leads to the following expression for the interfacial strain (44):

$$\mathbf{E} = -\phi \boldsymbol{\alpha} : \nabla \overline{\mathbf{u}}_s + \mathbf{c}_s^{-1} : (\mathbf{c}_s - \mathbf{c}_f : \boldsymbol{\alpha}) : \overline{\mathbf{u}}_s \nabla \phi + \mathbf{c}_s^{-1} : \mathbf{c}_f : \boldsymbol{\alpha} : \nabla (\phi \overline{\mathbf{u}}_f), \tag{80}$$

and the explicit form of the quadratic functional is

$$\begin{aligned} F = {} & \frac{1}{2}(\nabla \overline{\mathbf{u}}_s) : [(1-\phi)\mathbf{c}_s - \phi \mathbf{c}_s : \boldsymbol{\alpha}] : (\nabla \overline{\mathbf{u}}_s) + \frac{1}{2}(\nabla \overline{\mathbf{u}}_f) : [\phi(\mathbf{c}_f - \mathbf{c}_f : \mathbf{c}_s^{-1} : \mathbf{c}_f : \boldsymbol{\alpha})] : (\nabla \overline{\mathbf{u}}_f) \\ & + (\nabla \overline{\mathbf{u}}_s) : (\phi \mathbf{c}_f : \boldsymbol{\alpha}) : (\nabla \overline{\mathbf{u}}_f) \\ & + (\nabla \overline{\mathbf{u}}_s) : (\mathbf{c}_f : \boldsymbol{\alpha}) : (\overline{\mathbf{u}}_f - \overline{\mathbf{u}}_s) \nabla \phi + (\nabla \overline{\mathbf{u}}_f) : (\mathbf{c}_f - \mathbf{c}_f : \mathbf{c}_s^{-1} : \mathbf{c}_f : \boldsymbol{\alpha}) : (\overline{\mathbf{u}}_f - \overline{\mathbf{u}}_s) \nabla \phi \\ & + \frac{1}{2}\phi^{-1} (\nabla \phi)(\overline{\mathbf{u}}_f - \overline{\mathbf{u}}_s) : (\mathbf{c}_f - \mathbf{c}_f : \mathbf{c}_s^{-1} : \mathbf{c}_f : \boldsymbol{\alpha}) : (\overline{\mathbf{u}}_f - \overline{\mathbf{u}}_s) \nabla \phi. \end{aligned} \tag{81}$$

The dimensionless fourth-order tensor $\boldsymbol{\alpha}$ exhibits the symmetries $\alpha_{ijkl} = \alpha_{jikl} = \alpha_{ijlk} = \alpha_{klij}$, that is, in its most general form there are 21 independent parameters. Note that at this stage this tensor remains to be determined. Expressions of the form $\mathbf{c}_s^{-1} : \mathbf{c}_f$ in (80) and (81) should be interpreted in terms of Voigt's notation with contracted indices. In this notation, the solid or fluid fourth-order elastic tensor is written as C_{IJ}, $I, J = 1, \ldots, 6$, such that an expression of the form $\mathbf{c}_s^{-1} : \mathbf{c}_f$ becomes a regular (6×6) matrix expression in Voigt notation: $\mathbf{C}_s^{-1} \cdot \mathbf{C}_f$. Thus, if $\mathbf{c}$ denotes an elastic tensor, $\mathbf{c}^{-1}$ denotes the corresponding compliance tensor.

The macroscopic stresses $\overline{\mathbf{T}}_s$ and $\overline{\mathbf{T}}_f$ are now completely defined in terms of macroscopic quantities by

$$\frac{\partial F}{\partial \nabla \overline{\mathbf{u}}_s} = (1-\phi)\overline{\mathbf{T}}_s = [(1-\phi)\mathbf{c}_s - \phi \mathbf{c}_s : \boldsymbol{\alpha}] : \nabla \overline{\mathbf{u}}_s + (\phi \mathbf{c}_f : \boldsymbol{\alpha}) : \nabla \overline{\mathbf{u}}_f + (\mathbf{c}_f : \boldsymbol{\alpha}) : (\overline{\mathbf{u}}_f - \overline{\mathbf{u}}_s) \nabla \phi, \tag{82}$$

$$\frac{\partial F}{\partial \nabla \overline{\mathbf{u}}_f} = \phi \overline{\mathbf{T}}_f = [\phi(\mathbf{c}_f - \mathbf{c}_f : \mathbf{c}_s^{-1} : \mathbf{c}_f : \boldsymbol{\alpha})] : \nabla \overline{\mathbf{u}}_f + (\phi \mathbf{c}_f : \boldsymbol{\alpha}) : \nabla \overline{\mathbf{u}}_s + (\mathbf{c}_f - \mathbf{c}_f : \mathbf{c}_s^{-1} : \mathbf{c}_f : \boldsymbol{\alpha}) : (\overline{\mathbf{u}}_f - \overline{\mathbf{u}}_s) \nabla \phi. \tag{83}$$

In an isotropic material, the tensor $\boldsymbol{\alpha}$ may be written in terms of two scalar parameters α and β as

$$\alpha_{ijkl} = (\alpha - {}^2/_3 \beta)\delta_{ij}\delta_{kl} + \beta(\delta_{ik}\delta_{jl} + \delta_{il}\delta_{jk}). \tag{84}$$

The change in porosity $\Delta\phi$ defined in (45) may then be obtained by taking the trace of (80):

$$\Delta \phi = -\overline{\mathbf{u}}_s \cdot \nabla \phi + \alpha \phi (\kappa_f / \kappa_s)[(\kappa_s / \kappa_f) \nabla \cdot \overline{\mathbf{u}}_s - \nabla \cdot \overline{\mathbf{u}}_f - (\overline{\mathbf{u}}_f - \overline{\mathbf{u}}_s) \cdot \nabla \ln \phi], \tag{85}$$

where the scalar α remains to be determined. Note that (85) equivalently refers to the change in 'fluid content' of the pore space, since we are interested in fully saturated pores. In the case of constant porosity (85) reduces to the well-known result

$$\Delta \phi = \alpha \phi [\nabla \cdot \overline{\mathbf{u}}_s - (\kappa_f / \kappa_s) \nabla \cdot \overline{\mathbf{u}}_f], \tag{86}$$

where one may regard the difference $\nabla \cdot \overline{\mathbf{u}}_s - (\kappa_f / \kappa_s) \nabla \cdot \overline{\mathbf{u}}_f$ as a measure of the 'effective deformation' of the frame (in the sense of Terzaghi).

For the deviatoric part of $\mathbf{E}$, $\boldsymbol{\Gamma}$ defined in (47), let us define the symmetric, traceless strain deviator tensors

$$\overline{\mathbf{d}}_s = \frac{1}{2}[\nabla \overline{\mathbf{u}}_s + (\nabla \overline{\mathbf{u}}_s)^T] - \frac{1}{3}(\nabla \cdot \overline{\mathbf{u}}_s)\mathbf{I}, \tag{87}$$

$$\overline{\mathbf{d}}_f = \frac{1}{2}[\nabla\overline{\mathbf{u}}_f + (\nabla\overline{\mathbf{u}}_f)^T] - \frac{1}{3}(\nabla\cdot\overline{\mathbf{u}}_f)\mathbf{I}, \tag{88}$$

and the symmetric, traceless tensors

$$\overline{\gamma}_s = \frac{1}{2}[(\nabla\phi)\overline{\mathbf{u}}_s + \overline{\mathbf{u}}_s\nabla\phi] - \frac{1}{3}(\overline{\mathbf{u}}_s\cdot\nabla\phi)\mathbf{I}, \tag{89}$$

$$\overline{\gamma}_f = \frac{1}{2}[(\nabla\phi)\overline{\mathbf{u}}_f + \overline{\mathbf{u}}_f\nabla\phi] - \frac{1}{3}(\overline{\mathbf{u}}_f\cdot\nabla\phi)\mathbf{I}. \tag{90}$$

The deviatoric part of (80) may now be expressed as

$$\mathbf{\Gamma} = \overline{\gamma}_s + \beta(\eta_f/\mu_s)\partial_t(\overline{\gamma}_f - \overline{\gamma}_s) - \beta\phi[\overline{\mathbf{d}}_s - (\eta_f/\mu_s)\partial_t\overline{\mathbf{d}}_f], \tag{91}$$

where the scalar β remains to be determined.

6.2 From ($\overline{\mathbf{u}}_s$,$\overline{\mathbf{u}}_f$) to ($\overline{\mathbf{u}}_s$,$\overline{\mathbf{w}}$)

Following Biot, using the definition of the displacement of the fluid relative to the solid weighted by the porosity,

$$\overline{\mathbf{w}} = \phi(\overline{\mathbf{u}}_f - \overline{\mathbf{u}}_s), \tag{92}$$

which may be seen as a volumetric fluid flow per unit surface area, (81) may be rewritten in terms of the variables $\overline{\mathbf{u}}_s$ and $\overline{\mathbf{w}}$ as

$$\begin{aligned} F = {} & \frac{1}{2}(\nabla\overline{\mathbf{u}}_s):[(1-\phi)\mathbf{c}_s - \phi(\mathbf{c}_s - \mathbf{c}_f):\boldsymbol{\alpha} + \phi\mathbf{c}_f:\boldsymbol{\alpha} + \phi(\mathbf{c}_f - \mathbf{c}_f:\mathbf{c}_s^{-1}:\mathbf{c}_f:\boldsymbol{\alpha})]:(\nabla\overline{\mathbf{u}}_s) \\ & + \frac{1}{2}(\nabla\overline{\mathbf{w}}):[\phi^{-1}(\mathbf{c}_f - \mathbf{c}_f:\mathbf{c}_s^{-1}:\mathbf{c}_f:\boldsymbol{\alpha})]:(\nabla\overline{\mathbf{w}}) + (\nabla\overline{\mathbf{u}}_s):(\mathbf{c}_f - \mathbf{c}_f:\mathbf{c}_s^{-1}:\mathbf{c}_f:\boldsymbol{\alpha} + \mathbf{c}_f:\boldsymbol{\alpha}):(\nabla\overline{\mathbf{w}}). \end{aligned} \tag{93}$$

This is a remarkable result, because all the terms in (81) involving gradients in porosity, $\nabla\phi$, are naturally accommodated by gradients involving $\overline{\mathbf{w}}$. The constitutive relationships (82) and (83) become

$$(1-\phi)\overline{\mathbf{T}}_s = [(1-\phi)\mathbf{c}_s - \phi(\mathbf{c}_s - \mathbf{c}_f):\boldsymbol{\alpha}]:\nabla\overline{\mathbf{u}}_s + (\mathbf{c}_f:\boldsymbol{\alpha}):\nabla\overline{\mathbf{w}}, \tag{94}$$

$$\phi\overline{\mathbf{T}}_f = (\mathbf{c}_f - \mathbf{c}_f:\mathbf{c}_s^{-1}:\mathbf{c}_f:\boldsymbol{\alpha}):\nabla\overline{\mathbf{w}} + \phi(\mathbf{c}_f - \mathbf{c}_f:\mathbf{c}_s^{-1}:\mathbf{c}_f:\boldsymbol{\alpha} + \mathbf{c}_f:\boldsymbol{\alpha}):\nabla\overline{\mathbf{u}}_s. \tag{95}$$

Again we see that gradients in porosity are naturally absorbed by the definition (92).

Upon defining the average macroscopic stress

$$\overline{\mathbf{T}} = (1-\phi)\overline{\mathbf{T}}_s + \phi\overline{\mathbf{T}}_f, \tag{96}$$

and using the constitutive relationships (94) and (95), we discover that the quadratic functional (93) can also be established by using the principle of virtual work in terms of $\overline{\mathbf{u}}_s$ and $\overline{\mathbf{w}}$:

$$F = \frac{1}{2}(\overline{\mathbf{T}}:\nabla\overline{\mathbf{u}}_s + \overline{\mathbf{T}}_f:\nabla\overline{\mathbf{w}}). \tag{97}$$

We can identify the different elements of (97) as (1) the virtual work done by the average solid displacement $\overline{\mathbf{u}}_s$ against the average stress $\overline{\mathbf{T}}$, and (2) the virtual work done by the porosity-weighted relative displacement $\overline{\mathbf{w}}$ against the average fluid stress $\overline{\mathbf{T}}_f$. Note that (97) may be rewritten in terms of $\overline{\mathbf{u}}_s$ and $\overline{\mathbf{u}}_f$ as

$$F = \frac{1}{2}\left[(1-\phi)\overline{\mathbf{T}}_s:\nabla\overline{\mathbf{u}}_s + \phi\overline{\mathbf{T}}_f:\nabla\overline{\mathbf{u}}_f + \overline{\mathbf{T}}_f:\nabla\phi(\overline{\mathbf{u}}_f - \overline{\mathbf{u}}_s)\right], \tag{98}$$

where the different terms may be interpreted as (1) the averaged virtual work related to the solid phase, (2) the averaged virtual work related to the fluid phase and (3) the virtual work done by the relative displacement of the fluid and solid against the drag force $\overline{\mathbf{T}}_f\cdot\nabla\phi$. In Appendix A, we provide an alternative derivation of the macroscopic expression for the interfacial strain based upon the principle of virtual work. In effect, the quadratic forms (93), (97) and (98) are different representations of the 'potential energy density' associated with poroelastic wave propagation.

7 'DRAINED' PARAMETERS

In this section, we are going to identify the remaining unknown fourth-order tensor $\boldsymbol{\alpha}$ introduced in (81), or, in the isotropic case (84), the scalars α and β. This will uniquely specify the macroscopic constitutive relationships (94) and (95) in terms of macroscopic material parameters. Our strategy will be to refer to a Gedanken experiment in order to identify $\boldsymbol{\alpha}$, and thus to obtain expressions for $\Delta\phi$ and $\mathbf{\Gamma}$ and thereby fully constrain $\overline{\mathbf{T}}$ and $\overline{\mathbf{T}}_f$. This approach is similar to that of Pride *et al.* (1992) and Carcione (2007), but contrary to these authors, who used the well-known 'jacketed' and 'unjacketed' experiments, we rely on the definition of the effective stress (Terzaghi 1923, 1943).

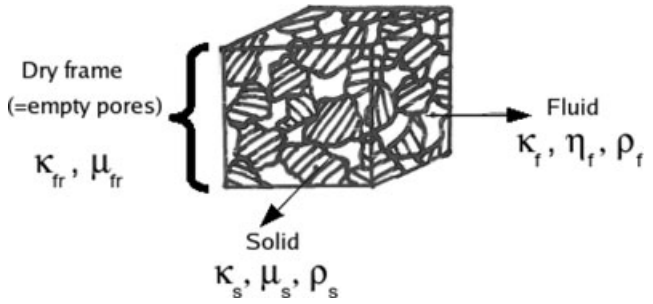

Figure 2. Three types of bulk moduli define the incompressible behaviour of a porous medium: the frame modulus, $\kappa_{\rm fr}$, the solid modulus, κ_s, and the fluid modulus, κ_f. Similarly, two types of shear moduli need to be considered: the shear modulus of the frame, $\mu_{\rm fr}$, and the shear modulus of the solid, μ_s. These five moduli combined with the solid density ρ_s, the fluid density ρ_f, the fluid viscosity η_f, and the permeability k define the nine microscopic parameters that describe a viscous, isotropic, porous medium.

7.1 Gedanken experiment

Let us imagine a dry porous medium, that is, the pore space is empty. We aim to describe the deformation of the skeleton part of such a medium, that is, the frame (Fig. 2). The elastic frame is characterized by a fourth-order tensor $\mathbf{c}_{\rm fr}$, or, in the isotropic case, by a bulk modulus $\kappa_{\rm fr}$ and a shear modulus $\mu_{\rm fr}$.

The constitutive equation we are looking for links the effective stress, $\overline{\mathbf{T}}_{\rm eff}$, perceived by the frame, and its effective deformation:

$$\overline{\mathbf{T}}_{\rm eff} = \mathbf{c}_{\rm fr} : \overline{\epsilon}_{\rm eff}. \tag{99}$$

By defining these effective fields, we isolate the behaviour of the frame by suppressing the effects of the pore fluid on the stress and on the deformation of the frame. This approach is thus equivalent to looking at the system in the absence of pore fluid.

The effective stress is defined as the difference between the total stress, $\overline{\mathbf{T}}$, and the part of the stress exerted by the fluid, $\overline{\mathbf{T}}_f$, (Terzaghi 1923, 1943):

$$\overline{\mathbf{T}}_{\rm eff} = \overline{\mathbf{T}} - \overline{\mathbf{T}}_f. \tag{100}$$

Upon using the definition (96) of $\overline{\mathbf{T}}$, (100) may also be expressed as

$$\overline{\mathbf{T}}_{\rm eff} = (1-\phi)(\overline{\mathbf{T}}_s - \overline{\mathbf{T}}_f). \tag{101}$$

We define the effective deformation of the frame as the total deformation of the solid skeleton minus the deformation of the solid phase due to the stress exerted by the fluid:

$$\overline{\epsilon}_{\rm eff} = \frac{1}{2}\left[\nabla \overline{\mathbf{u}}_s + (\nabla \overline{\mathbf{u}}_s)^T\right] - \mathbf{c}_s^{-1} : \overline{\mathbf{T}}_f. \tag{102}$$

We thus can rewrite the constitutive equation for the frame, (99), in the form

$$(1-\phi)(\overline{\mathbf{T}}_s - \overline{\mathbf{T}}_f) = \mathbf{c}_{\rm fr} : (\nabla \overline{\mathbf{u}}_s - \mathbf{c}_s^{-1} : \overline{\mathbf{T}}_f). \tag{103}$$

The trace of (103) is equivalent to the form given by Pride *et al.* (1992), when the authors look for a closure relationship to constrain the isotropic part of $\mathbf{E}$, that is, the change in porosity $\Delta\phi$. In our approach, the isotropic and the deviatoric parts of $\mathbf{E}$ are both determined at the same time.

Upon using (48) and (51), (103) may be expressed as

$$\mathbf{c}_s : \nabla[(1-\phi)\overline{\mathbf{u}}_s] + \mathbf{c}_s : \mathbf{E} - \phi^{-1}(1-\phi)\left[\mathbf{c}_f : \nabla(\phi \overline{\mathbf{u}}_f) - \mathbf{c}_f : \mathbf{E}\right] = \mathbf{c}_{\rm fr} : \left\{\nabla \overline{\mathbf{u}}_s - \phi^{-1}\mathbf{c}_s^{-1} : [\mathbf{c}_f : \nabla(\phi \overline{\mathbf{u}}_f) - \mathbf{c}_f : \mathbf{E}]\right\}. \tag{104}$$

This yields the following expression for $\mathbf{E}$:

$$\mathbf{E} = \left[\phi \mathbf{c}_s + (1-\phi)\mathbf{c}_f - \mathbf{c}_{\rm fr} : \mathbf{c}_s^{-1} : \mathbf{c}_f\right]^{-1} : \left[\phi[\mathbf{c}_{\rm fr} - (1-\phi)\mathbf{c}_s] : \nabla \overline{\mathbf{u}}_s + \phi \mathbf{c}_s : \overline{\mathbf{u}}_s \nabla\phi + \left[(1-\phi)\mathbf{c}_f - \mathbf{c}_{\rm fr} : \mathbf{c}_s^{-1} : \mathbf{c}_f\right] : \nabla(\phi \overline{\mathbf{u}}_f)\right]. \tag{105}$$

Upon comparing (80) and (105), we deduce that

$$\boldsymbol{\alpha} = [\phi \mathbf{c}_s + (1-\phi)\mathbf{c}_f - \mathbf{c}_{\rm fr} : \mathbf{c}_s^{-1} : \mathbf{c}_f]^{-1} : [(1-\phi)\mathbf{c}_s - \mathbf{c}_{\rm fr}]. \tag{106}$$

Thus, the complete constitutive equations (94) and (95) become

$$\begin{aligned}(1-\phi)\overline{\mathbf{T}}_s = {} & \left\{(1-\phi)\mathbf{c}_s - \phi(\mathbf{c}_s - \mathbf{c}_f) : \left[\phi \mathbf{c}_s + (1-\phi)\mathbf{c}_f - \mathbf{c}_{\rm fr} : \mathbf{c}_s^{-1} : \mathbf{c}_f\right]^{-1} : [(1-\phi)\mathbf{c}_s - \mathbf{c}_{\rm fr}]\right\} : \nabla \overline{\mathbf{u}}_s \\ & + \left\{\mathbf{c}_f : \left[\phi \mathbf{c}_s + (1-\phi)\mathbf{c}_f - \mathbf{c}_{\rm fr} : \mathbf{c}_s^{-1} : \mathbf{c}_f\right]^{-1} : [(1-\phi)\mathbf{c}_s - \mathbf{c}_{\rm fr}]\right\} : \nabla \overline{\mathbf{w}},\end{aligned} \tag{107}$$

and

$$\begin{aligned}\phi\overline{\mathbf{T}}_f = {} & \left\{\mathbf{c}_f - \mathbf{c}_f : \mathbf{c}_s^{-1} : \mathbf{c}_f : [\phi \mathbf{c}_s + (1-\phi)\mathbf{c}_f - \mathbf{c}_{\rm fr} : \mathbf{c}_s^{-1} : \mathbf{c}_f]^{-1} : [(1-\phi)\mathbf{c}_s - \mathbf{c}_{\rm fr}]\right\} : \nabla \overline{\mathbf{w}} \\ & + \phi\left\{\mathbf{c}_f - \mathbf{c}_f : \mathbf{c}_s^{-1} : \mathbf{c}_f : [\phi \mathbf{c}_s + (1-\phi)\mathbf{c}_f - \mathbf{c}_{\rm fr} : \mathbf{c}_s^{-1} : \mathbf{c}_f]^{-1} : [(1-\phi)\mathbf{c}_s - \mathbf{c}_{\rm fr}]\right. \\ & \left. + \mathbf{c}_f : [\phi \mathbf{c}_s + (1-\phi)\mathbf{c}_f - \mathbf{c}_{\rm fr} : \mathbf{c}_s^{-1} : \mathbf{c}_f]^{-1} : [(1-\phi)\mathbf{c}_s - \mathbf{c}_{\rm fr}]\right\} : \nabla \overline{\mathbf{u}}_s.\end{aligned} \tag{108}$$

At this stage, let us consider various limiting cases. First, let us assume that $\mathbf{c}_f \to \mathbf{0}$, then (107) and (108) simplify to

$$(1-\phi)\overline{\mathbf{T}}_s = \mathbf{c}_{\rm fr} : \nabla \overline{\mathbf{u}}_s$$
$$\phi \overline{\mathbf{T}}_f = \mathbf{0}. \tag{109}$$

In the absence of fluid, the porous medium deforms according to the elastic frame tensor $\mathbf{c}_{\rm fr}$, as expected.

Second, suppose that $\mathbf{c}_f \to \mathbf{c}_s$ and $\overline{\mathbf{u}}_s = \overline{\mathbf{u}}_f$, then (107) and (108) simplify to

$$(1-\phi)\overline{\mathbf{T}}_s = (1-\phi)\mathbf{c}_s : \nabla \overline{\mathbf{u}}_s, \tag{110}$$

$$\phi \overline{\mathbf{T}}_f = \phi \mathbf{c}_s : \nabla \overline{\mathbf{u}}_s, \tag{111}$$

which yields

$$\overline{\mathbf{T}} = (1-\phi)\overline{\mathbf{T}}_s + \phi \overline{\mathbf{T}}_f = \mathbf{c}_s : \nabla \overline{\mathbf{u}}_s. \tag{112}$$

(112) shows that the total deformation of the porous medium (solid skeleton and pore fluid) is solely governed by the solid elastic tensor $\mathbf{c}_s$.

Third, let us consider the limiting case where $\phi \to 0$, then the total stress $\overline{\mathbf{T}}$ simplifies to

$$\overline{\mathbf{T}} = \overline{\mathbf{T}}_s = \mathbf{c}_s : \nabla \overline{\mathbf{u}}_s, \tag{113}$$

showing that the medium deforms according to the solid elastic tensor $\mathbf{c}_s$, and the total stress is the solid stress, as expected.

Finally, suppose that $\phi \to 1$, then the total stress $\overline{\mathbf{T}}$ becomes

$$\overline{\mathbf{T}} = \overline{\mathbf{T}}_f = \mathbf{c}_f : \nabla \overline{\mathbf{u}}_f. \tag{114}$$

The medium now deforms according to the fluid tensor $\mathbf{c}_f$, and the total stress is simply the fluid stress, as expected.

7.2 Isotropic media

In isotropic media, the tensor $\boldsymbol{\alpha}$ is defined in terms of the two scalar fields α and β by (84). The scalar α is obtained by taking the trace of (106):

$$\alpha = \frac{(1-\phi)\kappa_s - \kappa_{\rm fr}}{\phi\kappa_s + (1-\phi)\kappa_f - \kappa_{\rm fr}\kappa_f/\kappa_s}, \tag{115}$$

and the deviatoric part of (106) gives the scalar β:

$$\beta = \frac{(1-\phi)\mu_s - \mu_{\rm fr}}{\phi\mu_s + (1-\phi)\eta_f\partial_t - (\mu_{\rm fr}/\mu_s)\eta_f\partial_t}. \tag{116}$$

Note that, strictly speaking, the quantity β, like $\mathbf{c}_f$, is an operator, because it contains partial derivatives with respect to time. The application of this operator is in practice most easily accomplished in the frequency domain. We will continue to use the notation (116) with this understanding.

We can now express the change in porosity, $\Delta\phi$ defined by (85), as

$$\Delta\phi = -\overline{\mathbf{u}}_s \cdot \nabla\phi + \phi \left[\frac{(1-\phi)\kappa_f - \kappa_f\kappa_{\rm fr}/\kappa_s}{\phi\kappa_s + (1-\phi)\kappa_f - \kappa_{\rm fr}\kappa_f/\kappa_s} \right] [(\kappa_s/\kappa_f)\nabla\cdot\overline{\mathbf{u}}_s - \nabla\cdot\overline{\mathbf{u}}_f - (\overline{\mathbf{u}}_f - \overline{\mathbf{u}}_s)\cdot\nabla\ln\phi], \tag{117}$$

and the deviatoric interfacial strain $\boldsymbol{\Gamma}$ (91) is given by

$$\begin{aligned}\boldsymbol{\Gamma} = \overline{\gamma}_s &+ \left[\frac{(1-\phi)\eta_f\partial_t - \mu_{\rm fr}\eta_f/\mu_s\partial_t}{\phi\mu_s + (1-\phi)\eta_f\partial_t - (\mu_{\rm fr}/\mu_s)\eta_f\partial_t} \right] (\overline{\gamma}_f - \overline{\gamma}_s) \\ &- \left[\frac{\phi(1-\phi)\mu_s - \phi\mu_{\rm fr}}{\phi\mu_s + (1-\phi)\eta_f\partial_t - (\mu_{\rm fr}/\mu_s)\eta_f\partial_t} \right] [\overline{\mathbf{d}}_s - (\eta_f/\mu_s)\partial_t\overline{\mathbf{d}}_f].\end{aligned} \tag{118}$$

We can further simplify (118) when the pore fluid does not bear any shear stress, that is, $\eta_f\partial_t = 0$, or when $\eta_f \ll \mu_s$:

$$\boldsymbol{\Gamma} = \overline{\gamma}_s - [(1-\phi) - \mu_{\rm fr}/\mu_s]\overline{\mathbf{d}}_s. \tag{119}$$

In the case of constant porosity ($\nabla\phi = \mathbf{0}$), (117) and (119) are in agreement with Pride *et al.* (1992).

For an isotropic medium, the constitutive eqs (107) and (108) become

$$\begin{aligned}(1-\phi)\overline{\mathbf{T}}_s = &\left\{ \frac{\kappa_s[(1-\phi)\kappa_f + \phi\kappa_{\rm fr}] - \kappa_{\rm fr}\kappa_f}{\phi\kappa_s + (1-\phi)\kappa_f - \kappa_{\rm fr}\kappa_f/\kappa_s} \nabla\cdot\overline{\mathbf{u}}_s + \frac{(1-\phi)\kappa_s\kappa_f - \kappa_{\rm fr}\kappa_f}{\phi\kappa_s + (1-\phi)\kappa_f - \kappa_{\rm fr}\kappa_f/\kappa_s} \nabla\cdot\overline{\mathbf{w}} \right\} \mathbf{I} \\ &+ \left\{ \frac{[(1-\phi)\mu_s - \mu_{\rm fr}](1-\phi)\eta_f\partial_t + \phi\mu_s\mu_{\rm fr}}{\phi\mu_s + (1-\phi)\eta_f\partial_t - (\mu_{\rm fr}/\mu_s)\eta_f\partial_t} \right\} 2\overline{\mathbf{d}}_s \\ &+ \left[\frac{(1-\phi)\mu_s\eta_f\partial_t - \mu_{\rm fr}\eta_f\partial_t}{\phi\mu_s + (1-\phi)\eta_f\partial_t - (\mu_{\rm fr}/\mu_s)\eta_f\partial_t} \right] 2\left(\phi\overline{\mathbf{d}}_f + \overline{\gamma}_f - \overline{\gamma}_s\right),\end{aligned} \tag{120}$$

and

$$\phi\overline{\mathbf{T}}_f = \left[\frac{\phi\kappa_s\kappa_f}{\phi\kappa_s+(1-\phi)\kappa_f-\kappa_{\rm fr}\kappa_f/\kappa_s}\,\boldsymbol{\nabla}\cdot\overline{\mathbf{w}}+\frac{\phi\kappa_f(\kappa_s-\kappa_{\rm fr})}{\phi\kappa_s+(1-\phi)\kappa_f-\kappa_{\rm fr}\kappa_f/\kappa_s}\,\boldsymbol{\nabla}\cdot\overline{\mathbf{u}}_s\right]\mathbf{I}$$
$$+\left\{\frac{[(1-\phi)\mu_s-\mu_{\rm fr}]\eta_f\partial_t}{\phi\mu_s+(1-\phi)\eta_f\partial_t-(\mu_{\rm fr}/\mu_s)\eta_f\partial_t}\right\}2\overline{\mathbf{d}}_s$$
$$+\left[\frac{\phi\mu_s\eta_f\partial_t}{\phi\mu_s+(1-\phi)\eta_f\partial_t-(\mu_{\rm fr}/\mu_s)\eta_f\partial_t}\right]2\left(\phi\overline{\mathbf{d}}_f+\overline{\gamma}_f-\overline{\gamma}_s\right). \tag{121}$$

The constitutive equations (120) and (121) may be further simplified when the pore fluid does not bear any shear stress:

$$(1-\phi)\overline{\mathbf{T}}_s=\left\{\frac{\kappa_s[(1-\phi)\kappa_f+\phi\kappa_{\rm fr}]-\kappa_{\rm fr}\kappa_f}{\phi\kappa_s+(1-\phi)\kappa_f-\kappa_{\rm fr}\kappa_f/\kappa_s}\,\boldsymbol{\nabla}\cdot\overline{\mathbf{u}}_s+\frac{(1-\phi)\kappa_s\kappa_f-\kappa_{\rm fr}\kappa_f}{\phi\kappa_s+(1-\phi)\kappa_f-\kappa_{\rm fr}\kappa_f/\kappa_s}\,\boldsymbol{\nabla}\cdot\overline{\mathbf{w}}\right\}\mathbf{I}+2\mu_{\rm fr}\overline{\mathbf{d}}_s, \tag{122}$$

and

$$\phi\overline{\mathbf{T}}_f=\phi\left[\frac{\kappa_s\kappa_f}{\phi\kappa_s+(1-\phi)\kappa_f-\kappa_{\rm fr}\kappa_f/\kappa_s}\,\boldsymbol{\nabla}\cdot\overline{\mathbf{w}}+\frac{\kappa_f(\kappa_s-\kappa_{\rm fr})}{\phi\kappa_s+(1-\phi)\kappa_f-\kappa_{\rm fr}\kappa_f/\kappa_s}\,\boldsymbol{\nabla}\cdot\overline{\mathbf{u}}_s\right]\mathbf{I}. \tag{123}$$

Note that in this approximation the solid phase shear modulus μ_s disappears. Shear stress is thus entirely supported by the frame.

7.3 Comparison with the Biot coefficients

The original Biot constitutive equations (Biot 1956ab, 1962a,b) may be written in the form

$$\overline{\mathbf{T}}=\left[\left(H-\frac{4}{3}\mu_{\rm fr}\right)\boldsymbol{\nabla}\cdot\overline{\mathbf{u}}_s+C\boldsymbol{\nabla}\cdot\overline{\mathbf{w}}\right]\mathbf{I}+2\mu_{\rm fr}\overline{\mathbf{d}}_s, \tag{124}$$

and

$$\overline{\mathbf{T}}_f=-\overline{p}_f\mathbf{I}=(C\boldsymbol{\nabla}\cdot\overline{\mathbf{u}}_s+M\boldsymbol{\nabla}\cdot\overline{\mathbf{w}})\,\mathbf{I}. \tag{125}$$

The moduli H, C and M are defined in terms of material (solid, fluid and frame) properties as follows (Geertsma & Smit 1961; Stoll & Bryan 1970):

$$H=\frac{(\kappa_s-\kappa_{\rm fr})^2}{D-\kappa_{\rm fr}}+\kappa_{\rm fr}+\frac{4}{3}\mu_{\rm fr}, \tag{126}$$

$$C=\frac{\kappa_s(\kappa_s-\kappa_{\rm fr})}{D-\kappa_{\rm fr}}, \tag{127}$$

$$M=\frac{\kappa_s^2}{D-\kappa_{\rm fr}}, \tag{128}$$

where

$$D=\kappa_s[1+\phi(\kappa_s/\kappa_f-1)]. \tag{129}$$

Upon substituting (127), (128) and (129) in (125), we obtain

$$\overline{\mathbf{T}}_f=-\overline{p}_f\mathbf{I}=\left[\frac{\kappa_f(\kappa_s-\kappa_{\rm fr})}{\phi\kappa_s+(1-\phi)\kappa_f-\kappa_{\rm fr}\kappa_f/\kappa_s}\,\boldsymbol{\nabla}\cdot\overline{\mathbf{u}}_s+\frac{\kappa_s\kappa_f}{\phi\kappa_s+(1-\phi)\kappa_f-\kappa_{\rm fr}\kappa_f/\kappa_s}\boldsymbol{\nabla}\cdot\overline{\mathbf{w}}\right]\mathbf{I}. \tag{130}$$

We thus find that (125) is in exact agreement with (123). We can similarly show the equivalence between (124) and the sum of (122) and (123). This establishes the equivalence between our derivation and Biot's results, and confirms again the validity of the Biot equations for media with gradients in porosity.

8 EQUATIONS OF MOTION

In the two sections that follow, the equations of motion are derived both without and with taking into account dissipation processes generated by viscous Poiseuille (laminar) flow. A third section is dedicated to the frequency-dependence of fluid flow, which allows us to derive the equations of motion at high frequencies. We also discuss and introduce a viscoelastic rheology to account for non-Biot attenuation mechanisms related to the anelasticity of the frame (Stoll & Bryan 1970; Stoll 1977).

8.1 No dissipation

Following Biot (1956a), we write the 'kinetic energy density' in the form

$$K=\frac{1}{2}\rho_{11}\partial_t\overline{\mathbf{u}}_s\cdot\partial_t\overline{\mathbf{u}}_s+\rho_{12}\partial_t\overline{\mathbf{u}}_s\cdot\partial_t\overline{\mathbf{u}}_f+\frac{1}{2}\rho_{22}\partial_t\overline{\mathbf{u}}_f\cdot\partial_t\overline{\mathbf{u}}_f, \tag{131}$$

where the coefficients ρ_{11}, ρ_{22} and ρ_{12}, may be interpreted as the total effective mass density of the moving solid, the total effective mass density of the fluid moving within the skeleton and a coupling coefficient, respectively.

In order to derive the equations of motion, we consider the Euler–Lagrange equations associated with the variational principle defined by the Lagrangian density

$$L = K - F, \tag{132}$$

that is

$$\frac{\partial}{\partial t}\frac{\partial L}{\partial \dot{q}} + \boldsymbol{\nabla}\cdot\left(\frac{\partial L}{\partial \boldsymbol{\nabla} q}\right) - \frac{\partial L}{\partial q} = 0. \tag{133}$$

Here q refers to the generalized coordinates $\overline{\mathbf{u}}_s$ and $\overline{\mathbf{u}}_f$. Contributions due to dissipative processes have been neglected and will be considered in the next section. Written out in full, the Euler–Lagrange equations (133) are

$$\rho_{11}\partial_t^2\overline{\mathbf{u}}_s + \rho_{12}\partial_t^2\overline{\mathbf{u}}_f - \boldsymbol{\nabla}\cdot[(1-\phi)\overline{\mathbf{T}}_s] - \overline{\mathbf{T}}_f\cdot\boldsymbol{\nabla}\phi = \mathbf{0}, \tag{134}$$

$$\rho_{12}\partial_t^2\overline{\mathbf{u}}_s + \rho_{22}\partial_t^2\overline{\mathbf{u}}_f - \boldsymbol{\nabla}\cdot(\phi\overline{\mathbf{T}}_f) + \overline{\mathbf{T}}_f\cdot\boldsymbol{\nabla}\phi = \mathbf{0}, \tag{135}$$

for the solid and the fluid, respectively. These equations may be rewritten in the form

$$(1-\phi)\rho_s\partial_t^2\overline{\mathbf{u}}_s = \boldsymbol{\nabla}\cdot[(1-\phi)\overline{\mathbf{T}}_s] + \overline{\mathbf{T}}_f\cdot\boldsymbol{\nabla}\phi - [\rho_{11} - (1-\phi)\rho_s]\partial_t^2\overline{\mathbf{u}}_s - \rho_{12}\partial_t^2\overline{\mathbf{u}}_f, \tag{136}$$

$$\phi\rho_f\partial_t^2\overline{\mathbf{u}}_f = \boldsymbol{\nabla}\cdot(\phi\overline{\mathbf{T}}_f) - \overline{\mathbf{T}}_f\cdot\boldsymbol{\nabla}\phi - \rho_{12}\partial_t^2\overline{\mathbf{u}}_s - (\rho_{22} - \phi\rho_f)\partial_t^2\overline{\mathbf{u}}_f. \tag{137}$$

Upon comparing (136) and (137) with (52) and (54) we can identify the drag terms as

$$\mathbf{d} = \overline{\mathbf{T}}_f\cdot\boldsymbol{\nabla}\phi - [\rho_{11} - (1-\phi)\rho_s]\partial_t^2\overline{\mathbf{u}}_s - \rho_{12}\partial_t^2\overline{\mathbf{u}}_f, \tag{138}$$

$$\mathbf{d} = \overline{\mathbf{T}}_f\cdot\boldsymbol{\nabla}\phi + \rho_{12}\partial_t^2\overline{\mathbf{u}}_s + (\rho_{22} - \phi\rho_f)\partial_t^2\overline{\mathbf{u}}_f. \tag{139}$$

Since (138) and (139) need to be equal, we deduce that

$$\rho_{11} = (1-\phi)\rho_s - \rho_{12}, \qquad \rho_{22} = \phi\rho_f - \rho_{12}, \tag{140}$$

and we can interpret ρ_{11} and ρ_{22} as the 'effective mass densities' of the solid and fluid, respectively.

At this point, let us assume that the fluid is restrained from moving, that is, $\overline{\mathbf{u}}_f = \mathbf{0}$. Then, according to (137), we see that in order to prevent any fluid displacement, we need to apply a force in the opposite direction to the solid acceleration. Thus, we must have $\rho_{12} < 0$. The drag term may be written in terms of ρ_{12} as

$$\mathbf{d} = \overline{\mathbf{T}}_f\cdot\boldsymbol{\nabla}\phi - \rho_{12}\left(\partial_t^2\overline{\mathbf{u}}_f - \partial_t^2\overline{\mathbf{u}}_s\right), \tag{141}$$

where the last term may be interpreted as the inertial drag that the fluid exerts on the solid, when there is a relative acceleration between the two phases. Note that if we rewrite the kinetic energy density in terms of ρ_{12} we find

$$K = \frac{1}{2}(1-\phi)\rho_s\partial_t\overline{\mathbf{u}}_s\cdot\partial_t\overline{\mathbf{u}}_s + \frac{1}{2}\phi\rho_f\partial_t\overline{\mathbf{u}}_f\cdot\partial_t\mathbf{u}_f - \frac{1}{2}\rho_{12}(\partial_t\overline{\mathbf{u}}_f - \partial_t\overline{\mathbf{u}}_s)\cdot(\partial_t\overline{\mathbf{u}}_f - \partial_t\overline{\mathbf{u}}_s). \tag{142}$$

The kinetic energy density is now expressed as the sum of (1) the average of the kinetic energy density of the solid, (2) the average of the kinetic energy density of the fluid and (3) the kinetic energy density due to the relative motion of an additional apparent fluid mass arising from the inertial drag of the fluid.

The coefficient ρ_{22}, the effective density of the fluid, is determined in Biot (1962a) and Leclaire *et al.* (1994) by introducing a linear relationship between the relative macroscopic fluid flow, $\overline{\mathbf{w}}$, and the relative microvelocities within the pores in order to take into account the fact that not all the pore fluid moves in the direction of the macroscopic pore fluid stress gradient because of the geometry of the pore space. A recent paper derives this coefficient based on a more general concept of dispersion of velocities in the fluid (Molotkov 2002). However, in the case of isotropy of the microvelocity field, those different studies propose the same expression:

$$\rho_{22} = m\phi^2, \tag{143}$$

where $m = c\rho_f/\phi$. The parameter c corresponds to the 'tortuosity', which is an experimental quantity often defined as the ratio between the actual flow path and the straight line distance between the ends of the flow path. Using (140) it follows that

$$-\rho_{12} = m\phi^2 - \phi\rho_f = (c-1)\phi\rho_f, \qquad \rho_{11} = (1-\phi)\rho_s + m\phi^2 - \phi\rho_f = (1-\phi)\rho_s + (c-1)\phi\rho_f. \tag{144}$$

8.2 Dissipation

Next, dissipation generated by viscous flow of the fluid phase is taken into account, and it is assumed to depend only on the relative motion between the fluid and the solid. The Euler–Lagrange equations (133) are therefore appended as follows:

$$\frac{\partial}{\partial t}\frac{\partial L}{\partial \dot{q}} + \boldsymbol{\nabla}\cdot\left(\frac{\partial L}{\partial \boldsymbol{\nabla} q}\right) - \frac{\partial L}{\partial q} + \frac{\partial D_p}{\partial \dot{q}} = 0, \tag{145}$$

where D_p is the dissipation potential directly connected to Darcy's law (Biot 1956a, 1962a):

$$D_p = \frac{1}{2}\phi(\partial_t\overline{\mathbf{u}}_f - \partial_t\overline{\mathbf{u}}_s)\cdot\mathbf{b}\cdot\phi(\partial_t\overline{\mathbf{u}}_f - \partial_t\overline{\mathbf{u}}_s). \tag{146}$$

The second-order, symmetric tensor **b** is a function of the fluid properties:

$$\mathbf{b} = \eta_f \mathbf{k}^{-1}, \tag{147}$$

and is valid for Poiseuille (laminar) pore fluid flow (see Section 8.3 for a discussion), where η_f is the fluid viscosity and **k** the porous medium permeability tensor. Written out in full the Euler–Lagrange equations (145) are

$$(1-\phi)\rho_s \partial_t^2 \overline{\mathbf{u}}_s = \nabla \cdot [(1-\phi)\overline{\mathbf{T}}_s] + \overline{\mathbf{T}}_f \cdot \nabla\phi + (c-1)\phi\rho_f \left(\partial_t^2 \overline{\mathbf{u}}_f - \partial_t^2 \overline{\mathbf{u}}_s\right) + \phi^2 \eta_f \mathbf{k}^{-1} \cdot (\partial_t \overline{\mathbf{u}}_f - \partial_t \overline{\mathbf{u}}_s), \tag{148}$$

$$\phi\rho_f \partial_t^2 \overline{\mathbf{u}}_f = \nabla \cdot (\phi \overline{\mathbf{T}}_f) - \overline{\mathbf{T}}_f \cdot \nabla\phi - (c-1)\phi\rho_f (\partial_t^2 \overline{\mathbf{u}}_f - \partial_t^2 \overline{\mathbf{u}}_s) - \phi^2 \eta_f \mathbf{k}^{-1} \cdot (\partial_t \overline{\mathbf{u}}_f - \partial_t \overline{\mathbf{u}}_s). \tag{149}$$

The drag term is thus

$$\mathbf{d} = \overline{\mathbf{T}}_f \cdot \nabla\phi + \phi^2 \eta_f \mathbf{k}^{-1} \cdot (\partial_t \overline{\mathbf{u}}_f - \partial_t \overline{\mathbf{u}}_s) + (c-1)\phi\rho_f (\partial_t^2 \overline{\mathbf{u}}_f - \partial_t^2 \overline{\mathbf{u}}_s), \tag{150}$$

where the first term on the right-hand side represents the force due to gradients in porosity (which we also encountered for media in hydrostatic equilibrium and for Darcy flow), the second term is a viscous term that captures drag on the pore walls associated with relative motion between the fluid and the solid (which we also encountered in Darcy flow), and the final term represents a dissipative force associated with inertial drag due to the relative acceleration between the fluid and the solid.

8.3 Frequency dependence

For oscillatory motion, the tensor **b** defined in (147), expressing the viscous resistance to fluid flow, becomes frequency dependent (Biot 1956a). At low frequencies, the fluid flow is laminar (Poiseuille flow), meaning that inertial forces are negligible compared to viscous forces, which control the flow regime. In this case, the flow regime may be expressed in terms of a classical diffusion equation, and **b** is given by (147). At high frequencies, when the fluid flow is no longer laminar, the fluid velocity distribution within the pores is more complex, and the effects of viscosity are felt only in a thin boundary layer. In this case, inertial forces dominate the flow regime. Biot's characteristic frequency defining the limit between the two flow regimes is given by (Biot 1956b; Auriault *et al.* 1985; Carcione 2007)

$$f_c = \min\left(\frac{\eta_f \phi}{2\pi c \rho_f k_{ij}}\right), \tag{151}$$

where k_{ij} denotes the components of the permeability tensor.

In order to accommodate the change in flow regime at high frequencies, Biot (1956b) uses a frequency-dependent correction factor in the term involving **b**. In later work, Biot (1962b) introduces the notion of a viscodynamic operator to account for viscous flow over the full frequency range. Comparisons of the predicted attenuation to experimental measurements at low frequencies (Mochizuki 1982) and high frequencies (Arntsen & Carcione 2001) show that the dissipation predicted by a theory involving only viscous resistance is smaller than observed in laboratory experiments. Thus, viscous resistance to fluid flow accounts only for a part of the attenuation and dissipation processes in a porous medium over the full frequency range (Stoll & Bryan 1970; Stoll 1977). Other dissipation phenomena of a mechanical, chemical or thermoelastic nature may also play a role, and these are often referred to as 'non-Biot' attenuation mechanisms. They are associated with the anelasticity of the frame, and are usually taken into account by introducing a viscoelastic rheology (Biot 1962a,b; Carcione 1993).

In the following, we present the implementation of both corrections in the time domain. This will allow us to numerically address attenuation and viscous damping over the full frequency range, and thus to accurately model such processes.

8.3.1 Anelastic response of the frame

In previous studies, anelasticity of the frame has been accommodated by regarding the coefficients H, M, C and $\mu_{\rm fr}$ as complex, frequency-dependent moduli (Stoll & Bryan 1970; Stoll 1977). Typically, the moduli are separated in terms of real solid and fluid properties and complex frame properties.

Following Carcione (1993, 2007), we describe attenuation controlled by the anelasticity of the frame by introducing a viscoelastic rheology. The basic hypothesis is that the current stress depends upon the strain history, such that (124) and (125) may be rewritten as

$$\overline{\mathbf{T}}(t) = \int_{-\infty}^{t} \left[\partial_t B(t-t')\nabla \cdot \overline{\mathbf{u}}_s(t')\,\mathbf{I} + \partial_t C(t-t')\nabla \cdot \overline{\mathbf{w}}(t')\,\mathbf{I} + 2\partial_t \mu_{\rm fr}(t-t')\overline{\mathbf{d}}_s(t')\right] \mathrm{d}t', \tag{152}$$

and

$$\overline{\mathbf{T}}_f(t) = \int_{-\infty}^{t} \left[\partial_t C(t-t')\nabla \cdot \overline{\mathbf{u}}_s(t')\,\mathbf{I} + \partial_t M(t-t')\nabla \cdot \overline{\mathbf{w}}(t')\,\mathbf{I}\right] \mathrm{d}t', \tag{153}$$

where we have introduced the compressional modulus

$$B = H - \frac{4}{3}\mu_{\rm fr} = \frac{(\kappa_s - \kappa_{\rm fr})^2}{D - \kappa_{\rm fr}} + \kappa_{\rm fr}. \tag{154}$$

Similar to viscoelastic single-phase media, a series of L standard linear solids may be introduced to capture dissipation in poroelastic media (Liu *et al.* 1976; Carcione *et al.* 1988b; Robertsson *et al.* 1994). Such an approach results in an almost constant quality factor Q over a selected frequency range, thus modelling an absorption-band poroelastic medium (Carcione 1993).

At this point we make the same assumption as Stoll & Bryan (1970), Stoll (1977), which is that only the time-dependence of the bulk and shear moduli of the frame, $\kappa_{\rm fr}$ and $\mu_{\rm fr}$, that is, the assemblage of particles, needs to be considered, accommodating the fact that various forms of energy dissipation may occur at grain contacts. Moreover, considering the fact that the bulk quality factor is generally observed to be several orders of magnitude larger than the shear quality factor, dissipation is mainly controlled by shear attenuation, and thus only the time dependence of the isotropic frame shear modulus $\mu_{\rm fr}$ needs to be accommodated (Komatitsch & Tromp 1999). Modelling an absorption-band poroelastic medium by a series of L standard-linear solids, we express the frame shear modulus as

$$\mu_{\rm fr}(t) = \mu_{\rm fr}^R \left[1 - \sum_{\ell=1}^{L} (1 - \tau^{\epsilon\ell}/\tau^{\sigma\ell}) \exp(-t/\tau^{\sigma\ell}) \right] H(t), \tag{155}$$

where $\mu_{\rm fr}^R$ denotes the relaxed frame shear modulus, $H(t)$ is the Heaviside function and $\tau^{\epsilon\ell}$ and $\tau^{\sigma\ell}$ are strain and stress relaxation times, respectively. Using the anelastic frame shear modulus (155), the constitutive relationships (152) and (153) may be rewritten as

$$\overline{\mathbf{T}} = (B\boldsymbol{\nabla}\cdot\overline{\mathbf{u}}_s + C\boldsymbol{\nabla}\cdot\overline{\mathbf{w}})\,\mathbf{I} + 2\mu_{\rm fr}^U \overline{\mathbf{d}}_s - \sum_{\ell=1}^{L} \mathbf{R}^\ell, \tag{156}$$

and

$$\overline{\mathbf{T}}_f = -\overline{p}_f \mathbf{I} = (C\boldsymbol{\nabla}\cdot\overline{\mathbf{u}}_s + M\boldsymbol{\nabla}\cdot\overline{\mathbf{w}})\,\mathbf{I}. \tag{157}$$

Note that in this approximation only the total stress $\overline{\mathbf{T}}$ is affected. The unrelaxed frame shear modulus, $\mu_{\rm fr}^U$, is defined by

$$\mu_{\rm fr}^U = \mu_{\rm fr}^R \left[1 - \sum_{\ell=1}^{L} (1 - \tau^{\epsilon\ell}/\tau^{\sigma\ell}) \right], \tag{158}$$

and the symmetric, traceless tensors $\mathbf{R}^\ell$, $\ell = 1, \ldots, L$, represent a series of (tensor) memory variables which are governed by

$$\partial_t \mathbf{R}^\ell = -\mathbf{R}^\ell/\tau^{\sigma\ell} + \delta\mu_{\rm fr}^\ell \overline{\mathbf{d}}_s/\tau^{\sigma\ell}, \tag{159}$$

where the modulus defect $\delta\mu_{\rm fr}^\ell$ is given by

$$\delta\mu_{\rm fr}^\ell = -\mu_{\rm fr}^R (1 - \tau^{\epsilon\ell}/\tau^{\sigma\ell}). \tag{160}$$

8.3.2 Viscous resistance

As already mentioned, the notion of a viscodynamic operator was introduced by Biot to cope with the change in fluid flow regime at high frequencies. Unfortunately, this factor is highly sensitive to the pore network structure, meaning that an analysis of the frequency dependence should be performed for each specific material (Biot 1962b). For example, Biot (1962b) derived frequency-domain expressions for cylindrical silt, which have been widely used (e.g. Auriault *et al.* 1985; Carcione & Quiroga-Goode 1996). An alternative strategy would be to regard η_f and $\mathbf{k}$ as empirical parameters, and to assume no particular pore geometry.

In this section we present another alternative, which involves redefining $\mathbf{b}$, given by (147), as a relaxation function, thus treating viscous resistance similar to attenuation processes related to the anelasticity of the frame. Using this approach, the components of the relaxation function $\mathbf{b}(t)$ may be described in terms of L' viscous relaxation mechanisms as (Carcione 2007; de la Puente 2008)

$$b_{ij}(t) = \eta_f k_{ij}^{-1} \left[1 - \sum_{\ell=1}^{L'} \left(1 - \theta_{ij}^{\epsilon\ell}/\theta^{\sigma\ell}\right) \exp(-t/\theta^{\sigma\ell}) \right] H(t), \tag{161}$$

where $\theta_{ij}^{\epsilon\ell}$ and $\theta^{\sigma\ell}$ are strain and stress relaxation times, respectively. Note that at low frequency ($t \to \infty$), we recover (147). Using this expression, the drag term (150) may be rewritten as

$$\mathbf{d} = \overline{\mathbf{T}}_f \cdot \boldsymbol{\nabla}\phi + \phi^2 \mathbf{b}^U \cdot (\partial_t \overline{\mathbf{u}}_f - \partial_t \overline{\mathbf{u}}_s) + (c-1)\phi\rho_f \left(\partial_t^2 \overline{\mathbf{u}}_f - \partial_t^2 \overline{\mathbf{u}}_s\right) - \sum_{\ell=1}^{L'} \mathbf{r}^\ell, \tag{162}$$

where $\mathbf{b}^U$ is the unrelaxed viscous term defined by

$$b_{ij}^U = \eta_f k_{ij}^{-1} \left[1 - \sum_{\ell=1}^{L'} \left(1 - \theta_{ij}^{\epsilon\ell}/\theta^{\sigma\ell}\right) \right], \tag{163}$$

and $\mathbf{r}^\ell$, $\ell = 1, \ldots, L'$, represent series of (vector) memory variables which satisfy

$$\partial_t \mathbf{r}^\ell = -\mathbf{r}^\ell/\theta^{\sigma\ell} + \phi^2 \delta\mathbf{b}^\ell \cdot (\partial_t \overline{\mathbf{u}}_f - \partial_t \overline{\mathbf{u}}_s)/\theta^{\sigma\ell}. \tag{164}$$

The viscous defect $\delta\mathbf{b}^\ell$ is determined by

$$\delta b_{ij}^\ell = -\eta_f k_{ij}^{-1} \left(1 - \theta_{ij}^{\epsilon\ell}/\theta^{\sigma\ell}\right). \tag{165}$$

In practice, it often suffices to use a single mechanism ($L' = 1$).

8.4 Biot's equations of motion

By adding equations (148) and (149) and keeping the second equation (149), we obtain an alternative set of equations, incorporating the frequency-dependent viscosity introduced in the previous section,

$$\overline{\rho}\partial_t^2\overline{\mathbf{u}}_s + \rho_f\partial_t^2\overline{\mathbf{w}} = \boldsymbol{\nabla}\cdot\overline{\mathbf{T}}, \tag{166}$$

$$\rho_f\partial_t^2\overline{\mathbf{w}} + \phi\rho_f\partial_t^2\overline{\mathbf{u}}_s = \boldsymbol{\nabla}\cdot(\phi\overline{\mathbf{T}}_f) - \overline{\mathbf{T}}_f\cdot\boldsymbol{\nabla}\phi - (c-1)\rho_f\partial_t^2\overline{\mathbf{w}} - \phi\mathbf{b}(t)(*\cdot)\partial_t\overline{\mathbf{w}}, \tag{167}$$

where we have used the definitions (92) for $\overline{\mathbf{w}}$, (96) for the average macroscopic stress $\overline{\mathbf{T}}$ and (62) for the average density $\overline{\rho}$. The symbol $(*\cdot)$ denotes time convolution combined with the dot product. (167) may finally be rearranged as

$$m\partial_t^2\overline{\mathbf{w}} + \rho_f\partial_t^2\overline{\mathbf{u}}_s + \mathbf{b}(t)(*\cdot)\partial_t\overline{\mathbf{w}} = \boldsymbol{\nabla}\cdot\overline{\mathbf{T}}_f, \tag{168}$$

where $m = \rho_f c/\phi$. We thus recover the original Biot equations of motion (Biot 1956a, 1962a). Note that we have demonstrated that the Biot equations of motion in terms of $\overline{\mathbf{u}}_s$ and $\overline{\mathbf{w}}$ 'remain valid for media with gradients in porosity'.

9 SUMMARY OF THE MAIN EQUATIONS

In summary, wave propagation in poroelastic media is governed by the macroscopic equations of motion

$$(1-\phi)\rho_s\partial_t^2\overline{\mathbf{u}}_s = \boldsymbol{\nabla}\cdot[(1-\phi)\overline{\mathbf{T}}_s] + \overline{\mathbf{T}}_f\cdot\boldsymbol{\nabla}\phi + (c-1)\phi\rho_f\left(\partial_t^2\overline{\mathbf{u}}_f - \partial_t^2\overline{\mathbf{u}}_s\right) + \phi^2\mathbf{b}(t)(*\cdot)\left(\partial_t\overline{\mathbf{u}}_f - \partial_t\overline{\mathbf{u}}_s\right), \tag{169}$$

$$\phi\rho_f\partial_t^2\overline{\mathbf{u}}_f = \phi\boldsymbol{\nabla}\cdot\overline{\mathbf{T}}_f - (c-1)\phi\rho_f(\partial_t^2\overline{\mathbf{u}}_f - \partial_t^2\overline{\mathbf{u}}_s) - \phi^2\mathbf{b}(t)(*\cdot)(\partial_t\overline{\mathbf{u}}_f - \partial_t\overline{\mathbf{u}}_s). \tag{170}$$

The most general anisotropic constitutive relationships are (107) and (108) in terms of the anisotropic frame, solid and fluid tensors $\mathbf{c}_{\rm fr}$, $\mathbf{c}_s$ and $\mathbf{c}_f$, respectively. The much simpler isotropic constitutive relationships for a porous isotropic medium are

$$(1-\phi)\overline{\mathbf{T}}_s = \left[\frac{\kappa_s[(1-\phi)\kappa_f + \phi\kappa_{\rm fr}] - \kappa_{\rm fr}\kappa_f}{\phi\kappa_s + (1-\phi)\kappa_f - \kappa_{\rm fr}\kappa_f/\kappa_s}\,\boldsymbol{\nabla}\cdot\overline{\mathbf{u}}_s + \frac{(1-\phi)\kappa_s\kappa_f - \kappa_{\rm fr}\kappa_f}{\phi\kappa_s + (1-\phi)\kappa_f - \kappa_{\rm fr}\kappa_f/\kappa_s}\,\boldsymbol{\nabla}\cdot\overline{\mathbf{w}}\right]\mathbf{I} + 2\mu_{\rm fr}(t) * \overline{\mathbf{d}}_s, \tag{171}$$

and

$$\phi\overline{\mathbf{T}}_f = \phi\left[\frac{\kappa_s\kappa_f}{\phi\kappa_s + (1-\phi)\kappa_f - \kappa_{\rm fr}\kappa_f/\kappa_s}\,\boldsymbol{\nabla}\cdot\overline{\mathbf{w}} + \frac{\kappa_f(\kappa_s - \kappa_{\rm fr})}{\phi\kappa_s + (1-\phi)\kappa_f - \kappa_{\rm fr}\kappa_f/\kappa_s}\,\boldsymbol{\nabla}\cdot\overline{\mathbf{u}}_s\right]\mathbf{I}. \tag{172}$$

Alternatively, we may use the macroscopic equations of motion in terms of $\overline{\mathbf{u}}_s$ and $\overline{\mathbf{w}}$ (the Biot formulation)

$$\overline{\rho}\partial_t^2\overline{\mathbf{u}}_s + \rho_f\partial_t^2\overline{\mathbf{w}} = \boldsymbol{\nabla}\cdot\overline{\mathbf{T}}, \tag{173}$$

$$m\partial_t^2\overline{\mathbf{w}} + \rho_f\partial_t^2\overline{\mathbf{u}}_s + \mathbf{b}(t)(*\cdot)\partial_t\overline{\mathbf{w}} = \boldsymbol{\nabla}\cdot\overline{\mathbf{T}}_f, \tag{174}$$

where $m = \rho_f c/\phi$, c denotes the tortuosity. In this case the isotropic constitutive relationships are

$$\overline{\mathbf{T}} = (B\boldsymbol{\nabla}\cdot\overline{\mathbf{u}}_s + C\boldsymbol{\nabla}\cdot\overline{\mathbf{w}})\,\mathbf{I} + 2\mu_{\rm fr}(t) * \overline{\mathbf{d}}_s, \tag{175}$$

and

$$\overline{\mathbf{T}}_f = -\overline{p}_f\mathbf{I} = (C\boldsymbol{\nabla}\cdot\overline{\mathbf{u}}_s + M\boldsymbol{\nabla}\cdot\overline{\mathbf{w}})\,\mathbf{I}, \tag{176}$$

with $B = H - \frac{4}{3}\mu_{\rm fr}$ and where the coefficients H, C and M are defined in (126)–(128).

Finally, we add to this set of equations the expression for the relative change in porosity:

$$\Delta\ln\phi = -\overline{\mathbf{u}}_s\cdot\boldsymbol{\nabla}\ln\phi + \left[\frac{(1-\phi)\kappa_f - \kappa_f\kappa_{\rm fr}/\kappa_s}{\phi\kappa_s + (1-\phi)\kappa_f - \kappa_{\rm fr}\kappa_f/\kappa_s}\right][(\kappa_s/\kappa_f)\boldsymbol{\nabla}\cdot\overline{\mathbf{u}}_s - \boldsymbol{\nabla}\cdot\overline{\mathbf{u}}_f - (\overline{\mathbf{u}}_f - \overline{\mathbf{u}}_s)\cdot\boldsymbol{\nabla}\ln\phi]. \tag{177}$$

Given the explicit expression for the change in porosity (177), we may now use (39) and (41) to obtain the corresponding changes in the solid and fluid densities induced by the motions:

$$\Delta\ln\rho_s = -\Delta\ln(1-\phi) - \overline{\mathbf{u}}_s\cdot\boldsymbol{\nabla}\ln(1-\phi) - \boldsymbol{\nabla}\cdot\overline{\mathbf{u}}_s - \overline{\mathbf{u}}_s\cdot\boldsymbol{\nabla}\ln\rho_s, \tag{178}$$

$$\Delta\ln\rho_f = -\Delta\ln\phi - \overline{\mathbf{u}}_f\cdot\boldsymbol{\nabla}\ln\phi - \boldsymbol{\nabla}\cdot\overline{\mathbf{u}}_f - \overline{\mathbf{u}}_f\cdot\boldsymbol{\nabla}\ln\rho_f. \tag{179}$$

If the background density and porosity are constant, the changes in porosity (177), solid density (178) and fluid density (179) reduce to

$$\Delta\ln\phi = \left[\frac{(1-\phi)\kappa_f - \kappa_f\kappa_{\rm fr}/\kappa_s}{\phi\kappa_s + (1-\phi)\kappa_f - \kappa_{\rm fr}\kappa_f/\kappa_s}\right][(\kappa_s/\kappa_f)\boldsymbol{\nabla}\cdot\overline{\mathbf{u}}_s - \boldsymbol{\nabla}\cdot\overline{\mathbf{u}}_f], \tag{180}$$

$$\Delta\ln\rho_s = \frac{\phi}{1-\phi}\,\Delta\ln\phi - \boldsymbol{\nabla}\cdot\overline{\mathbf{u}}_s, \tag{181}$$

$$\Delta\ln\rho_f = -\Delta\ln\phi - \boldsymbol{\nabla}\cdot\overline{\mathbf{u}}_f. \tag{182}$$

10 DILATATIONAL AND ROTATIONAL WAVE SPEEDS

In this section, we determine the dilatational and rotational wave speeds in terms of the properties of a homogeneous porous medium. The results in this section demonstrate the existence of two compressional waves, a fast and a slow P wave, plus a shear wave. In subsequent benchmarks against semi-analytical reference solutions, we will see numerous examples of the propagation and interaction of all three types of waves.

In the system $(\overline{\mathbf{u}}_s, \overline{\mathbf{w}})$, we recall that the equations of motion for the solid and for the fluid relative to the solid are

$$(\overline{\rho} - \phi\rho_f/c)\partial_t^2\overline{\mathbf{u}}_s = \boldsymbol{\nabla}\cdot\overline{\mathbf{T}} - \frac{\phi}{c}\boldsymbol{\nabla}\cdot\overline{\mathbf{T}}_f + \frac{\phi}{c}b(t) * \partial_t\overline{\mathbf{w}}, \tag{183}$$

$$\frac{\rho_f c\overline{\rho} - \phi\rho_f^2}{\phi\overline{\rho}}\partial_t^2\overline{\mathbf{w}} = \boldsymbol{\nabla}\cdot\overline{\mathbf{T}}_f - \frac{\rho_f}{\overline{\rho}}\boldsymbol{\nabla}\cdot\overline{\mathbf{T}} - b(t) * \partial_t\overline{\mathbf{w}}, \tag{184}$$

with

$$\overline{\mathbf{T}} = (B\boldsymbol{\nabla}\overline{\mathbf{u}}_s + C\boldsymbol{\nabla}\cdot\overline{\mathbf{w}})\,\mathbf{I} + 2\mu_{\mathrm{fr}}(t) * \overline{\mathbf{d}}_s, \tag{185}$$

$$\overline{\mathbf{T}}_f = (C\boldsymbol{\nabla}\cdot\overline{\mathbf{u}}_s + M\boldsymbol{\nabla}\cdot\overline{\mathbf{w}})\,\mathbf{I}. \tag{186}$$

Note that since we are considering homogeneous, isotropic properties, the permeability is a simple scalar, $\mathbf{k} = k\,\mathbf{I}$, and thus we only need to consider a scalar viscous relaxation function

$$b(t) = \eta_f k^{-1}\left[1 - \sum_{\ell=1}^{L'}(1 - \theta^{\epsilon\ell}/\theta^{\sigma\ell})\exp(-t/\theta^{\sigma\ell})\right]H(t). \tag{187}$$

We now introduce the classic decomposition of the displacements in terms of their dilatational and rotational components by using the operations div and curl, such that

$$\boldsymbol{\nabla}\cdot\overline{\mathbf{u}}_s = e, \tag{188}$$

$$\boldsymbol{\nabla}\times\overline{\mathbf{u}}_s = \boldsymbol{\Omega}, \tag{189}$$

$$\boldsymbol{\nabla}\cdot\overline{\mathbf{w}} = \varsigma \tag{190}$$

and

$$\boldsymbol{\nabla}\times\overline{\mathbf{w}} = \boldsymbol{\psi}. \tag{191}$$

The equations governing the propagation of dilatational and rotational waves are obtained by applying the divergence and curl operations, respectively, to (183) and (184).

10.1 Dilatational wave propagation

Applying the divergence operation to (183) and (184), using the definitions (185) and (186), and assuming constant material properties yields

$$(\overline{\rho} - \phi\rho_f/c)\partial_t^2 e = \boldsymbol{\nabla}^2\left\{\left[B + \frac{4}{3}\mu_{\mathrm{fr}}(t)\right]e + C\varsigma\right\} - \frac{\phi}{c}\boldsymbol{\nabla}^2(Ce + M\varsigma) + \frac{\phi}{c}b(t) * \partial_t\varsigma, \tag{192}$$

$$\frac{\rho_f c\overline{\rho} - \phi\rho_f^2}{\phi\overline{\rho}}\partial_t^2\varsigma = \boldsymbol{\nabla}^2(Ce + M\varsigma) - \frac{\rho_f}{\overline{\rho}}\boldsymbol{\nabla}^2\left[\left(B + \frac{4}{3}\mu_{\mathrm{fr}}(t)\right)e + C\varsigma\right] - b(t) * \partial_t\varsigma. \tag{193}$$

Assuming plane wave propagation in the x direction, the solutions to these equations are written as

$$e = A_1\exp[i(lx + \omega t)], \tag{194}$$

and

$$\varsigma = A_2\exp[i(lx + \omega t)], \tag{195}$$

where ω denotes the real angular frequency, l the complex wavenumber and $z_p = \omega/l$ the complex speed. The frequency-domain viscous operator $b(\omega)$ has the form (Carcione 2007)

$$b(\omega) = \eta_f k^{-1}\left[1 - L' + \sum_{\ell=1}^{L'}\left(\frac{1 + i\omega\theta^{\epsilon\ell}}{1 + i\omega\theta^{\sigma\ell}}\right)\right] \tag{196}$$

and the frequency domain shear modulus has the form (Carcione *et al.* 1988a)

$$\mu_{\mathrm{fr}}(\omega) = \mu_{\mathrm{fr}}^R\left[1 - L + \sum_{\ell=1}^{L}\left(\frac{1 + i\omega\tau^{\epsilon\ell}}{1 + i\omega\tau^{\sigma\ell}}\right)\right]. \tag{197}$$

Upon substituting (194) and (195) in (192) and (193), we obtain

$$(\overline{\rho}-\phi\rho_f/c)A_1\omega^2=\left[B+\frac{4}{3}\mu_{\rm fr}(\omega)\right]A_1l^2+CA_2l^2-\frac{\phi}{c}(CA_1l^2+MA_2l^2)-i\frac{\phi}{c}b(\omega)A_2\omega \tag{198}$$

and

$$\frac{\rho_f c\overline{\rho}-\phi\rho_f^2}{\phi\overline{\rho}}A_2\omega^2=CA_1l^2+MA_2l^2-\frac{\rho_f}{\overline{\rho}}\left\{\left[B+\frac{4}{3}\mu_{\rm fr}(\omega)\right]A_1l^2+CA_2l^2\right\}+ib(\omega)A_2\omega. \tag{199}$$

Eliminating A_1 and A_2 gives an equation for the speed, z_p:

$$\left[\overline{\rho}-\frac{\phi\rho_f}{c}+i\frac{b(\omega)}{\omega}\frac{\phi\overline{\rho}}{c\rho_f}\right]z_p^4-\left\{\left[B+\frac{4}{3}\mu_{\rm fr}(\omega)\right]+M\frac{\phi\overline{\rho}}{c\rho_f}-\frac{2\phi}{c}C+i\frac{b(\omega)}{\omega}\frac{\phi}{c\rho_f}\left[B+\frac{4}{3}\mu_{\rm fr}(\omega)\right]\right\}z_p^2$$
$$+\frac{\phi}{c\rho_f}\left\{\left[B+\frac{4}{3}\mu_{\rm fr}(\omega)\right]M-C^2\right\}=0. \tag{200}$$

This equation has two complex roots:

$$z_p^2=\frac{\left\{B+\frac{4}{3}\mu_{\rm fr}(\omega)+M\frac{\phi\overline{\rho}}{c\rho_f}-\frac{2\phi}{c}C+i\frac{b(\omega)}{\omega}\frac{\phi}{c\rho_f}\left[B+\frac{4}{3}\mu_{\rm fr}(\omega)\right]\right\}}{2\left[\overline{\rho}-\frac{\phi\rho_f}{c}+i\frac{b(\omega)}{\omega}\frac{\phi\overline{\rho}}{c\rho_f}\right]}$$
$$\frac{\pm\sqrt{\left\{B+\frac{4}{3}\mu_{\rm fr}(\omega)+M\frac{\phi\overline{\rho}}{c\rho_f}-\frac{2\phi}{c}C+i\frac{b(\omega)}{\omega}\frac{\phi}{c\rho_f}\left[B+\frac{4}{3}\mu_{\rm fr}(\omega)\right]\right\}^2-4\left[\overline{\rho}-\frac{\phi\rho_f}{c}+i\frac{b(\omega)}{\omega}\frac{\phi\overline{\rho}}{c\rho_f}\right]\frac{\phi}{c\rho_f}\left\{\left[B+\frac{4}{3}\mu_{\rm fr}(\omega)\right]M-C^2\right\}}}{2\left[\overline{\rho}-\frac{\phi\rho_f}{c}+i\frac{b(\omega)}{\omega}\frac{\phi\overline{\rho}}{c\rho_f}\right]}. \tag{201}$$

We denote these two roots $z_{p\rm I}$ and $z_{p\rm II}$, with $z_{p\rm I}>z_{p\rm II}$. They correspond to the complex wave speeds associated with a fast dilatational P wave when the solid and the fluid move in-phase, and a slow dilatation P wave when the solid and the fluid move out-of-phase (Biot 1956a; Carcione 2007).

The phase speeds of the fast and slow dilatational P waves are defined as the angular frequency, ω, divided by the real part of the complex wavenumber, l, that is,

$$c_{p\rm I}=\left[{\rm Re}(z_{p\rm I}^{-1})\right]^{-1},\quad c_{p\rm II}=\left[{\rm Re}\left(z_{p\rm II}^{-1}\right)\right]^{-1}. \tag{202}$$

The corresponding inverse quality factors are defined as

$$Q_{p\rm I}^{-1}=\frac{{\rm Im}(z_{p\rm I}^2)}{{\rm Re}(z_{p\rm I}^2)},\quad Q_{p\rm II}^{-1}=\frac{{\rm Im}(z_{p\rm II}^2)}{{\rm Re}(z_{p\rm II}^2)}. \tag{203}$$

At this point we compare our expressions for the dilatational phase speeds and quality factors with those derived by Carcione & Quiroga-Goode (1996) in the case of a poroacoustic medium (i.e. $\mu_{\rm fr}=0$), considering a porosity $\phi=0.3$, a viscosity $\eta_f=0.001$ Pa s, and a homogeneous permeability $k=1\times10^{-10}$ m^2 ($f_c=452$ kHz). The remaining properties are summarized in Table 2. Figs 3(1) and (2) show the phase speeds and inverse quality factors, respectively, of the fast P and slow P waves as a function of frequency using the low-frequency theory, that is, **b** is defined by (147). We find good agreement between our formulation and that of Carcione & Quiroga-Goode (1996). Note the diffusive behaviour and quasi-static character of the slow P wave at low-frequencies, when the wave is highly attenuated due to viscous damping.

Finally, note that in the absence of viscosity, that is, when $\eta_f=0$, the fast and slow dilatational wave speeds are determined by

$$c_p^2=\frac{\left[B+\frac{4}{3}\mu_{\rm fr}(\omega)+M\frac{\phi\overline{\rho}}{c\rho_f}-\frac{2\phi}{c}C\right]}{2\left(\overline{\rho}-\frac{\phi\rho_f}{c}\right)}$$
$$\frac{\pm\sqrt{\left[B+\frac{4}{3}\mu_{\rm fr}(\omega)+M\frac{\phi\overline{\rho}}{c\rho_f}-\frac{2\phi}{c}C\right]^2-4\left(\overline{\rho}-\frac{\phi\rho_f}{c}\right)\frac{\phi}{c\rho_f}\left\{\left[B+\frac{4}{3}\mu_{\rm fr}(\omega)\right]M-C^2\right\}}}{2\left(\overline{\rho}-\frac{\phi\rho_f}{c}\right)}. \tag{204}$$

10.2 Rotational wave propagation

Applying the curl operation to (183) and (184) and assuming constant material properties yields

$$(\overline{\rho}-\phi\rho_f/c)\partial_t^2\boldsymbol{\Omega}=\mu_{\rm fr}(t)*\nabla^2\boldsymbol{\Omega}+\frac{\phi}{c}b(t)*\partial_t\boldsymbol{\psi}, \tag{205}$$

$$\frac{\rho_f c\overline{\rho}-\phi\rho_f^2}{\phi\overline{\rho}}\partial_t^2\boldsymbol{\psi}=-\frac{\rho_f}{\overline{\rho}}\mu_{\rm fr}(t)*\nabla^2\boldsymbol{\Omega}-b(t)*\partial_t\boldsymbol{\psi}. \tag{206}$$

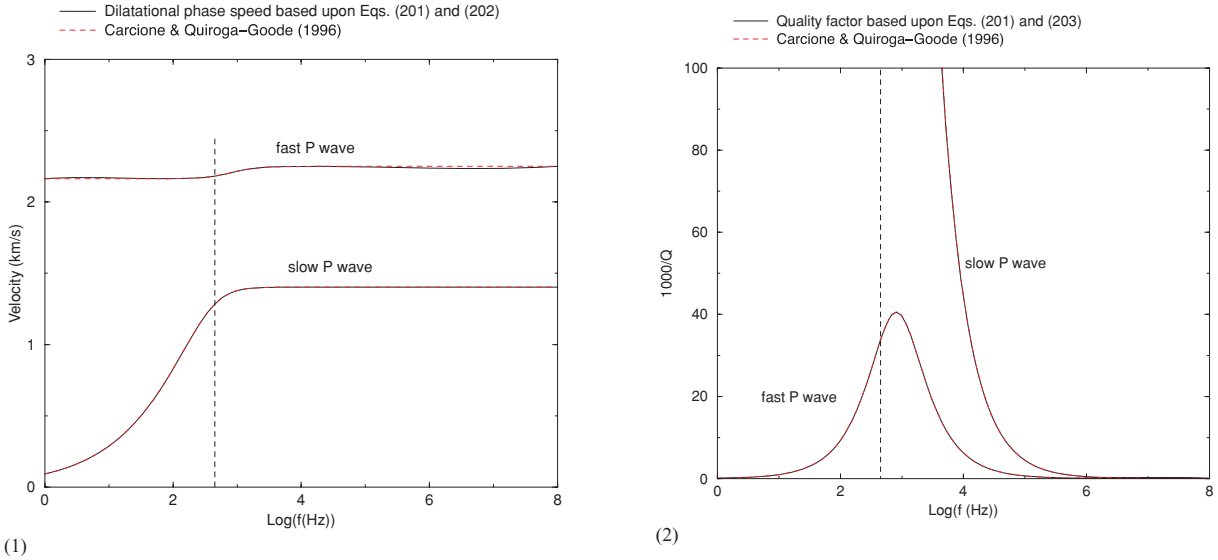

Figure 3. (1) Dilatational phase speeds and (2) inverse quality factors of the fast and slow *P* waves as a function of frequency using the low-frequency theory (i.e. **b** is defined by 147). The vertical dashed line is the characteristic frequency, f_c, which indicates the upper limit for the validity of the low-frequency theory. Our formulation is in good agreement with that of Carcione & Quiroga-Goode (1996). Note the diffusive behaviour and quasi-static character of the slow *P* wave at low-frequencies, when the wave is highly attenuated due to viscous damping.

Without loss of generality, we write the solutions of these equations for plane wave propagation in the x direction as

$$\Omega = B_1 \exp[i(lx + \omega t)], \tag{207}$$

and

$$\psi = B_2 \exp[i(lx + \omega t)], \tag{208}$$

where the complex speed of these waves is $z_s = \omega/l$.

Upon substituting (207) and (208) in (205) and (206), we obtain

$$(\overline{\rho} - \phi\rho_f/c)B_1\omega^2 = \mu_{\rm fr}(\omega)l^2 B_1 - i\frac{\phi}{c}b(\omega)B_2\omega \tag{209}$$

and

$$\frac{\rho_f c\overline{\rho} - \phi\rho_f^2}{\phi\overline{\rho}}B_2\omega^2 = -\frac{\rho_f}{\overline{\rho}}\mu_{\rm fr}(\omega)l^2 B_1 + ib(\omega)B_2\omega. \tag{210}$$

Eliminating B_1 and B_2 gives an equation for the complex speed, z_s, which after simplification may be expressed as:

$$z_s^2 = \frac{\mu_{\rm fr}(\omega)}{\overline{\rho} - \frac{\phi\rho_f}{c}} + \frac{\frac{\phi\rho_f}{c\overline{\rho}}\frac{b(\omega)}{\omega}\left[i\frac{\rho_f c\overline{\rho}-\phi\rho_f^2}{\phi\overline{\rho}} + \frac{b(\omega)}{\omega}\right]\mu_{\rm fr}(\omega)}{\left(\frac{\rho_f c\overline{\rho}-\phi\rho_f^2}{\phi\overline{\rho}}\right)^2 + \left[\frac{b(\omega)}{\omega}\right]^2}. \tag{211}$$

We thus note the presence of only one type of shear wave, with phase speed

$$c_s = \left[\mathrm{Re}\left(z_s^{-1}\right)\right]^{-1}, \tag{212}$$

and inverse quality factor

$$Q_s^{-1} = \frac{\mathrm{Im}(z_s^2)}{\mathrm{Re}(z_s^2)}. \tag{213}$$

In the absence of viscosity, when $\eta_f = 0$, we have

$$c_s^2 = \frac{\mu_{\rm fr}(\omega)}{\overline{\rho} - \phi\rho_f/c}. \tag{214}$$

Finally, note also the relation between the solid rotation, $\mathbf{\Omega}$, and the fluid rotation relative to the solid, $\boldsymbol{\psi}$:

$$\boldsymbol{\psi} = -\frac{\phi}{c}\,\mathbf{\Omega}. \tag{215}$$

10.3 Practical considerations

In practice, one may have experimental data that determine the wave speeds $c_{p\mathrm{I}}$, $c_{p\mathrm{II}}$ and c_s and the inverse quality factors $Q_{p\mathrm{I}}^{-1}$, $Q_{p\mathrm{II}}^{-1}$ and Q_s^{-1} as a function of frequency. From a numerical perspective, this frequency dependence may be captured by prescribing the appropriate stress and strain relaxation times $\theta^{\epsilon\ell}$ and $\theta^{\sigma\ell}$ for the viscous operator $b(\omega)$ in (196), and the stress and strain relaxation times $\tau^{\epsilon\ell}$ and $\tau^{\sigma\ell}$ for the frame shear modulus in (197). This is similar to the determination of the stress and strain relaxation times needed to fit an absorption band solid for anelastic problems (see e.g. Komatitsch & Tromp 1999).

11 DISCRETIZATION

In the following, we first seek to establish the weak form of the governing equations. Subsequently, we determine the spatial discretization of this variational problem using a SEM (Komatitsch 1997; Komatitsch & Tromp 1999). Finally, we discuss the assembly stage and time marching. We will see that we obtain a diagonal mass matrix, which implies that the SEM provides the same numerical benefits for simulations of poroelastic wave propagation as it does for acoustic and elastic problems.

To avoid mathematical complications, we do not incorporate attenuation and frequency-dependent viscous processes in the discretization that follows. But as discussed in previous sections, these effects may be readily accommodated based upon a simple memory variable approach (see e.g. Komatitsch & Tromp 1999, 2002; Carcione 1993, 2007).

11.1 Weak form

We consider the set of equations in terms of $\overline{\mathbf{u}}_s$ and $\overline{\mathbf{w}}$, which naturally takes into account gradients in porosity, with an explicit source term:

$$\overline{\rho}\partial_t^2\overline{\mathbf{u}}_s + \rho_f\partial_t^2\overline{\mathbf{w}} = \boldsymbol{\nabla}\cdot\overline{\mathbf{T}} + \mathbf{f}, \tag{216}$$

$$m\partial_t^2\overline{\mathbf{w}} + \rho_f\partial_t^2\overline{\mathbf{u}}_s + \eta_f\mathbf{k}^{-1}\cdot\partial_t\overline{\mathbf{w}} = \boldsymbol{\nabla}\cdot\overline{\mathbf{T}}_f + \mathbf{f}, \tag{217}$$

where we have introduced the following constitutive relationships for an isotropic medium

$$\overline{\mathbf{T}} = \mathbf{G}:\boldsymbol{\nabla}\overline{\mathbf{u}}_s + C\boldsymbol{\nabla}\cdot\overline{\mathbf{w}}\,\mathbf{I}, \tag{218}$$

and

$$\overline{\mathbf{T}}_f = -\overline{p}_f\mathbf{I} = (C\boldsymbol{\nabla}\cdot\overline{\mathbf{u}}_s + M\boldsymbol{\nabla}\cdot\overline{\mathbf{w}})\,\mathbf{I}. \tag{219}$$

For convenience we have defined a tensor $\mathbf{G}$ whose elements are

$$G_{ijkl} = (H - 2\mu_{\mathrm{fr}})\delta_{ij}\delta_{kl} + \mu_{\mathrm{fr}}(\delta_{ik}\delta_{jl} + \delta_{il}\delta_{jk}). \tag{220}$$

This choice allows us to avoid cumbersome notation and has the additional benefit of naturally extending the theory to more general anisotropic problems.

The macroscopic source term $\mathbf{f}$ excites the wave motion and is linearly partitioned between the solid and the fluid phase assuming a uniform distribution of the force within the porous medium. In the context of an earthquake, it is written in terms of a moment tensor $\mathbf{M}$, as (e.g. Dahlen & Tromp 1998)

$$\mathbf{f} = -\mathbf{M}\cdot\boldsymbol{\nabla}\delta(\mathbf{x} - \mathbf{x}_s)S(t), \tag{221}$$

where $\mathbf{x}_s$ refers to the point source location, $\delta(\mathbf{x} - \mathbf{x}_s)$ is the Dirac delta distribution located at $\mathbf{x}_s$ and $S(t)$ is the source time function.

We write (216) and (217) in a weak form by dotting each equation with arbitrary test vectors $\tilde{\mathbf{u}}$ and $\tilde{\mathbf{w}}$, respectively, and integrating over the model volume Ω:

$$\int_\Omega \overline{\rho}\tilde{\mathbf{u}}\cdot\partial_t^2\overline{\mathbf{u}}_s\,\mathrm{d}^3\mathbf{x} + \int_\Omega \rho_f\tilde{\mathbf{u}}\cdot\partial_t^2\overline{\mathbf{w}}\,\mathrm{d}^3\mathbf{x} = \int_\Omega \tilde{\mathbf{u}}:\boldsymbol{\nabla}\overline{\mathbf{T}}\,\mathrm{d}^3\mathbf{x} + \int_\Omega \tilde{\mathbf{u}}\cdot\mathbf{f}\,\mathrm{d}^3\mathbf{x}, \tag{222}$$

$$\int_\Omega m\tilde{\mathbf{w}}\cdot\partial_t^2\overline{\mathbf{w}}\,\mathrm{d}^3\mathbf{x} + \int_\Omega \rho_f\tilde{\mathbf{w}}\cdot\partial_t^2\overline{\mathbf{u}}_s\,\mathrm{d}^3\mathbf{x} + \int_\Omega \eta_f\tilde{\mathbf{w}}\cdot(\mathbf{k}^{-1}\cdot\partial_t\overline{\mathbf{w}})\,\mathrm{d}^3\mathbf{x} = \int_\Omega \tilde{\mathbf{w}}:\boldsymbol{\nabla}\overline{\mathbf{T}}_f\,\mathrm{d}^3\mathbf{x} + \int_\Omega \tilde{\mathbf{w}}\cdot\mathbf{f}\,\mathrm{d}^3\mathbf{x}. \tag{223}$$

Integrating by parts and replacing the source by its explicit expression (221) yields

$$\int_\Omega \overline{\rho}\tilde{\mathbf{u}}\cdot\partial_t^2\overline{\mathbf{u}}_s\,\mathrm{d}^3\mathbf{x} + \int_\Omega \rho_f\tilde{\mathbf{u}}\cdot\partial_t^2\overline{\mathbf{w}}\,\mathrm{d}^3\mathbf{x} = -\int_\Omega \boldsymbol{\nabla}\tilde{\mathbf{u}}:\overline{\mathbf{T}}\,\mathrm{d}^3\mathbf{x} + \int_\Gamma \hat{\mathbf{n}}\cdot\overline{\mathbf{T}}\cdot\tilde{\mathbf{u}}\,\mathrm{d}^2\mathbf{x} + \mathbf{M}:\boldsymbol{\nabla}\tilde{\mathbf{u}}(\mathbf{x}_s)S(t), \tag{224}$$

$$\begin{aligned}\int_\Omega m\tilde{\mathbf{w}}\cdot\partial_t^2\overline{\mathbf{w}}\,\mathrm{d}^3\mathbf{x} + \int_\Omega \rho_f\tilde{\mathbf{w}}\cdot\partial_t^2\overline{\mathbf{u}}_s\,\mathrm{d}^3\mathbf{x} + \int_\Omega \eta_f\tilde{\mathbf{w}}\cdot(\mathbf{k}^{-1}\cdot\partial_t\overline{\mathbf{w}})\,\mathrm{d}^3\mathbf{x} &= -\int_\Omega \boldsymbol{\nabla}\tilde{\mathbf{w}}:\overline{\mathbf{T}}_f\,\mathrm{d}^3\mathbf{x}\\ &\quad + \int_\Gamma \hat{\mathbf{n}}\cdot\overline{\mathbf{T}}_f\cdot\tilde{\mathbf{w}}\,\mathrm{d}^2\mathbf{x} + \mathbf{M}:\boldsymbol{\nabla}\tilde{\mathbf{w}}(\mathbf{x}_s)S(t),\end{aligned} \tag{225}$$

where Γ is comprised of the free surface, the interfaces between acoustic–poroelastic, elastic-poroelastic and poroelastic–poroelastic domains, and the absorbing boundaries. Note that this definition of the surface Γ explicitly allows for first-order discontinuities in the model parameters, including the porosity. (224) and (225) represent the basis for the discretization of our problem developed in the following sections.

11.2 Assembly and temporal discretization

Details of the SEM discretization may be found in Komatitsch & Vilotte (1998), Komatitsch & Tromp (1999) and Komatitsch *et al.* (2005). Integration at the elemental level of (224) and (225) leads to a set of mass and stiffness matrices and source vectors similar to the elastic case. In addition, we define a damping matrix which involves the viscous damping force present in (225). Detailed expressions for the mass and damping matrices may be found in Appendix B. One should note that, similar to the elastic case, the mass matrices are diagonal.

We need to distinguish between the 'local mesh' of GLL integration and interpolation points defining one element (using as four indices the three GLL labels α, β and γ plus an element label Ω_e), and the 'global mesh' of all the gridpoints of the system (using a single index I). We also need to take into account the fact that integration points which lie on the sides, edges, or corners of an element are shared amongst neighbouring elements. Let us denote the mapping between the local mesh and the global mesh as

$$(\alpha, \beta, \gamma, \Omega_e) \rightarrow (I). \tag{226}$$

The contributions from all elements which share a global gridpoint need to be summed. This process is referred to as the 'assembly' of the system, and routines used to perform this task are available from FEM modelling. If we use $\mathbf{U}$ to denote the solid displacement vector of the global system and $\mathbf{W}$ to denote the relative fluid displacement vector of the global system (i.e. $\mathbf{U}$ and $\mathbf{W}$ contain the displacement vectors at all the gridpoints in the global mesh), the discretized set of equations may be written in the form

$$\mathbf{M}_1\ddot{\mathbf{U}} + \mathbf{M}_2\ddot{\mathbf{W}} + \mathbf{K}_1\mathbf{U} + \mathbf{K}_2\mathbf{W} = \mathbf{F} \tag{227}$$

for the solid, and

$$\mathbf{M}_3\ddot{\mathbf{W}} + \mathbf{M}_4\ddot{\mathbf{U}} + \mathbf{D}\dot{\mathbf{W}} + \mathbf{K}_3\mathbf{W} + \mathbf{K}_4\mathbf{U} = \mathbf{F} \tag{228}$$

for the fluid, where $\mathbf{M}_1$, $\mathbf{M}_2$, $\mathbf{M}_3$ and $\mathbf{M}_4$ are the global diagonal mass matrices; $\mathbf{K}_1$, $\mathbf{K}_2$, $\mathbf{K}_3$ and $\mathbf{K}_4$ are the global stiffness matrices; $\mathbf{D}$ is the global damping matrix and $\mathbf{F}$ is the global source vector. Note that, because we choose the same test vectors, $\tilde{\mathbf{u}}$ and $\tilde{\mathbf{w}}$, for the solid part and for the fluid part, respectively, $\mathbf{M}_4 = \mathbf{M}_2$ and $\mathbf{K}_4 = \mathbf{K}_2$. Using basic matrix algebra, (227) and (228) may be further rewritten as

$$\begin{bmatrix} \mathbf{M}^s & 0 \\ 0 & \mathbf{M}^f \end{bmatrix} \begin{bmatrix} \ddot{\mathbf{U}} \\ \ddot{\mathbf{W}} \end{bmatrix} + \begin{bmatrix} 0 & \mathbf{D}^s \\ 0 & \mathbf{D}^f \end{bmatrix} \begin{bmatrix} \dot{\mathbf{U}} \\ \dot{\mathbf{W}} \end{bmatrix} + \begin{bmatrix} \mathbf{K}_s^s & \mathbf{K}_f^s \\ \mathbf{K}_s^f & \mathbf{K}_f^f \end{bmatrix} \begin{bmatrix} \mathbf{U} \\ \mathbf{W} \end{bmatrix} = \begin{bmatrix} \mathbf{F}^s \\ \mathbf{F}^f \end{bmatrix}, \tag{229}$$

where

$$\mathbf{M}^s = \mathbf{M}_1 - \mathbf{M}_2\mathbf{M}_3^{-1}\mathbf{M}_2, \quad \mathbf{M}^f = \mathbf{M}_3 - \mathbf{M}_2\mathbf{M}_1^{-1}\mathbf{M}_2, \tag{230}$$

$$\mathbf{D}^s = -\mathbf{M}_2\mathbf{M}_3^{-1}\mathbf{D}, \quad \mathbf{D}^f = \mathbf{D}, \tag{231}$$

$$\mathbf{K}_s^s = \mathbf{K}_1 - \mathbf{M}_2\mathbf{M}_3^{-1}\mathbf{K}_2, \quad \mathbf{K}_f^s = \mathbf{K}_2 - \mathbf{M}_2\mathbf{M}_3^{-1}\mathbf{K}_3, \quad \mathbf{K}_s^f = \mathbf{K}_2 - \mathbf{M}_2\mathbf{M}_1^{-1}\mathbf{K}_1, \quad \mathbf{K}_f^f = \mathbf{K}_3 - \mathbf{M}_2\mathbf{M}_1^{-1}\mathbf{K}_2, \tag{232}$$

$$\mathbf{F}^s = \mathbf{F} - \mathbf{M}_2\mathbf{M}_3^{-1}\mathbf{F}, \quad \mathbf{F}^f = \mathbf{F} - \mathbf{M}_2\mathbf{M}_1^{-1}\mathbf{F}. \tag{233}$$

Detailed expressions for the corresponding matrix elements at the global level may be found in Appendix C. The critical observation is that the global mass matrices $\mathbf{M}^s$ and $\mathbf{M}^f$ are diagonal.

Because the system (229) is diagonal, it may be solved based upon a simple explicit time marching scheme. We use a Newmark scheme (e.g. Hughes 1987) implemented using a predictor/multicorrection technique. (C17) and (C18) provide the formulae to compute the acceleration at any given time. The predictor phase at the beginning of each time step Δt is given by

$$d^{n+1} = d^n + v^n\Delta t + \frac{1}{2}a^n(\Delta t)^2, \tag{234}$$

$$v^{n+1} = v^n + \frac{1}{2}a^n\Delta t, \tag{235}$$

$$a^{n+1} = 0, \tag{236}$$

where d is the displacement, v the velocity and a the acceleration. The corrector phase at the end of each time step is given by

$$a^{n+1} = M^{-1}\mathrm{RHS}, \tag{237}$$

$$v^{n+1} = v^{n+1} + \frac{1}{2}a^{n+1}\Delta t, \tag{238}$$

$$d^{n+1} = d^{n+1}. \tag{239}$$

12 BOUNDARY CONDITIONS

The top surface of our model is a free surface, such that in the weak formulation the integral of the traction along this boundary vanishes. We need to absorb the outgoing waves at the edges of our computational domain in order to avoid artificial reflections and to simulate an unbounded medium. To that end, we use classical first-order absorbing boundary conditions based upon a paraxial approximation (Clayton &

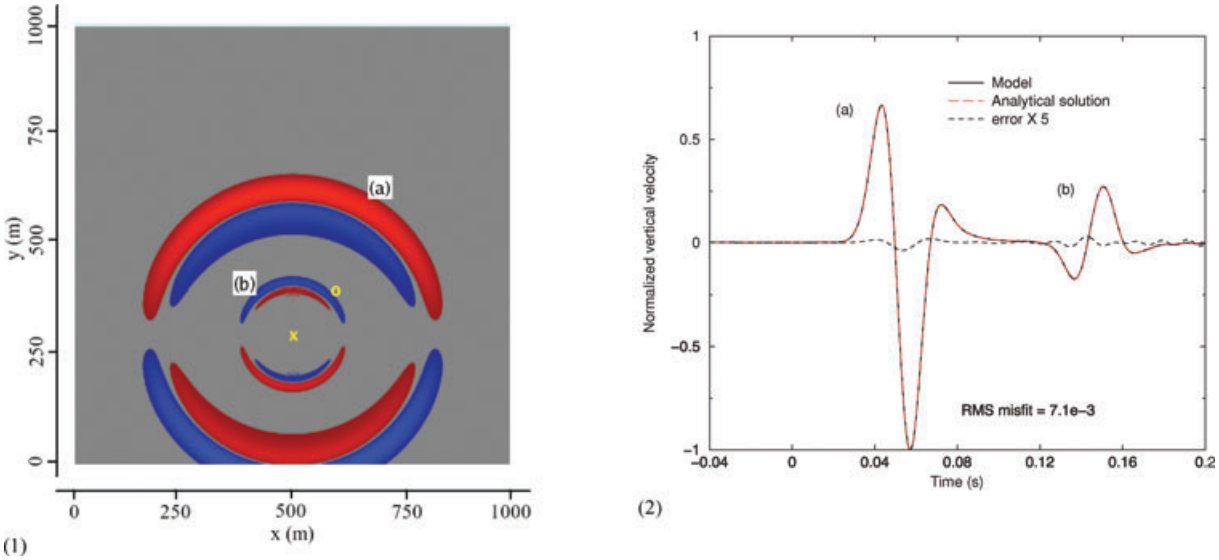

Figure 4. 2-D spectral-element simulation of wave propagation in a homogeneous porous medium whose properties are summarized in Table 1. The domain dimensions are 1000 m × 1000 m, the explosive source with a dominant frequency of 30 Hz (yellow cross) is located at $\mathbf{x}_s = (500, 300)$ and the receiver (yellow circle) at $\mathbf{x}_r = (600, 400)$. The top boundary is a free surface and the remaining three edges are absorbing boundaries. (1) Snapshot of the vertical-component macroscopic solid displacement $\overline{\mathbf{u}}_s$ at $t = 0.12$ s. The fast P (a) and slow P (b) waves may be observed. (2) Comparison of the vertical-component velocity synthetic seismograms (solid black line) to the Dai *et al.* (1995) analytical solution (dashed red line), and their difference multiplied by a factor of 5 (dashed black line). We have also noted the RMS misfit between the analytical solution and the SEM simulation, as we will do for all such comparisons in this paper.

Table 1. Poroelastic medium properties.

Variable name	Symbol	Unit	Value
Solid density	ρ_s	kg m^{-3}	2650
Fluid density	ρ_f	kg m^{-3}	880
Porosity	ϕ	–	0.1
Tortuosity	c	–	2
Solid bulk modulus	κ_s	GPa	12.2
Fluid bulk modulus	κ_f	GPa	1.985
Frame bulk modulus	κ_{fr}	GPa	9.6
Fluid viscosity	η_f	Pa s	0
Frame shear modulus	μ_{fr}	GPa	5.1
Fast P wave	$c_{p\mathrm{I}}$	m s^{-1}	2639
Slow P wave	$c_{p\mathrm{II}}$	m s^{-1}	961
S wave	c_s	m s^{-1}	1449

Engquist 1977; Engquist & Majda 1977). The associated conditions for the tractions are

$$\mathbf{t} = \bar{\rho} c_{p\mathrm{I}} (\partial_t \overline{\mathbf{u}}_s \cdot \hat{\mathbf{n}}) \hat{\mathbf{n}} + \rho_f c_{p\mathrm{II}} (\partial_t \overline{\mathbf{w}} \cdot \hat{\mathbf{n}}) \hat{\mathbf{n}} + (\bar{\rho} - \rho_f \phi / c) c_s (\mathbf{I} - \hat{\mathbf{n}}\hat{\mathbf{n}}) \cdot \partial_t \overline{\mathbf{u}}_s, \tag{240}$$

and

$$\mathbf{t}_f = \rho_f c / \phi c_{p\mathrm{II}} (\partial_t \overline{\mathbf{w}} \cdot \hat{\mathbf{n}}) \hat{\mathbf{n}} + \rho_f c_{p\mathrm{I}} (\partial_t \overline{\mathbf{u}}_s \cdot \hat{\mathbf{n}}) \hat{\mathbf{n}}. \tag{241}$$

Note that recent studies have started to adopt the perfectly matched layer (PML) methodology, first introduced for electromagnetic waves (Berenger 1994), to problems of poroelastic wave propagation (Zeng & Liu 2001b; Zeng *et al.* 2001; Martin *et al.* 2007). The PML implementation is not included in this paper but will be addressed in the near future. The boundary conditions related to domain heterogeneity (acoustic–poroelastic, poroelastic–elastic and poroelastic–poroelastic) are dealt with based upon domain decomposition, and are further discussed as they arise in subsequent sections.

13 2-D BENCHMARKS

In the following sections, we validate our implementation of poroelastic wave propagation for various 2-D models. Wave speeds in the models may be calculated based upon the results presented in Section 10. In Section 13.1, we perform a series of tests involving wave propagation in a simple homogeneous poroelastic medium. Section 13.1.1 treats propagation in the high-frequency regime for an inviscid fluid. Our SEM solution is compared to an analytical solution derived by Dai *et al.* (1995). The stability and accuracy of the implementation are further

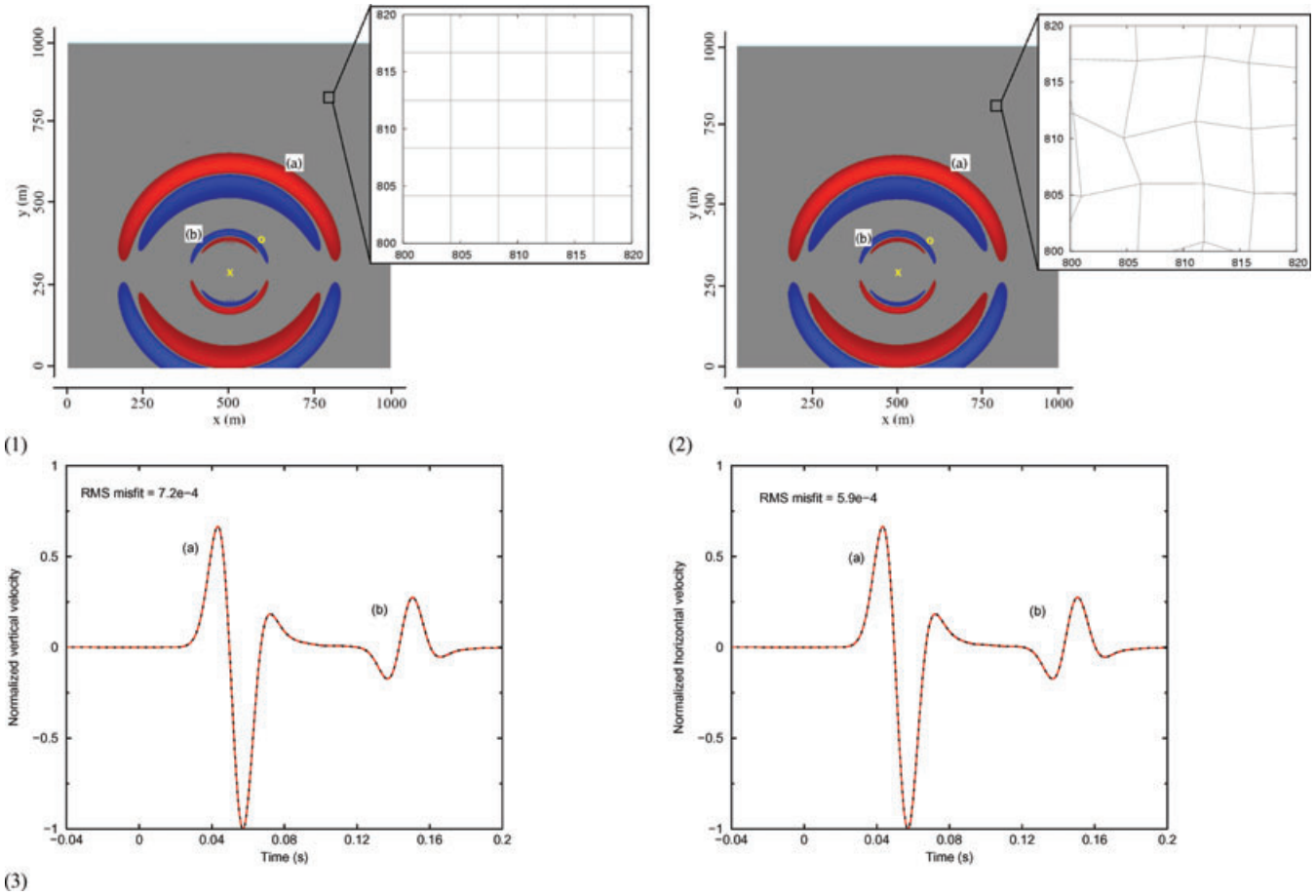

Figure 5. 2-D spectral-element simulation of wave propagation in a homogeneous porous medium whose properties are summarized in Table 1. The domain dimensions are 1000 m × 1000 m, the explosive source with a dominant frequency of 30 Hz (yellow cross) is located at $\mathbf{x}_s = (500, 300)$ and the receiver (yellow circle) at $\mathbf{x}_r = (600, 400)$. The top boundary is a free surface and the remaining three edges are absorbing boundaries. Snapshot of the vertical-component displacement at $t = 0.12$ s for (1) a reference model using a regular mesh, and (2) the same model with a randomly perturbed mesh (Courtesy of Dimitri Komatitsch). The fast P (a) and slow P (b) waves may be observed. (3) Comparison of the vertical- and horizontal-component velocity synthetic seismograms (regular mesh: solid black line, perturbed mesh: dashed red line).

illustrated in Section 13.1.2, where we present results for the same problem using a randomly deformed mesh. Sections 13.1.3 and 13.1.4 highlight viscous damping phenomena in the low- and high-frequency regimes, where we compare our SEM solutions to analytical solutions derived by Carcione & Quiroga-Goode (1996). In Section 13.2, we focus on coupling between acoustic and poroelastic waves. Finally, in Section 13.3 we deal with porosity discontinuities, and in Section 13.4 we discuss the coupling between poroelastic and elastic waves.

All of the numerical experiments are performed using Lagrange polynomials of degree 4, resulting in 25 GLL points in each element. In order to maintain stability and accuracy, we prescribe a minimum of 5 gridpoints per shortest wavelength and a Courant stability number less than 0.4.

13.1 Homogeneous porous media

13.1.1 Analytical solution: high-frequency, inviscid fluid

In order to validate our formulation, we consider a homogeneous poroelastic medium subjected to an explosion with a Gaussian source time function with a dominant frequency of 30 Hz. For an inviscid fluid ($\eta_f = 0$), we compare the numerical solution obtained based upon our SEM to the analytical solution derived by Dai *et al.* (1995). The model setup is displayed in Fig. 4(1). The poroelastic medium properties are summarized in Table 1. The vertical-component velocity seismograms obtained with the SEM and the analytical solution are compared in Fig. 4(2). The difference between the two results enhanced by a factor of 5 is also plotted, which illustrates the excellent agreement between the SEM and the analytical solution for both the fast and the slow P waves. This is further confirmed by the RMS misfit between the SEM solution and the analytical solution, as indicated in Fig. 4(2). In what follows, we will indicate this misfit for all benchmarks against analytical solutions.

Table 2. Poroacoustic medium properties.

Variable name	Symbol	Unit	Value
Solid density	ρ_s	$\mathrm{kg\,m^{-3}}$	2650
Fluid density	ρ_f	$\mathrm{kg\,m^{-3}}$	880
Porosity	ϕ	–	0.3
Tortuosity	c	–	1.2
Solid bulk modulus	κ_s	GPa	12.2
Fluid bulk modulus	κ_f	GPa	1.985
Frame bulk modulus	κ_{fr}	GPa	9.6
Fluid viscosity	η_f	Pa s	0 (0.001)
Permeability	k	$\mathrm{m^2}$	10^{-10}
Fast *P* wave	$c_{p\mathrm{I}}$	$\mathrm{m\,s^{-1}}$	2250 (2163)[a] (2250)[b,c]
Slow *P* wave	$c_{p\mathrm{II}}$	$\mathrm{m\,s^{-1}}$	1403 (476)[a] (1403)[b,c]

Note: For further details see the text in Sections 13.1.3 and 13.1.4.
[a]Viscous model in the low-frequency regime.
[b]Viscous model in the high-frequency regime using a frequency-dependent viscous correction.
[c]Viscous model in the high-frequency regime using low-frequency Biot theory.

13.1.2 Randomly perturbed mesh

In this Section we show that our implementation remains accurate even when using deformed meshes. To that end, we consider the same problem as in Section 13.1.1, but this time we employ a randomly perturbed mesh (regular mesh: Fig. 5(1), perturbed mesh: Fig. 5(2)). The perturbed mesh is obtained by randomly stretching the position of the mesh points compared to their origin (i.e. the regular mesh) from 0 ± 1.1 m (which corresponds to ± 20 per cent of the element length) in the x and z directions. Comparison of the vertical- and horizontal-component velocity synthetic seismograms confirms the accuracy and stability of our implementation. Note that the RMS misfit for the randomly perturbed mesh is only slightly larger than for the regular mesh.

13.1.3 Analytical solution: low-frequency, viscous fluid

To investigate low-frequency poroelastic wave propagation involving a viscous fluid, we use a model setup similar to that in Section 13.1.1 (Fig. 4(1)). In this case, however, the source–receiver distance is 666 m, and we use a Ricker wavelet source time function with a dominant frequency of 30 Hz. First, we compare wave propagation two models (Model A is viscous and Model B is inviscid) to illustrate the effects of viscous damping as discussed in Section 8.3. Next, we compare our viscous simulation to an analytical solution derived by Carcione & Quiroga-Goode (1996) for a poroacoustic problem, which implies that there is no shear deformation (i.e. μ_{fr} is taken to be zero). The properties of the poroacoustic medium are summarized in Table 2.

Model A is viscous with a viscosity $\eta_f = 0.001$ Pa s and an isotropic permeability $k = 10^{-10}\mathrm{m}^2$ ($f_c = 452$ Hz (151)), whereas the fluid in Model B is inviscid. Results for the two models are displayed in Figs 6(1) and (2), where we plot the solid and fluid pressures, respectively. The slow *P* wave is highly attenuated in Model A and exhibits diffusive behaviour, in agreement with the theory (Biot 1956a; Carcione & Quiroga-Goode 1996). In inviscid Model B the slow *P* wave is observed. Note the difference in the fast *P* wave traveltimes, as predicted by the analytical solution for the dilatational wave speeds in Section 10.1.

Figs 6(3) and (4) show a comparison between SEM synthetics for viscous Model A and the analytical solution derived by Carcione & Quiroga-Goode (1996), which are in good agreement. The spectral-element mesh consists of 300×260 elements, the time step is 1.25×10^{-4} s, and the total number of time steps is 6000. A challenge when dealing with wave propagation in a porous medium in the low-frequency regime is to find a stable numerical scheme that captures the diffusive behaviour of the slow *P* wave. Frequently, explicit time schemes encounter numerical stability issues, which has led to the development of alternative techniques (e.g. Discontinuous Galerking Methods, see de la Puente *et al.* 2007). The good agreement between the SEM solution for viscous Model A and the analytical solution demonstrates the stability and accuracy of our approach, which is based upon a predictor/corrector explicit time scheme and classical SEM stability criteria (Komatitsch & Vilotte 1998).

13.1.4 Analytical solution: high-frequency, viscous fluid

To address high-frequency poroelastic wave propagation involving a viscous fluid, we use a similar setup as in the previous section. The properties of the poroacoustic medium are similar to viscous Model A used in Section 13.1.3 (see Table 2). However in this case, in order to shift the simulation to the high-frequency regime, we use a Ricker wavelet source time function with a dominant frequency of 10^6 Hz and a source–receiver distance of 0.21 m. To address the change in fluid flow regime at high frequencies as described by Biot (1956b), we use the frequency-dependent correction discussed in Section 8.3.2

First, we show solid and fluid pressure seismograms in Figs 7(1) and (2), respectively, comparing results obtained using frequency-dependent viscous resistance with low-frequency Biot theory (i.e. **b** is still given by (147), the appropriate expression for Poiseuille flow). In

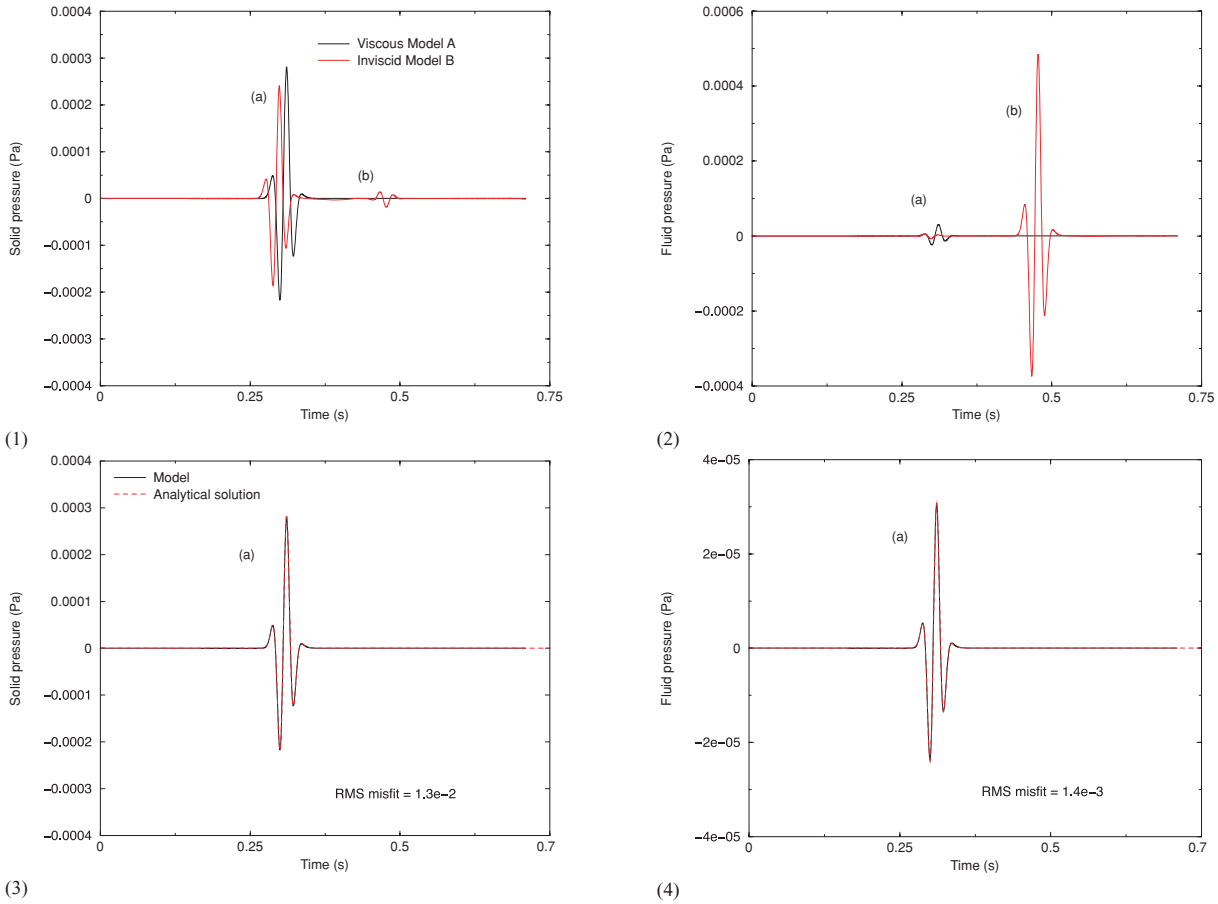

Figure 6. (1) Solid pressure and (2) fluid pressure seismograms obtained for viscous Model A in the low-frequency regime (black line; using a viscosity $\eta_f = 0.001$ Pa s and an isotropic permeability $k = 10^{-10}\,\mathrm{m}^2$, see Table 2) and inviscid Model B (red line; see Table 2). The explosive source has a dominant frequency of 30 Hz and the source–receiver distance is 666 m. The slow P wave (b) is highly attenuated due to viscous damping in Model A. Comparison of (3) solid pressure and (4) fluid pressure obtained for Model A (black line) with an analytical solution derived by Carcione & Quiroga-Goode (1996) (red dashed line).

the high-frequency domain, the slow P wave exhibits propagative behaviour. Frequency-dependent viscous resistance leads to attenuation of both the fast and slow P waves compared to low-frequency Biot theory. The attenuation is stronger for the slow P wave in the fluid. Note that the fast P wave in the solid is in-phase with respect to the fast P wave in the fluid, whereas the slow P waves are out-of-phase, as predicted by the theory. Finally, Figs 7(3) and (4) demonstrate good agreement between the frequency-dependent viscous SEM simulation and an analytical solution derived by Carcione & Quiroga-Goode (1996) using the frequency-domain viscous operator $b(w)$ defined in (196).

13.2 Coupling between acoustic and poroelastic waves

In this section we recall the equation of motion for acoustic waves and discuss coupling between an acoustic and a poroelastic medium, before presenting an application.

13.2.1 Acoustic wave equation

To describe wave propagation in an inviscid fluid, we use the formulation introduced by Chaljub & Valette (2004) and Komatitsch *et al.* (2005):

$$\rho_a \partial_t^2 \chi_a = \kappa \boldsymbol{\nabla}^2 \chi_a, \tag{242}$$

where the acoustic fluid displacement, $\mathbf{u}_a$, is expressed in terms of a scalar potential, χ_a, as $\mathbf{u}_a = \boldsymbol{\nabla}\chi_a$, and the acoustic pressure p_a is defined by $p_a = -\rho_a \partial_t^2 \chi_a$. Multiplying (242) with an arbitrary test vector $\tilde{\chi}_a$ and integrating by parts yields

$$\int_\Omega \frac{\rho_a}{\kappa} \tilde{\chi}_a \, \partial_t^2 \chi_a \, \mathrm{d}^3\mathbf{x} = -\int_\Omega \boldsymbol{\nabla}\tilde{\chi}_a \cdot \boldsymbol{\nabla}\chi_a \, \mathrm{d}^3\mathbf{x} + \int_\Gamma \tilde{\chi}_a \, \hat{\mathbf{n}} \cdot \boldsymbol{\nabla}\chi_a \, \mathrm{d}^2\mathbf{x}. \tag{243}$$

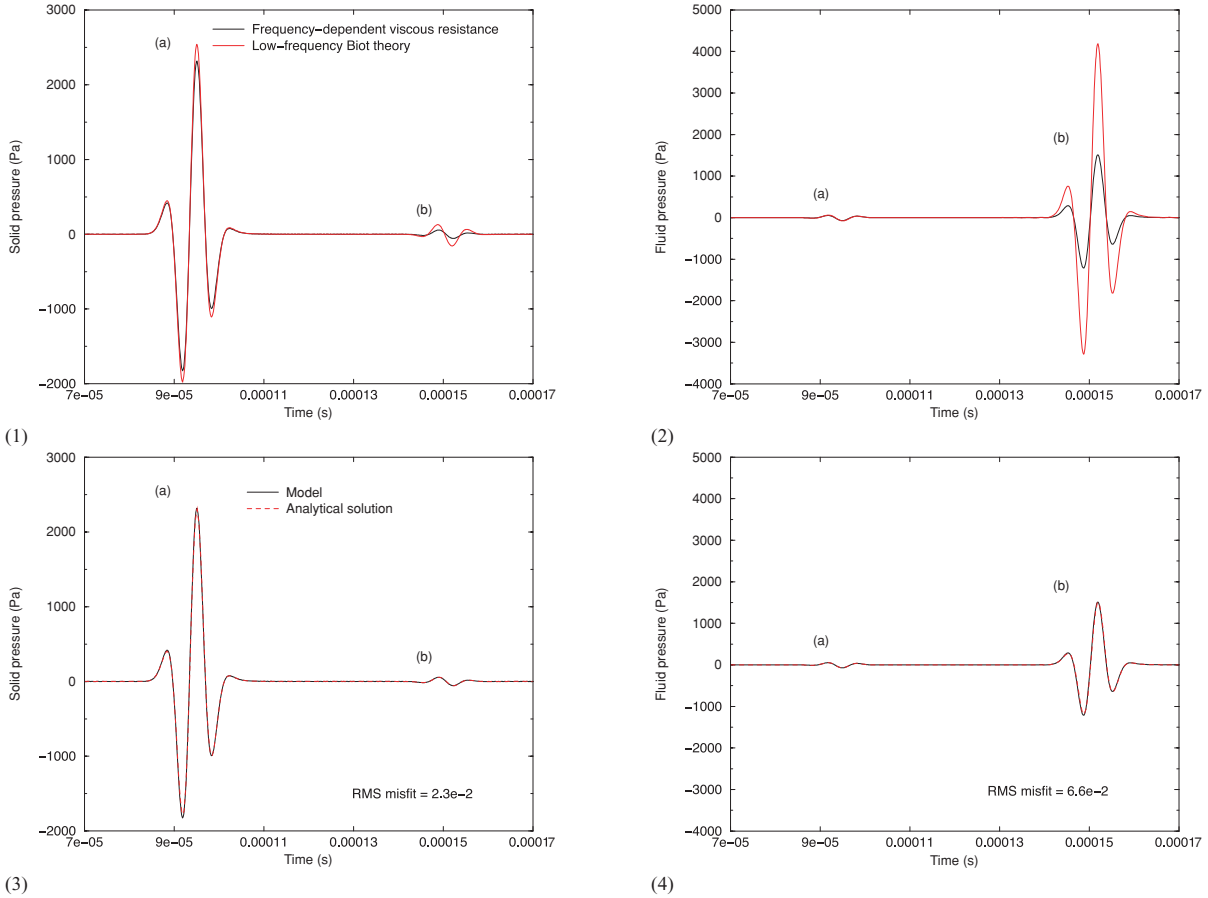

Figure 7. Pressure seismograms obtained using a viscosity $\eta_f = 0.001$ Pa s and an isotropic permeability $k = 10^{-10}$ m^2 (Table 2). The explosive source has a dominant frequency of 10^6 Hz, thus shifting the experiment to the high frequency regime ($f_c = 452$ Hz). The source–receiver distance is 0.21 m. Comparison of (1) the solid pressure and (2) the fluid pressure using the frequency-dependent viscous resistance described in Section 8.3.2 (black line; $\theta^\epsilon = 3.84 \times 10^{-4}$ s and $\theta^\sigma = 6.59 \times 10^{-5}$ s) and Biot low-frequency theory (red line; **b** is given by (147)). Compared to Biot low-frequency theory, the frequency-dependent viscous resistance leads to attenuation of both the fast P (a) and slow P (b) waves. Note that the effect is more significant for the slow P wave in the fluid phase. Comparison of (3) the solid pressure and (4) the fluid pressure using frequency-dependent viscous resistance (black line) to the analytical solution derived by Carcione & Quiroga-Goode (1996) (red dashed line).

The kinematic boundary condition at the acoustic–poroelastic interface involves free slip, so only the normal component of displacement, $\hat{\mathbf{n}} \cdot \mathbf{u}_a = \hat{\mathbf{n}} \cdot \nabla \chi_a$, needs to be continuous across the interface. Thus, the second integral on the right-hand side in (224) is replaced by

$$\int_\Gamma \hat{\mathbf{n}} \cdot \overline{\mathbf{T}} \cdot \tilde{\mathbf{u}} \, \mathrm{d}^2\mathbf{x} = -\int_\Gamma p_a \hat{\mathbf{n}} \cdot \tilde{\mathbf{u}} \, \mathrm{d}^2\mathbf{x}, \tag{244}$$

and the second integral on the right hand side in (225) by

$$\int_\Gamma \hat{\mathbf{n}} \cdot \overline{\mathbf{T}}_f \cdot \tilde{\mathbf{w}} \, \mathrm{d}^2\mathbf{x} = -\int_\Gamma p_a \hat{\mathbf{n}} \cdot \tilde{\mathbf{w}} \, \mathrm{d}^2\mathbf{x}, \tag{245}$$

that is, we exchange the tractions between the fluid and the poroelastic medium at their common interface. Finally, feedback from the poroelastic medium to the fluid is accommodated by replacing the second integral on the right hand side of (243) by

$$\int_\Gamma \tilde{\chi}_a \, \hat{\mathbf{n}} \cdot \nabla \chi_a \, \mathrm{d}^2\mathbf{x} = \int_\Gamma \tilde{\chi}_a \, \hat{\mathbf{n}} \cdot [(1-\phi)\overline{\mathbf{u}}_s + \phi \overline{\mathbf{u}}_f] \, \mathrm{d}^2\mathbf{x} = \int_\Gamma \tilde{\chi}_a \, \hat{\mathbf{n}} \cdot (\overline{\mathbf{u}}_s + \overline{\mathbf{w}}) \, \mathrm{d}^2\mathbf{x}, \tag{246}$$

thus exchanging the normal component of displacement between the fluid and the poroelastic medium.

13.2.2 Coupled acoustic and poroelastic waves

In this section, we consider a model with an acoustic layer (inviscid fluid, $\eta_f = 0$) on top of a homogeneous poroelastic layer. The model domain is 4800 m $\times$ 4800 m. The porous medium properties are summarized in Table 3. We use a Ricker wavelet source time function (i.e. the derivative of a Gaussian) with a dominant frequency of 15 Hz. The source is located in the acoustic domain at $\mathbf{x}_s = (1600, 2900)$. We place one receiver at $\mathbf{x}_{r1} = (2000, 2934)$ in the acoustic domain and a second receiver at $\mathbf{x}_{r2} = (2000, 1867)$ in the poroelastic domain (Fig. 8(1)).

Table 3. Acoustic–poroelastic model properties.

Variable name	Symbol	Unit	Value
	Acoustic layer		
Density	ρ	$\mathrm{kg\,m^{-3}}$	1020
Bulk modulus	κ	GPa	2.295
P wave	$c_{p\mathrm{I}}$	$\mathrm{m\,s^{-1}}$	1500
S wave	c_s	$\mathrm{m\,s^{-1}}$	0
	Poroelastic layer		
Solid density	ρ_s	$\mathrm{kg\,m^{-3}}$	2500
Fluid density	ρ_f	$\mathrm{kg\,m^{-3}}$	1020
Porosity	ϕ	–	0.4
Tortuosity	c	–	2
Solid bulk modulus	κ_s	GPa	16.0554
Fluid bulk modulus	κ_f	GPa	2.295
Frame bulk modulus	κ_{fr}	GPa	10.0
Fluid viscosity	η_f	Pa s	0
Frame shear modulus	μ_{fr}	GPa	9.63342
Fast *P* wave	$c_{p\mathrm{I}}$	$\mathrm{m\,s^{-1}}$	3677
Slow *P* wave	$c_{p\mathrm{II}}$	$\mathrm{m\,s^{-1}}$	1060
S wave	c_s	$\mathrm{m\,s^{-1}}$	2378

Table 4. Poroelastic–poroelastic model properties—homogeneous case.

Variable name	Symbol	Unit	Value
	Upper layer		
Solid density	ρ_s	$\mathrm{kg\,m^{-3}}$	2200
Fluid density	ρ_f	$\mathrm{kg\,m^{-3}}$	950
Porosity	ϕ	–	0.4
Tortuosity	c	–	2
Solid bulk modulus	κ_s	GPa	6.9
Fluid bulk modulus	κ_f	GPa	2.0
Frame bulk modulus	κ_{fr}	GPa	6.7
Fluid viscosity	η_f	Pa s	0
Frame shear modulus	μ_{fr}	GPa	3.0
Fast *P* wave	$c_{p\mathrm{I}}$	$\mathrm{m\,s^{-1}}$	2693
Slow *P* wave	$c_{p\mathrm{II}}$	$\mathrm{m\,s^{-1}}$	1186
S wave	c_s	$\mathrm{m\,s^{-1}}$	1410
	Lower layer		
Solid density	ρ_s	$\mathrm{kg\,m^{-3}}$	2650
Fluid density	ρ_f	$\mathrm{kg\,m^{-3}}$	750
Porosity	ϕ	–	0.2
Tortuosity	c	–	2
Solid bulk modulus	κ_s	GPa	6.9
Fluid bulk modulus	κ_f	GPa	2.0
Frame bulk modulus	κ_{fr}	GPa	6.7
Fluid viscosity	η_f	Pa s	0
Frame shear modulus	μ_{fr}	GPa	3.0
Fast *P* wave	$c_{p\mathrm{I}}$	$\mathrm{m\,s^{-1}}$	2219
Slow *P* wave	$c_{p\mathrm{II}}$	$\mathrm{m\,s^{-1}}$	1169
S wave	c_s	$\mathrm{m\,s^{-1}}$	1325

Fig. 8(2) displays SEM synthetic seismograms at the two receivers, which are compared to the analytical solution provided by Dr Julien Diaz (University of Pau, France) (Diaz & Ezziani 2007). The RMS misfit values demonstrate that the results are in good agreement.

13.3 Heterogeneous poroelastic media

In this section we investigate wave propagation in layered porous media. First, in Section 13.3.1, we specify the boundary conditions used to deal with porosity discontinuities. Next, in Sections 13.3.2 and 13.3.3 we present two applications. Finally, in Section 13.3.4 we discuss differences between gradients and discontinuities in porosity.

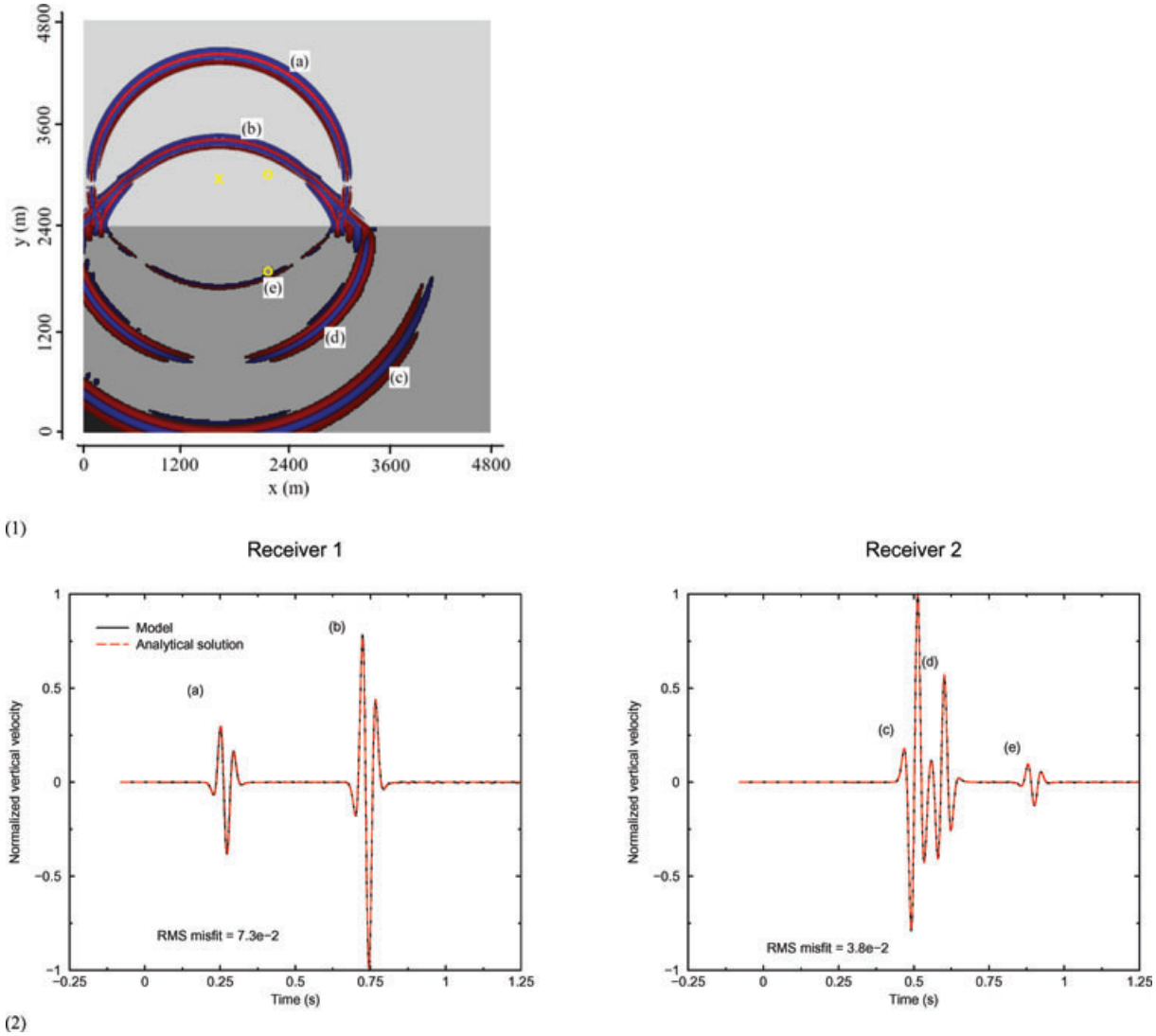

Figure 8. Acoustic–poroelastic simulation of wave propagation in a water layer over a homogeneous poroelastic half-space, as tabulated in Table 3. The model dimensions are 4800 m × 4800 m, the source (yellow cross) is located at $\mathbf{x}_s = (1600, 2900)$ and the receivers (yellow circles) at $\mathbf{x}_{r1} = (2000, 2934)$ and at $\mathbf{x}_{r2} = (2000, 1867)$. The top is a free surface and the remaining three edges are absorbing boundaries. The explosive source has a Ricker wavelet source time function with a dominant frequency of 15 Hz. (1) Snapshot of the vertical-component of displacement at $t = 1.00$ s. We can observe the direct P (a) and the reflected P (b) waves in the acoustic domain, while the transmitted fast P (c), the P-to-S converted (d), and the P-to-slow P converted (e) waves are clearly visible in the poroelastic domain. (2) Vertical-component velocity seismograms at receivers 1 and 2 (SEM: solid black line, analytical solution: dashed red line). We use domain decomposition between the fluid and the poroelastic solid as described in Section 13.2.1

13.3.1 Boundary conditions

One needs to realize that any discontinuity in porosity results in a discontinuous relative fluid displacement $\overline{\mathbf{w}} = \phi(\overline{\mathbf{u}}_f - \overline{\mathbf{u}}_s)$. In the SEM discretization, the assembly stage forces $\overline{\mathbf{w}}$ to be continuous across an element boundary. Thus, simulations involving gradients in porosity are accommodated, but discontinuities in porosity are not. In order to account for discontinuities in porosity, we use the concept of domain decomposition in a similar manner as used for coupling acoustic and elastic domains (Chaljub & Valette 2004; Komatitsch *et al.* 2005). Thus, each poroelastic domain is treated independently. Coupling is achieved by applying the principle of continuity of traction and displacement across the interface between the two poroelastic domains. Practically, if we denote the two domains by subscripts 1 and 2, the boundary conditions are

$$\overline{\mathbf{T}}^1 \cdot \hat{\mathbf{n}} = \overline{\mathbf{T}}^2 \cdot \hat{\mathbf{n}}, \quad \overline{\mathbf{T}}_f^1 \cdot \hat{\mathbf{n}} = \overline{\mathbf{T}}_f^2 \cdot \hat{\mathbf{n}}, \quad \overline{\mathbf{u}}_s^1 = \overline{\mathbf{u}}_s^2, \quad \overline{\mathbf{w}}^1 = \overline{\mathbf{w}}^2. \tag{247}$$

13.3.2 Continuous bulk and shear moduli and a jump in porosity

We consider a two-layer poroelastic model. The properties of the two layers are summarized in Table 4. Note that the bulk and shear moduli of the two layers are identical, whereas the porosities and densities are different. The dimensions of the domain are 4800 m × 4800 m. The

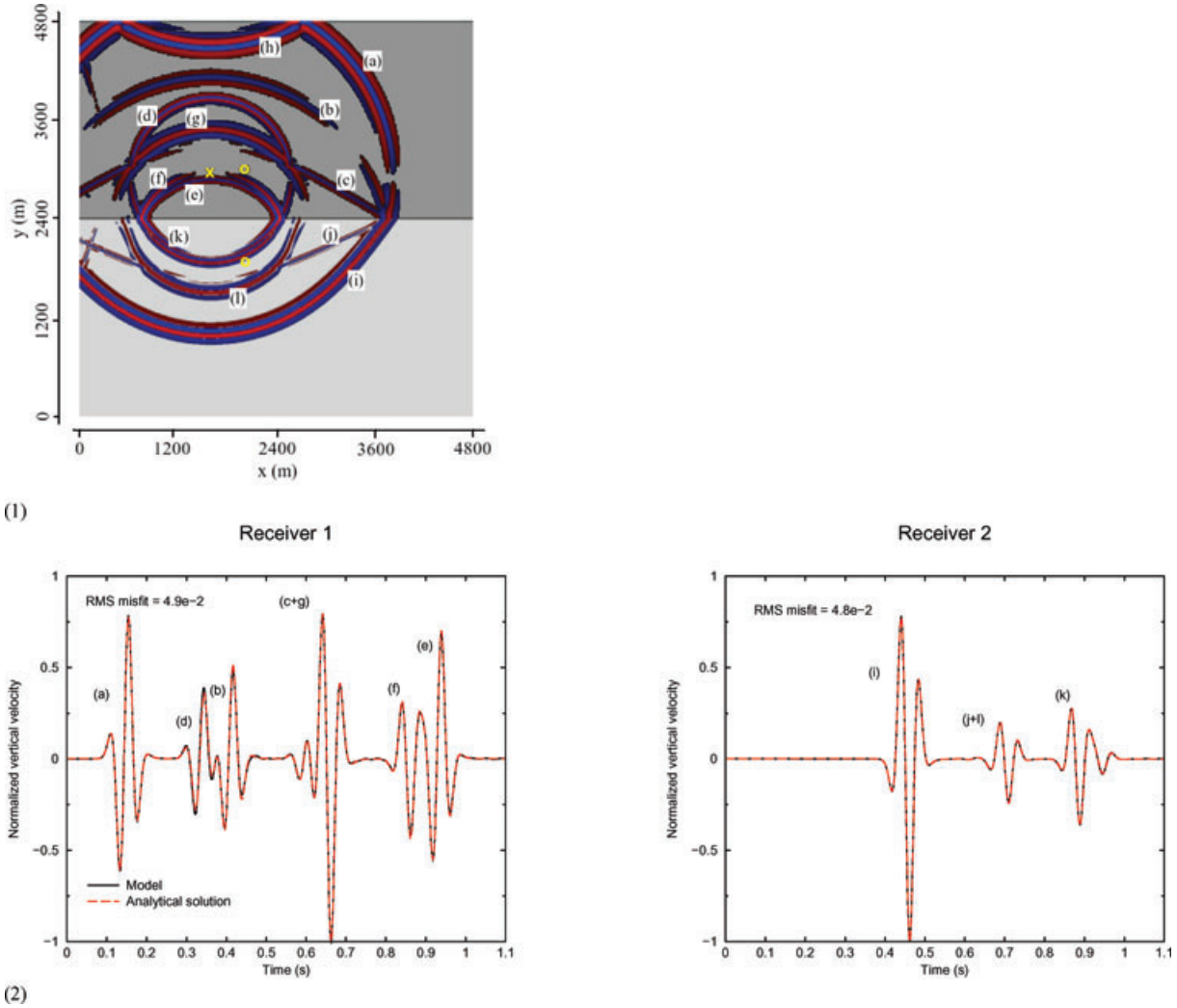

Figure 9. Simulation of wave propagation in a model consisting of two homogeneous poroelastic layers with continuous bulk and shear moduli and discontinuous porosities, as tabulated in Table 4. The model dimensions are 4800 m × 4800 m, the source (yellow cross) is located at $\mathbf{x}_s = (1600, 2900)$ and the receivers (yellow circles) at $\mathbf{x}_{r1} = (2000, 2934)$ and at $\mathbf{x}_{r2} = (2000, 1867)$. The top is a free surface and the remaining three edges are absorbing boundaries. The explosive source has a Ricker wavelet source time function with a dominant frequency of 15 Hz. (1) Snapshot of the vertical-component displacement at $t = 0.82$ s. The direct fast P (a), the reflected fast P (b), the reflected fast P-to-S and the fast P-to-slow P converted (c) waves (which overlap because they have similar wave speeds) may be observed in the upper layer, together with the direct slow P (d), the reflected slow P (e), the reflected slow P-to-S converted (f), and the reflected slow P-to-fast P converted (g) waves. We also observe the reflected fast P wave due to the free surface (h). In the lower layer, the transmitted fast P (i), fast P-to-S and fast P-to-slow P converted (j) waves (which again overlap because they have similar wave speeds) can clearly be identified, together with the transmitted slow P and slow P-to-S converted (k) and slow P-to-fast P converted (l) waves. There are some weak spurious reflections from the absorbing boundary at $x = 0$. (2) Vertical-component velocity seismograms at receivers 1 and 2 (SEM: solid black line, analytical solution: dashed red line). We use domain composition to accommodate the first-order discontinuity in porosity in the Biot $(\overline{\mathbf{u}}_s, \overline{\mathbf{w}})$ formulation based upon the approach described in Section 13.3.1

explosive source is located in the upper layer at $\mathbf{x}_s = (1600, 2900)$. We place one receiver in each domain at $\mathbf{x}_{r1} = (2000, 2934)$ and $\mathbf{x}_{r2} = (2000, 1867)$ (Fig. 9(1)). Fig. 9(2) displays SEM synthetic seismograms at the two receivers, which are compared to the analytical solution provided by Dr Julien Diaz. As demonstrated by the RMS misfit values, the results are again in good agreement.

13.3.3 Discontinuous bulk and shear moduli and a jump in porosity

Again, we consider a two-layer poroelastic model. The properties of the layers are summarized in Table 5. Note that in this case we choose distinct bulk and shear moduli for the two layers, and a discontinuous porosity. The dimensions of the domain are 4800 m × 4800 m. The explosive source is located in the upper layer at $\mathbf{x}_s = (1600, 2900)$. We place one receiver in each domain at $\mathbf{x}_{r1} = (2000, 2934)$ and $\mathbf{x}_{r2} = (2000, 1867)$ (Fig. 10(1)). Fig. 10(2) shows the SEM synthetic seismograms at the two receivers, which are in good agreement with the analytical solution provided by Dr Julien Diaz.

Table 5. Poroelastic–poroelastic model properties—heterogeneous case.

Variable name	Symbol	Unit	Value
	Upper layer		
Solid density	ρ_s	$\mathrm{kg\,m^{-3}}$	2200
Fluid density	ρ_f	$\mathrm{kg\,m^{-3}}$	950
Porosity	ϕ	–	0.4
Tortuosity	c	–	2
Solid bulk modulus	κ_s	GPa	6.9
Fluid bulk modulus	κ_f	GPa	2.0
Frame bulk modulus	κ_{fr}	GPa	6.7
Fluid viscosity	η_f	Pa s	0
Frame shear modulus	μ_{fr}	GPa	3.0
Fast P wave	$c_{p\mathrm{I}}$	$\mathrm{m\,s^{-1}}$	2693
Slow P wave	$c_{p\mathrm{II}}$	$\mathrm{m\,s^{-1}}$	1186
S wave	c_s	$\mathrm{m\,s^{-1}}$	1410
	Lower layer		
Solid density	ρ_s	$\mathrm{kg\,m^{-3}}$	2650
Fluid density	ρ_f	$\mathrm{kg\,m^{-3}}$	750
Porosity	ϕ	–	0.2
Tortuosity	c	–	2
Solid bulk modulus	κ_s	GPa	37
Fluid bulk modulus	κ_f	GPa	1.7
Frame bulk modulus	κ_{fr}	GPa	2.2
Fluid viscosity	η_f	Pa s	0
Frame shear modulus	μ_{fr}	GPa	4.4
Fast P wave	$c_{p\mathrm{I}}$	$\mathrm{m\,s^{-1}}$	2535
Slow P wave	$c_{p\mathrm{II}}$	$\mathrm{m\,s^{-1}}$	744
S wave	c_s	$\mathrm{m\,s^{-1}}$	1416

13.3.4 Gradient in porosity

In this section, we perform various simulations involving porosity gradients or discontinuities, as tabulated in Table 4, to highlight the differences between the following five models:

(i) Model A: no domain decomposition, meaning we incorrectly consider $\overline{\mathbf{w}}$ to be continuous across the porosity discontinuity (as discussed in Section 13.3.1).
(ii) Model B: a smooth porosity gradient.
(iii) Model C: an intermediate porosity gradient.
(iv) Model D: a sharp porosity gradient.
(v) Model E: domain decomposition (as discussed in Section 13.3.2, Fig. 9).

For each of these five models, the behaviour of the porosity across the interface is displayed in Fig. 11. The dimensions of the domain are 4800 m $\times$ 4800 m. The explosive source is located in the upper layer at $\mathbf{x}_s = (1600, 2900)$. We use a Ricker wavelet source time function with a dominant frequency of 15 Hz. We place one receiver in each domain at $\mathbf{x}_{r1} = (2000, 2934)$ and $\mathbf{x}_{r2} = (2000, 1867)$ (Figs 12(1)–(4)).

As mentioned at the beginning of Section 13.3.1, the SEM discretization naturally accounts for porosity gradients, but not for discontinuities in porosity. A comparison of seismograms for the various models (Fig. 12(5)) at receivers 1 and 2 shows that a gradient in porosity is not the right tactic to handle a porosity discontinuity. We note the strong sensitivity to the nature of the gradient by observing the increasing level of accuracy reached by Models B–D, as we sharpen the porosity gradient. Moreover, we have confirmation that porosity discontinuities are not naturally taken into account by our SEM discretization of $\overline{\mathbf{w}}$ by comparing Models A and E, that is, domain decomposition is required to properly model a discontinuity in porosity.

13.4 Coupling between elastic and poroelastic waves

We recall the elastic wave equation and discuss the coupling with a poroelastic domain, before presenting an application.

13.4.1 Elastic wave equation

The equation of motion for an elastic medium is

$$\rho_e \partial_t^2 \mathbf{u}_e = \boldsymbol{\nabla} \cdot \mathbf{T}_e, \tag{248}$$

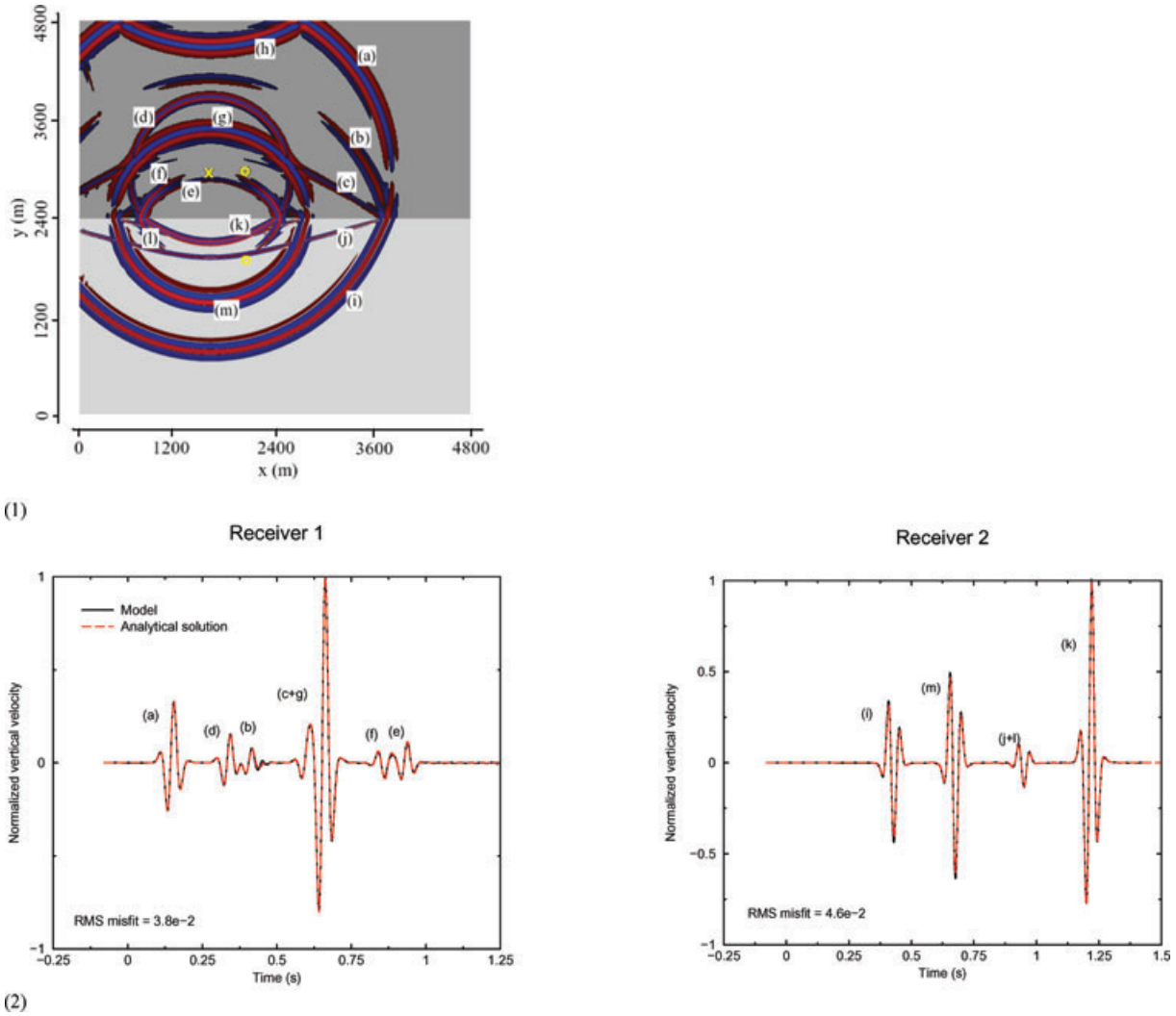

Figure 10. Simulation of wave propagation in a model consisting of two homogeneous poroelastic layers with discontinuous bulk and shear moduli and porosities, as tabulated in Table 5. The model dimensions are 4800 m × 4800 m, the source (yellow cross) is located at $\mathbf{x}_s = (1600, 2900)$ and the receivers (yellow circles) at $\mathbf{x}_{r1} = (2000, 2934)$ and at $\mathbf{x}_{r2} = (2000, 1867)$. The top is a free surface and the remaining three edges are absorbing boundaries. The explosive source has a Ricker wavelet source time function with a dominant frequency of 15 Hz. (1) Snapshot of the vertical-component displacement at $t =$ 0.82 s. The direct fast *P* (a), the reflected fast *P* (b), and the reflected fast *P*-to-*S* and fast *P*-to-slow *P* converted (c) waves (which overlap because they have similar wave speeds) may be observed in the upper layer, together with the direct slow *P* (d), the reflected slow *P* (e), the reflected slow *P*-to-*S* converted (f), and the reflected slow *P*-to-fast *P* converted (g) waves. We also observe the reflected fast *P* wave due to the free surface (h). In the lower layer, the transmitted fast *P* (i) and fast *P*-to-slow *P* converted (j) waves may be clearly identified, together with the transmitted slow *P* (k), slow *P*-to-*S* converted (l) and slow *P*-to-fast *P* converted (m) waves. Note that the transmitted fast *P*-to-*S* converted wave, which presents a low amplitude, is not visible. (2) Vertical-component velocity seismograms at receivers 1 and 2 (SEM: solid black line, analytical solution: dashed red line). We use domain composition to accommodate the first-order discontinuity in porosity in the Biot ($\overline{\mathbf{u}}_s$, $\overline{\mathbf{w}}$) formulation based upon the approach described in Section 13.3.1

with

$$\mathbf{T}_e = \mathbf{c}_e : \nabla \mathbf{u}_e, \tag{249}$$

where $\mathbf{c}_e$ is the fourth-order elastic tensor. For an isotropic material we have

$$c^e_{ijkl} = (\kappa_e - {}^2/_3\mu_e)\delta_{ij}\delta_{kl} + \mu_e(\delta_{ik}\delta_{jl} + \delta_{il}\delta_{jk}). \tag{250}$$

Here κ_e denotes the bulk modulus and μ_e the shear modulus. Dotting (248) with an arbitrary test vector $\tilde{\mathbf{u}}_e$ and integrating by parts leads to the following weak form:

$$\int_\Omega \rho_e \tilde{\mathbf{u}}_e \cdot \partial_t^2 \mathbf{u}_e \, \mathrm{d}^3\mathbf{x} = -\int_\Omega \nabla \tilde{\mathbf{u}}_e : \mathbf{T}_e \, \mathrm{d}^3\mathbf{x} + \int_\Gamma \hat{\mathbf{n}} \cdot \mathbf{T}_e \cdot \tilde{\mathbf{u}}_e \, \mathrm{d}^2\mathbf{x}. \tag{251}$$

Coupling between the elastic and the poroelastic domains is achieved by imposing the following boundary conditions:

$$\overline{\mathbf{T}} \cdot \hat{\mathbf{n}} = \mathbf{T}_e \cdot \hat{\mathbf{n}}, \quad \overline{\mathbf{T}}_f \cdot \hat{\mathbf{n}} = \mathbf{T}_e \cdot \hat{\mathbf{n}}, \quad \overline{\mathbf{u}}_s = \mathbf{u}_e, \quad \overline{\mathbf{w}} = \mathbf{0}. \tag{252}$$

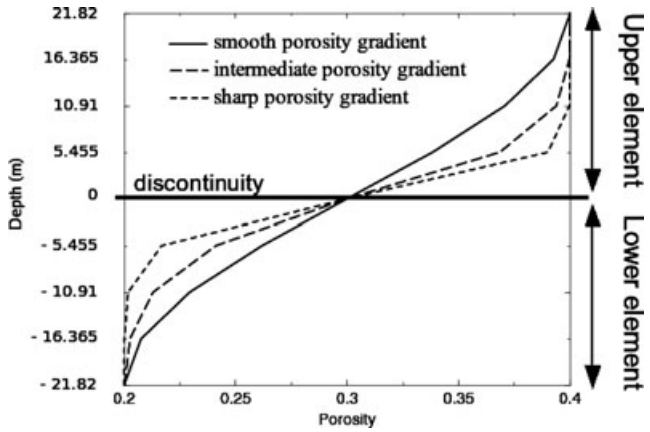

Figure 11. Various gradients in porosity used to mimic a porosity discontinuity.

13.4.2 Poroelastic–elastic coupling

We consider a poroelastic layer on top of an elastic layer; the properties of the two layers are summarized in Table 6. Note that we choose the poroelastic upper layer properties to be identical to one of the previous models (Section 13.3.2) and that we choose the elastic lower layer properties (bulk and shear moduli) such that the phase speeds are identical to those in the poroelastic lower layer of the same previous model (compare Tables 4 and 6). In Section 10, we summarized expressions for the fast and slow compressional wave speeds as well as the shear wave speed in homogeneous porous media. We recall that the compressional and shear wave speeds in a purely elastic medium, c_p and c_s, respectively, are determined by

$$c_p = \sqrt{\frac{\kappa_e + \frac{4}{3}\mu_e}{\rho_e}}, \quad c_s = \sqrt{\frac{\mu_e}{\rho_e}}. \tag{253}$$

The phase speeds displayed in Table 6 have been calculated based upon these formulae and may be compared to the values summarized in Table 4. The dimensions of the domain are 4800 m $\times$ 4800 m. The explosive source is located in the upper (poroelastic) layer at $\mathbf{x}_s = (1600, 2900)$. We place one receiver in each domain at $\mathbf{x}_{r1} = (2000, 2934)$ and $\mathbf{x}_{r2} = (2000, 1867)$ (Fig. 13(1)). Fig. 13(2) displays synthetic seismograms at the two receivers, together with the seismograms obtained for the previous model with a discontinuity in porosity (Section 13.3.3). The results at receiver 1, located in the poroelastic upper layer, show differences in the amplitude of the various phases between the two models, except for the direct fast and slow P waves. The results at receiver 2, located in the elastic lower layer, exhibit equivalent arrival times but differences in amplitudes. The amplitude differences between the two simulations clearly illustrate the implications of the distinct reflection and transmission coefficients at poroelastic–elastic and poroelastic–poroelastic interfaces.

14 SAMPLE APPLICATIONS

In this section, we present examples of poroelastic wave propagation in more complex media.

14.1 Compacted sedimentary layer

We consider a model with an acoustic (water) layer on top of a compacted sedimentary layer (with an exponential decrease in porosity with depth and constant bulk and shear moduli, see Fig. 14(1)). This experiment has ingredients relevant to problems encountered in the petroleum industry. We use a Ricker wavelet source time function with a dominant frequency of 15 Hz. We compare the results obtained based upon this model with those obtained for the model used as a benchmark in Section 13.2.2 to highlight the effects of a porosity gradient (Fig. 14(2)). We observe exactly the same arrival times and amplitudes at receiver 1 in the acoustic domain, while we observe clear differences at receiver 2 in the poroelastic domain. These differences highlight the effects of a porosity gradient on phase speeds (see Section 10). For a porosity of 0.4 we have $c_{p\mathrm{I}} = 3677\ \mathrm{m\,s^{-1}}$, $c_{p\mathrm{II}} = 1060\ \mathrm{m\,s^{-1}}$ and $c_s = 2378\ \mathrm{m\,s^{-1}}$, whereas for a porosity of 0.1 we have $c_{p\mathrm{I}} = 3279\ \mathrm{m\,s^{-1}}$, $c_{p\mathrm{II}} = 862\ \mathrm{m\,s^{-1}}$ and $c_s = 2046\ \mathrm{m\,s^{-1}}$, and in the purely elastic layer $c_p = 3399\ \mathrm{m\,s^{-1}}$ and $c_s = 1963\ \mathrm{m\,s^{-1}}$. Note that because of the smoothly vanishing porosity towards the elastic interface, the poroelastic–elastic boundary does not act as a strong reflector.

This application clearly illustrates that our spectral-element implementation of the Biot equations remains stable and valid when the porosity vanishes. In such regions, the volumetric fluid flow per unit surface area, $\overline{\mathbf{w}}$, vanishes, and the Biot equations reduce to the elastic wave equation.

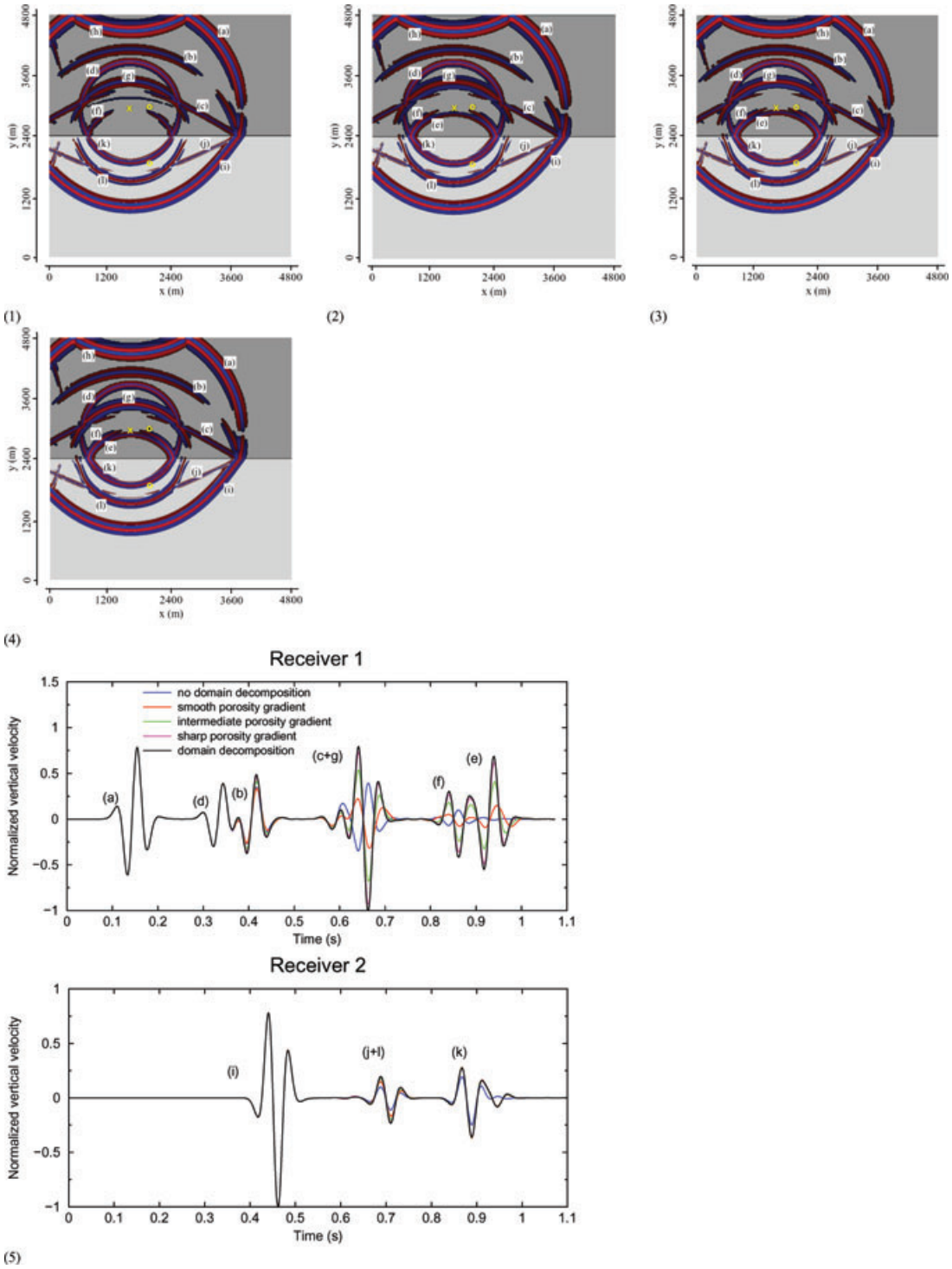

Figure 12. Simulations of wave propagation in a model consisting of two homogeneous poroelastic layers with continuous bulk and shear moduli and discontinuous porosities, as tabulated in Table 4. The dimensions of the domain are 4800 m × 4800 m. The explosive source is located in the upper layer at $\mathbf{x}_s = (1600, 2900)$. We use a Ricker source time function with a dominant frequency of 15 Hz. We place one receiver in each domain at $\mathbf{x}_{r1} = (2000, 2934)$ and $\mathbf{x}_{r2} = (2000, 1867)$. Various types of models have been designed to address a discontinuity in porosity, as shown in Fig. 11. Snapshots of the vertical-component displacement at $t = 0.82$ s for (1) Model A: no domain decomposition, (2) Model B: a smooth porosity gradient, (3) Model C: an intermediate porosity gradient, (4) Model D: a sharp porosity gradient, and Model E: domain decomposition (see Fig. 9). The direct fast *P* (a), the reflected fast *P* (b), the reflected fast *P*-to-*S* and the fast *P*-to-slow *P* converted (c) waves (which overlap because they have similar wave speeds) may be observed in the upper layer, together with the direct slow *P* (d), the reflected slow *P* (e), the reflected slow *P*-to-*S* converted (f), and the reflected slow *P*-to-fast *P* converted (g) waves. We also observe the reflected fast *P* wave due to the free surface (h). In the lower layer, the transmitted fast *P* (i), fast *P*-to-*S* and fast *P*-to-slow *P* converted (j) waves (which again overlap because they have similar wave speeds) can clearly be identified, together with the transmitted slow *P* and slow *P*-to-*S* converted (k) and slow *P*-to-fast *P* converted (l) waves. (5) Vertical-component velocity seismograms at receivers 1 and 2.

Table 6. Poroelastic–elastic model properties.

Variable name	Symbol	Unit	Value
	Poroelastic layer		
Solid density	ρ_s	$\mathrm{kg\,m^{-3}}$	2200
Fluid density	ρ_f	$\mathrm{kg\,m^{-3}}$	950
Porosity	ϕ	–	0.4
Tortuosity	c	–	2
Solid bulk modulus	κ_s	GPa	6.9
Fluid bulk modulus	κ_f	GPa	2.0
Frame bulk modulus	κ_{fr}	GPa	6.7
Fluid viscosity	η_f	Pa s	0
Frame shear modulus	μ_{fr}	GPa	3.0
Fast P wave	$c_{p\mathrm{I}}$	$\mathrm{m\,s^{-1}}$	2693
Slow P wave	$c_{p\mathrm{II}}$	$\mathrm{m\,s^{-1}}$	1186
S wave	c_s	$\mathrm{m\,s^{-1}}$	1410
	Elastic layer		
Density	ρ_e	$\mathrm{kg\,m^{-3}}$	2650
Bulk modulus	κ_e	GPa	6.845
Shear modulus	μ_e	GPa	4.652
P wave	c_p	$\mathrm{m\,s^{-1}}$	2219
S wave	c_s	$\mathrm{m\,s^{-1}}$	1325

Table 7. Acoustic–poroelastic model properties: buried object detection.

Variable name	Symbol	Unit	Value
	Acoustic layer		
Density	ρ	$\mathrm{kg\,m^{-3}}$	1020
Bulk modulus	κ	GPa	2.295
P wave	$c_{p\mathrm{I}}$	$\mathrm{m\,s^{-1}}$	1500
S wave	c_s	$\mathrm{m\,s^{-1}}$	0
	Poroelastic layer		
Solid density	ρ_s	$\mathrm{kg\,m^{-3}}$	2650
Fluid density	ρ_f	$\mathrm{kg\,m^{-3}}$	750
Porosity	ϕ	–	0.4 (0.14)
Tortuosity	c	–	2
Solid bulk modulus	κ_s	GPa	37.0
Fluid bulk modulus	κ_f	GPa	1.7
Frame bulk modulus	κ_{fr}	GPa	2.2
Fluid viscosity	η_f	Pa s	0
Frame shear modulus	μ_{fr}	GPa	6.0
Fast P wave	$c_{p\mathrm{I}}$	$\mathrm{m\,s^{-1}}$	2709 (2811)
Slow P wave	$c_{p\mathrm{II}}$	$\mathrm{m\,s^{-1}}$	923 (705)
S wave	c_s	$\mathrm{m\,s^{-1}}$	1857 (1604)
	Elastic buried metal object		
Density	ρ_e	$\mathrm{kg\,m^{-3}}$	4000
Bulk modulus	κ_e	GPa	63.6
Shear modulus	μ_e	GPa	8
P wave	c_p	$\mathrm{m\,s^{-1}}$	4309
S wave	c_s	$\mathrm{m\,s^{-1}}$	1414

14.2 Buried object detection

Considerable attention has been given by military and humanitarian organizations to improving the detection and characterization of a large variety of buried landmines and unexploded ordnance (UXO) worldwide. For example, acoustic methods have been employed for such detection purposes (e.g. Scott *et al.* 2001; Zeng & Liu 2001a; Xiang & Sabatier 2003).

We designed two models to evaluate the signature of a purely elastic buried object in three types of environments:

(i) Model 1: acoustic layer on top of a poroelastic medium with a porosity gradient and no viscous damping.

(ii) Model 2: acoustic layer on top of a poroelastic medium with a porosity gradient and viscous damping (with $\eta_f = 10^{-3}$ Pas, an isotropic permeability $k = 10^{-12}$ m^2, and $f_c = 42$ kHz).

(iii) Model 3: acoustic layer on top of an elastic medium.

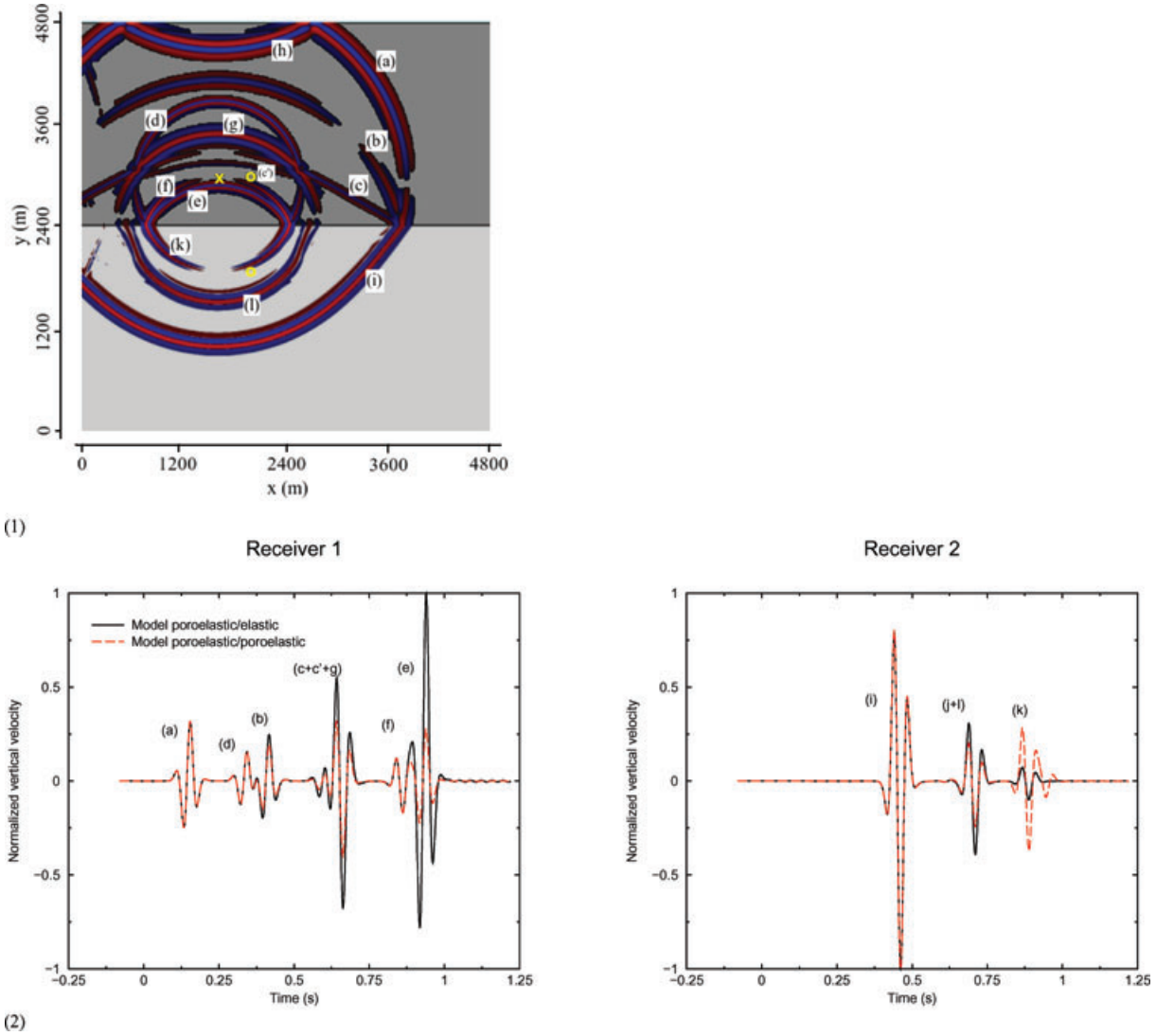

Figure 13. Simulation of wave propagation in a model consisting of a homogeneous elastic layer beneath a homogeneous poroelastic layer, as tabulated in Table 6. The model dimensions are 4800 m × 4800 m, the source (yellow cross) is located at $\mathbf{x}_s = (1600, 2900)$ and the receivers (yellow circles) at $\mathbf{x}_{r1} = (2000, 2934)$ and at $\mathbf{x}_{r2} = (2000, 1867)$. The top is a free surface and the remaining three edges are absorbing boundaries. The explosive source has a Ricker wavelet source time function with a dominant frequency of 15 Hz. (1) Snapshot of the vertical-component displacement at $t = 0.82$ s. The direct fast *P* (a), the reflected fast *P* (b), and the reflected fast *P*-to-*S* (c) and fast *P*-to-slow *P* converted (c') waves may be observed in the poroelastic domain, together with the direct slow *P* (d), the reflected slow *P* (e), the reflected slow *P*-to-*S* converted (f), and the reflected slow *P*-to-fast *P* (g) converted waves. We also observe the reflected fast *P* wave due to the free surface (h). In the elastic domain, the transmitted fast *P* (i) wave can clearly be identified, together with the transmitted slow *P* and slow *P*-to-*S* (k) and slow *P*-to-fast *P* converted (l) waves. Note that the transmitted fast *P*-to-*S* converted wave has a low amplitude and is not visible. (2) Vertical-component velocity seismograms at receivers 1 and 2 (poroelastic–elastic interface: solid black line, poroelastic–poroelastic discontinuity as in Section 13.3.3: dashed red line). We use domain composition as described in Section 13.4.1.

We use a Ricker wavelet source time function with a dominant frequency of 5 kHz, that is, three orders of magnitude higher than in previous experiments. The source is located in the acoustic domain, and we place 20 receivers close to the bottom of this domain [Figs 15(1)–(3)]. The model dimensions are 10 × 8 m, that is, much smaller than in the previous experiments. The model geometry mimics a typical under water landmine/UXO detection experiment (Tables 7 and 8).

The differences between synthetic seismograms for Models 1, 2 and 3 with and without the buried metal object [Fig. 15(4)] illustrate the corresponding seismic signatures. The differential seismograms for Models 1 and 2 illustrate the impact of viscous damping on the slow compressional waves, which are clearly suppressed in Model 2. The signature of the object in differential seismograms for elastic Model 3 is notably different from that in the poroelastic models. Clearly, the nature of the environment in which the object is buried has an influence on the object's signature.

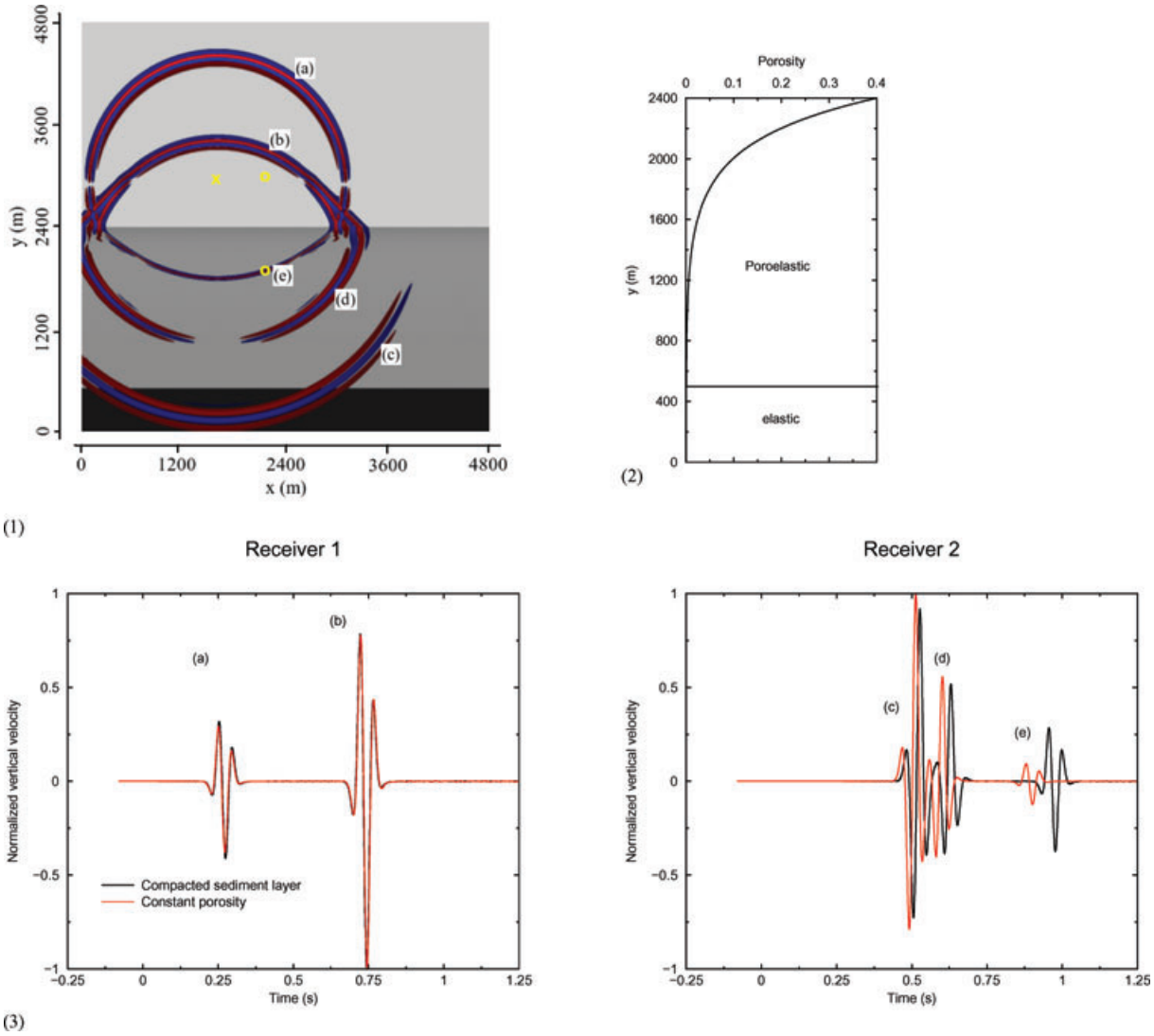

Figure 14. Simulation of wave propagation in a water layer over a compacted sedimentary layer, as tabulated in Table 3 but with variable porosity. The model dimensions are 4800 m × 4800 m, the source (yellow cross) is located at $\mathbf{x}_s = (1600, 2900)$ and the receivers (yellow circles) at $\mathbf{x}_{r1} = (2000, 2934)$ and at $\mathbf{x}_{r2} = (2000, 1867)$. The top is a free surface and the remaining three edges are absorbing boundaries. The explosive source has a Ricker wavelet source time function with a dominant frequency of 15 Hz. (1) Snapshot of the vertical-component displacement at $t = 1.00$ s. We can observe the direct P (a) and the reflected P (b) waves in the acoustic domain, the transmitted fast P (c), the fast P-to-S (d), and the fast P-to-slow P (e) waves in the poroelastic domain. (2) Porosity profile in the poroelastic layer. (3) Vertical-component velocity seismograms at receivers 1 and 2 (compacted sediment layer: solid black line, constant porosity of 0.4: solid red line). We use domain composition as described in Section 13.4.1.

15 CONCLUSIONS

This paper presents a numerical implementation of poroelastic wave propagation using a SEM. The first part is dedicated to a straightforward derivation of the main equations that govern wave propagation in a general poroelastic medium. This set of equations is derived using an averaging principle, which accommodates the transition from the microscopic to the macroscopic scale. We pay particular attention to the effects of gradients in porosity, and we show that the original Biot formulation naturally takes such gradients into account. The popular equation for the 'change in fluid content' acquires two extra terms related to porosity gradients.

The second part of the paper deals with the numerical aspects of wave propagation in porous media. Using a spectral-element approach one naturally obtains a diagonal mass matrix, which—as in the elastic and acoustic cases—leads to explicit time schemes that lend themselves very well to applications on large parallel computers. Coupling between acoustic, elastic and poroelastic waves at first-order interfaces may be accommodated based upon domain decomposition. In particular, problems involving a sharp discontinuity in porosity may be efficiently handled in this fashion. Our spectral-element implementation compares favourably to analytical reference solutions for problems involving acoustic–poroelastic and poroelastic–poroelastic coupling at first-order discontinuities. Gradual transitions from porous to elastic media are stably and accurately accommodated by the method.

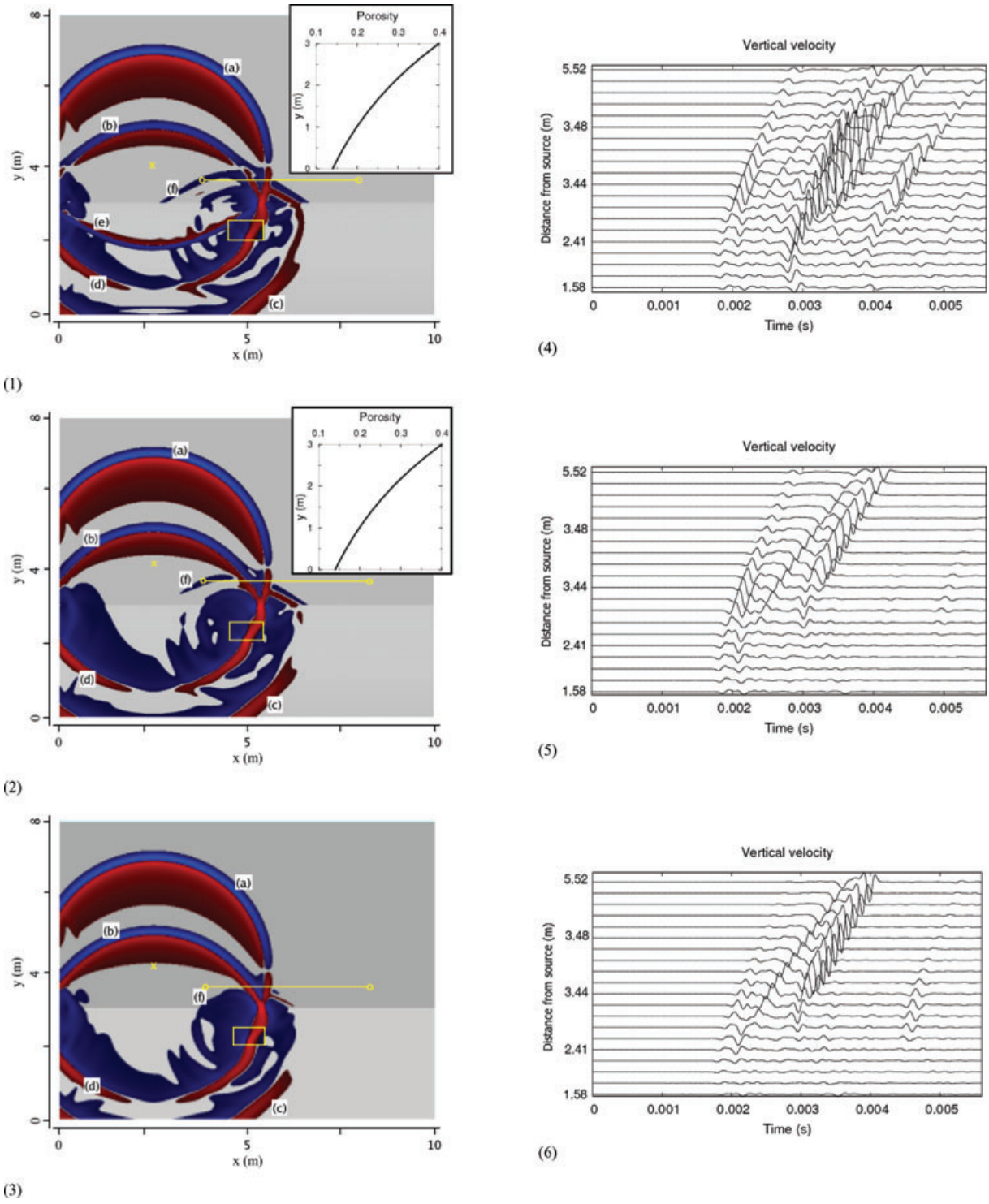

Figure 15. Simulation of wave propagation in a model consisting of a water layer over a poroelastic layer (1 and 2) or an elastic layer (3) with a buried metal object (yellow rectangle). The properties of the acoustic and poroelastic layers are summarized in Table 7, and those of the acoustic and elastic layers in Table 8, together with the elastic metal object properties. The model dimensions are 10 m × 8 m, the source (yellow cross) is located at $\mathbf{x}_s = (2.5, 4.0)$ and 20 receivers (yellow circles) are evenly located between $\mathbf{x}_{r1} = (4.0, 3.5)$ and at $\mathbf{x}_{r20} = (8.0, 3.5)$. All the edges are absorbing boundaries. The explosive source has a Ricker wavelet source time function with a dominant frequency of 5 kHz. Snapshot of the vertical-component displacement at $t = 1.76$ ms for (1) Model 1: porosity gradient and no viscous damping, (2) Model 2: porosity gradient and viscous damping and (3) Model 3: elastic. We can observe the direct P (a) and the reflected P (b) waves in the acoustic domain, the transmitted fast P (c), the P-to-S converted (d), and the fast P-to-slow P converted (e) waves in the poroelastic domain, plus waves reflected by the elastic object (f). (4) Difference between vertical-component velocity seismograms at receivers 1-20 for Model 1 with and without the buried metal object. These differential seismograms highlight the signature of the buried target. (5) Difference between vertical-component velocity seismograms at receivers 1-20 for Model 2 with and without the buried metal object. (6) Difference between vertical-component velocity seismograms at receivers 1-20 for elastic Model 3 with and without the buried metal object. We use domain composition as described in Section 13.4.1.

Table 8. Acoustic–elastic model properties: buried object detection.

Variable name	Symbol	Unit	Value
	Acoustic layer		
Density	ρ	$\mathrm{kg\,m^{-3}}$	1020
Bulk modulus	κ	GPa	2.295
P wave	$c_{p\mathrm{I}}$	$\mathrm{m\,s^{-1}}$	1500
S wave	c_s	$\mathrm{m\,s^{-1}}$	0
	Elastic layer		
Density	ρ_e	$\mathrm{kg\,m^{-3}}$	2650
Bulk modulus	κ_e	GPa	7.26
Shear modulus	μ_e	GPa	9.14
P wave	$c_{p\mathrm{I}}$	$\mathrm{m\,s^{-1}}$	2709
S wave	c_s	$\mathrm{m\,s^{-1}}$	1857
	Elastic buried metal object		
Density	ρ_e	$\mathrm{kg\,m^{-3}}$	4000
Bulk modulus	κ_e	GPa	63.6
Shear modulus	μ_e	GPa	8
P wave	c_p	$\mathrm{m\,s^{-1}}$	4309
S wave	c_s	$\mathrm{m\,s^{-1}}$	1414

Future applications of the method will involve 3-D simulations of poroelastic wave propagation in complex geometrical domains. These simulations will be of interest in the context of oil reservoir monitoring, and also for the seismic detection of landmines and unexploded ordnance buried in compacted sediments.

ACKNOWLEDGMENTS

This research was supported in part by a grant from the Strategic Environmental Research Development Program (SERDP) under contract number W912HQ-06-C-0006. We are grateful to Julien Diaz, who helped us carry out most of the 2-D benchmarks, and to Dimitri Komatitsch for providing the randomly perturbed mesh. The program used to evaluate the analytical solutions for the two layered models may be found at http://www.spice-rtn.org/library/software/Garcimore2D/. We thank Dimitri Komatitsch, Abdelaâziz Ezziani, Julien Diaz, Roland Martin from the University of Pau, France and Josep de la Puente from the University of Munich, Germany, for valuable discussions and advice. Finally, we also wish to acknowledge the Editor Johan Robertsson and two anonymous reviewers for pertinent comments which helped to improve the manuscript. This is contribution No. 8999 of the Division of Geological & Planetary Sciences (GPS), California Institute of Technology.

REFERENCES

Aki, K. & Richards, P.G., 1980. *Quantitative Seismology, Theory and Methods,* W.H. Freeman, San Francisco.

Arntsen, B. & Carcione, J.M., 2001. Numerical simulation of the Biot slow wave in water-saturated Nivelsteiner sandstone, *Geophysics,* **66,** 890–896.

Auriault, J.-L., Borne, L. & Chambon, R., 1985. Dynamics of porous saturated media, checking of the generalized law of Darcy, *J. acoust. Soc. Am.,* **77,** 1641–1650.

Bear, J., 1972. *Dynamics of Fluids in Porous Media,* American Elsevier Publishing Company Inc., New York.

Berenger, J.P., 1994. A perfectly matched layer for absorption of electromagnetic waves, *J. Comput. Phys.,* **114,** 185–200.

Biot, M.A., 1941. General theory of three-dimensional consolidation, *J. appl. Phys.,* **12,** 155–164.

Biot, M.A., 1956a, Theory of propagation of elastic waves in a fluid-saturated porous solid. I Low-frequency range, *J. acoust. Soc. Am.,* **28,** 168–178.

Biot, M.A., 1956b, Theory of propagation of elastic waves in a fluid-saturated porous solid. II Higher frequency range, *J. acoust. Soc. Am.,* **28,** 179–191.

Biot, M.A., 1962a, Mechanics of deformation and acoustic propagation in porous media, *J. appl. Phys.,* **33,** 1482–1498.

Biot, M.A., 1962b, Generalized theory of acoustic propagation in porous dissipative media, *J. acoust. Soc. Am.,* **34,** 1254–1264.

Carcione, J.M., 1993. A 3-D time-domain wave equation for viscoacoustic saturated porous media, *Eur. J. Mech., A/Solids,* **12,** 53–71.

Carcione, J.M., 2007. *Wave Fields in Real Media: Wave Propagation in Anisotropic, anelastic, Porous and Electromagnetic Media, Handbook of Geophysical Exploration,* Elsevier, Amsterdam.

Carcione, J.M. & Quiroga-Goode, G., 1996. Full frequency-range transient solution for compressional waves in a fluid-saturated viscoacoustic porous medium, *Geophys. Prospect.,* **44,** 99–129.

Carcione, J.M., Kosloff, D. & Kosloff, R., 1988a, Wave propagation simulation in an elastic anisotropic (transversely isotropic) solid, *Q. J. Mech. Appl. Math.,* **41**(3), 319–345.

Carcione, J.M., Kosloff, D. & Kosloff, R., 1988b, Wave propagation simulation in a linear viscoelastic medium, *Geophys. J. Int.,* **95,** 597–611.

Chaljub, E. & Valette, B., 2004. Spectral element modelling of three-dimensional wave propagation in a self-gravitating Earth with an arbitrarily stratified outer core, *Geophys. J. Int.,* **158,** 131–141.

Chaljub, E., Komatitsch, D., Vilotte, J.-P., Capdeville, Y., Valette, B. & Festa, G., 2007. Spectral element analysis in seismology, in *Advances in Wave Propagation in Heterogeneous Media,* Vol. 48, pp. 365–419, eds Wu, R.-S. & Maupin, V., Advances in Geophysics, Elsevier/Academic Press, London.

Chandler, R.N., 1981. Transient streaming potential measurements on fluid-saturated porous structures: an experimental verification of Biot's slow wave in the quasi-static limit, *J. acoust. Soc. Am.,* **70,** 116–121.

Chandler, R.N. & Johnson, D.L., 1981. The equivalence of quasistatic flow in fluid-saturated porous media and Biot's slow wave in the limit of zero frequency, *J. appl. Phys.,* **52,** 3391–3395.

Clayton, R. & Engquist, B., 1977. Absorbing boundary conditions for acoustic and elastic wave equations, *Bull. seism. Soc. Am.,* **67,** 1529–1540.

Dahlen, F.A., 1990. Critical taper model of fold-and-thrust belts and accretionary wedges, *Ann. Rev. Earth. Planet. Sci.,* **18,** 55–99.

Dahlen, F.A. & Tromp, J., 1998. *Theoretical Global Seismology,* Princeton University Press, Princeton.

Dai, N., Vafidis, A. & Kanasewich, E.R., 1995. Wave propagation in heterogeneous, porous media: a velocity-stress, finite-difference method, *Geophysics,* **60,** 327–340.

De Basabe, J.D. & Sen, M.K., 2007. Grid dispersion and stability criteria of some common finite-element methods for acoustic and elastic wave equations, *Geophysics,* **72,** 81–95.

de la Puente, J., 2008. Seismic wave simulation for complex rheologies on unstructured meshes, *PhD thesis*, University of Munich, Munich, Germany.

de la Puente, J., Dumbser, M., Käser, M. & Igel, H., 2007. Discontinuous galerkin methods for wave propagation in poroelastic media, *Geophysics,* in press.

Diaz, J. & Ezziani, A., 2007. Analytical solution for waves propagation in heterogeneous porous media, in preparation.

Engquist, B. & Majda, A., 1977. Absorbing boundary conditions for the numerical simulation of waves, *Math. Comp.,* **31,** 629–651.

Frenkel, Y., 1944. On the theory of seismic and seismoelectric phenomena in moist soil, *J. Phys.,* **8,** 230–241.

Geertsma, J. & Smit, D.C., 1961. Some aspects of elastic wave propagation in fluid-saturated porous solids, *Geophysics,* **26,** 169–181.

Hughes, T.J.R., 1987. *The Finite-Element Method, Linear Static and Dynamic Finite Element Analysis,* Prentice-Hall International, Englewood Cliffs, NJ.

Kelder, O. & Smeulders, D.M.J., 1997. Observation of the Biot slow wave in water-saturated Niverlsteiner sandstone, *Geophysics,* **62,** 1794–1796.

Komatitsch, D., 1997. Méthodes spectrales et éléments spectraux pour l'équation de l'élastodynamique 2D et 3D en milieu hétérogène (Spectral and spectral-element methods for the 2D and 3D elastodynamics equations in heterogeneous media), *PhD thesis*, Institut de Physique du Globe, Paris, France.

Komatitsch, D. & Tromp, J., 1999. Introduction to the spectral element method for three-dimensional seismic wave propagation, *Geophys. J. Int.,* **139,** 806–822.

Komatitsch, D. & Tromp, J., 2002. Spectral-element simulations of global seismic wave propagation – I. Validation, *Geophys. J. Int.,* **149,** 390–412.

Komatitsch, D. & Vilotte, J.P., 1998. The spectral-element method: an efficient tool to simulate the seismic response of 2D and 3D geological structures, *Bull. seism. Soc. Am.,* **88**(2), 368–392.

Komatitsch, D., Tsuboi, S. & Tromp, J., 2005. The Spectral-Element in Seismology, in *AGU Monograph,* pp. 205–228, eds Levander, A. & Nolet, G., American Geophysical Union, Washington, DC.

Leclaire, P., Cohen-Ténoudji, F. & Aguirre-Puente, J., 1994. Extension of biot's theory of wave propagation to frozen porous media, *J. acoust. Soc. Am.,* **96,** 3753–3768.

Liu, H.P., Anderson, D.L. & Kanamori, H., 1976. Velocity dispersion due to anelasticity: implications for seismology and mantle composition, *Geophys. J. R. astr. Soc.,* **47,** 41–58.

Martin, R., Komatitsch, D. & Ezziani, A., 2007. An unsplit convolutional Perfectly Matched Layer improved at grazing incidence for the seismic wave equation. Part II: poroelastic media, *Geophysics,* **73,** T51–T61, doi: 10.1190/1.2939484.

Mochizuki, S., 1982. Attenuation in partially saturated rocks, *J. geophys. Res.,* **87,** 8598–8604.

Molotkov, L.A., 2002. On the coefficients of pore tortuosity in the effective Biot model, *J. Math. Sci.,* **108,** 752–757.

Plona, T.J., 1980. Observation of a second bulk compressional wave in a porous medium at ultrasonic frequencies, *Appl. Phys. Lett.,* **36,** 259–261.

Pride, S.R., 2003. The electroseismic wave theory of Frenkel, *Lawrence Berkeley National Laboratory,* Paper LBNL-54075, http://repositories.cdlib.org/lbnl/LBNL–54075.

Pride, S.R. & Berryman, J.G., 1998. Connecting theory to experiment in poroelasticity, *J. Mech. Phys. Solids,* **46,** 719–747.

Pride, S.R., Gangi, A.F. & Morgan, F.D., 1992. Deriving the equations of motion for porous isotropic media, *J. acoust. Soc. Am.,* **92,** 3278–3290.

Robertsson, J.O.A., Blanch, J.O. & Symes, W.W., 1994. Viscoelastic finite-difference modeling, *Geophysics,* **59,** 1444–1456.

Sahay, P.N., Spanos, T.J.T. & de la Cruz, V., 2001. Seismic wave propagation in inhomogeneous and anisotropic porous media, *Geophys. J. Int.,* **145,** 209–222.

Scott, W.R., Martin, J. & Larson, G.D., 2001. Experimental model for a seismic landmine detection system, *IEEE,* **39,** 1155–1164.

Smeulders, D.M.J., 2005. Experimental evidence for slow compressional waves, *J. Eng. Mech.,* **131,** 908–917.

Stoll, R.D., 1977. Acoustic waves in ocean sediments, *Geophysics,* **42,** 715–725.

Stoll, R.D. & Bryan, G.M., 1970. Wave attenuation in saturated sediments, *J. acoust. Soc. Am.,* **47,** 1440–1447.

Terzaghi, K., 1923. Die Berechnung der Durchlässigkeitsziffer des Tones aus dem Verlauf der hydrodynamischen Spannungserscheinungen, *Sitzungsberichte der Akademie der Wissenschaften in Wien, Mathematisch-Naturwissenschaftliche Klasse, Abteilung IIa,* **132,** 125–138.

Terzaghi, K., 1943. *Theoretical Soil Mechanics,* John Wiley and Sons, New York.

Van der Grinten, J.G., Van Dongen, M.E.H. & Van der Kogel, H., 1985. A shock tube technique for studying pore pressure propagation in a dry and water-saturated porous medium, *J. Appl. Phys.,* **58,** 2937–2942.

Whitaker, S., 1999. *The Method of Volume Averaging,* Kluwer, Dordrecht.

Xiang, N. & Sabatier, J.M., 2003. An experimental study on antipersonnel landmine detection using acoustic-to-seismic coupling, *J. acoust. Soc. Am.,* **113,** 1333–1341.

Zeng, Y.Q. & Liu, Q.H., 2001a. Acoustic detection of buried object in 3-D fluid saturated porous media: numerical modeling, *IEEE Trans. Geosci. Remote Sens.,* **39,** 1165–1173.

Zeng, Y.Q. & Liu, Q.H., 2001b. A staggered-grid finite-difference method with perfectly matched layers for poroelastic wave equations, *J. acoust. Soc. Am.,* **109,** 2571–2580.

Zeng, Y.Q., He, J.Q. & Liu, Q.H., 2001. The application of the perfectly matched layer in numerical modeling of wave propagation in poroelastic media, *Geophysics,* **66,** 1258–1266.

APPENDIX A: ALTERNATIVE DERIVATION OF THE MACROSCOPIC INTERFACIAL STRAIN

In this appendix, we seek to determine the interfacial strain using the principle of virtual work. To that end, we use the definition of the potential energy per unit volume P of the poroelastic medium (98) in terms of $\overline{\mathbf{u}}_s$ and $\overline{\mathbf{u}}_f$:

$$2P = (1-\phi)\overline{\mathbf{T}}_s : \nabla\overline{\mathbf{u}}_s + \phi\overline{\mathbf{T}}_f : \nabla\overline{\mathbf{u}}_f + \overline{\mathbf{T}}_f : \nabla\phi(\overline{\mathbf{u}}_f - \overline{\mathbf{u}}_s). \tag{A1}$$

This quadratic form can also be written as

$$P = \frac{\partial P}{\partial \nabla\overline{\mathbf{u}}_s} : \nabla\overline{\mathbf{u}}_s + \frac{\partial P}{\partial \nabla\overline{\mathbf{u}}_f} : \nabla\overline{\mathbf{u}}_f + \frac{\partial P}{\partial \overline{\mathbf{u}}_s} \cdot \overline{\mathbf{u}}_s + \frac{\partial P}{\partial \overline{\mathbf{u}}_f} \cdot \overline{\mathbf{u}}_f. \tag{A2}$$

Upon comparing (A1) and (A2) we deduce that

$$\frac{\partial P}{\partial \nabla \overline{\mathbf{u}}_s} = \frac{1}{2}(1-\phi)\overline{\mathbf{T}}_s\,, \tag{A3}$$

$$\frac{\partial P}{\partial \nabla \overline{\mathbf{u}}_f} = \frac{1}{2}\phi\overline{\mathbf{T}}_f\,, \tag{A4}$$

$$\frac{\partial P}{\partial \overline{\mathbf{u}}_s} = -\frac{1}{2}\overline{\mathbf{T}}_f \cdot \nabla\phi\,, \tag{A5}$$

$$\frac{\partial P}{\partial \overline{\mathbf{u}}_f} = \frac{1}{2}\overline{\mathbf{T}}_f \cdot \nabla\phi\,. \tag{A6}$$

Expecting the interfacial strain $\mathbf{E}$ to be a function of $\overline{\mathbf{u}}_s$, $\overline{\mathbf{u}}_f$, $\nabla\overline{\mathbf{u}}_s$ and $\nabla\overline{\mathbf{u}}_f$, we can write it in the following general form

$$\mathbf{E} = \boldsymbol{\alpha}_1 : \nabla\overline{\mathbf{u}}_s + \boldsymbol{\alpha}_2 : \overline{\mathbf{u}}_s\nabla\phi + \boldsymbol{\alpha}_3 : \nabla\overline{\mathbf{u}}_f + \boldsymbol{\alpha}_4 : \overline{\mathbf{u}}_f\nabla\phi, \tag{A7}$$

where $\boldsymbol{\alpha}_1$, $\boldsymbol{\alpha}_2$, $\boldsymbol{\alpha}_3$ and $\boldsymbol{\alpha}_4$ remain to be determined. We recall the constitutive relationships (48) and (51):

$$(1-\phi)\overline{\mathbf{T}}_s = \mathbf{c}_s : \nabla[(1-\phi)\overline{\mathbf{u}}_s] + \mathbf{c}_s : \mathbf{E} \tag{A8}$$

and

$$\phi\overline{\mathbf{T}}_f = \mathbf{c}_f : \nabla(\phi\overline{\mathbf{u}}_f) - \mathbf{c}_f : \mathbf{E}. \tag{A9}$$

Since P is an exact differential, we have the following constraints:

$$\frac{\partial^2 P}{\partial\nabla\overline{\mathbf{u}}_f\partial\nabla\overline{\mathbf{u}}_s} = \frac{1}{2}\frac{\partial[(1-\phi)\overline{\mathbf{T}}_s]}{\partial\nabla\overline{\mathbf{u}}_f} = \frac{\partial^2 P}{\partial\nabla\overline{\mathbf{u}}_s\partial\nabla\overline{\mathbf{u}}_f} = \frac{1}{2}\frac{\partial(\phi\overline{\mathbf{T}}_f)}{\partial\nabla\overline{\mathbf{u}}_s}\,, \tag{A10}$$

$$\frac{\partial^2 P}{\partial\overline{\mathbf{u}}_f\partial\overline{\mathbf{u}}_s} = -\frac{1}{2}\frac{\partial(\overline{\mathbf{T}}_f\cdot\nabla\phi)}{\partial\overline{\mathbf{u}}_f} = \frac{\partial^2 P}{\partial\overline{\mathbf{u}}_s\partial\overline{\mathbf{u}}_f} = \frac{1}{2}\frac{\partial(\overline{\mathbf{T}}_f\cdot\nabla\phi)}{\partial\overline{\mathbf{u}}_s}\,, \tag{A11}$$

$$\frac{\partial^2 P}{\partial\nabla\overline{\mathbf{u}}_f\partial\overline{\mathbf{u}}_s} = -\frac{1}{2}\frac{\partial(\overline{\mathbf{T}}_f\cdot\nabla\phi)}{\partial\nabla\overline{\mathbf{u}}_f} = \frac{\partial^2 P}{\partial\overline{\mathbf{u}}_s\partial\nabla\overline{\mathbf{u}}_f} = \frac{1}{2}\frac{\partial(\phi\overline{\mathbf{T}}_f)}{\partial\overline{\mathbf{u}}_s}\,, \tag{A12}$$

$$\frac{\partial^2 P}{\partial\overline{\mathbf{u}}_f\partial\nabla\overline{\mathbf{u}}_s} = \frac{1}{2}\frac{\partial[(1-\phi)\overline{\mathbf{T}}_s]}{\partial\overline{\mathbf{u}}_f} = \frac{\partial^2 P}{\partial\nabla\overline{\mathbf{u}}_s\partial\overline{\mathbf{u}}_f} = \frac{1}{2}\frac{\partial(\overline{\mathbf{T}}_f\cdot\nabla\phi)}{\partial\nabla\overline{\mathbf{u}}_s}\,. \tag{A13}$$

Using the constraints (A10)–(A13) together with (A7), (A8) and (A9) it may be shown that

$$\boldsymbol{\alpha}_2 = \mathbf{c}_f^{-1} : \mathbf{c}_f + \phi^{-1}\mathbf{c}_s^{-1} : \mathbf{c}_f : \boldsymbol{\alpha}_1, \tag{A14}$$

$$\boldsymbol{\alpha}_3 = -\mathbf{c}_s^{-1} : \mathbf{c}_f : \boldsymbol{\alpha}_1, \tag{A15}$$

$$\boldsymbol{\alpha}_4 = -\phi^{-1}\mathbf{c}_s^{-1} : \mathbf{c}_f : \boldsymbol{\alpha}_1. \tag{A16}$$

This implies that

$$\begin{aligned} P = {} & \frac{1}{2}(\nabla\overline{\mathbf{u}}_s) : [(1-\phi)\mathbf{c}_s - \phi\mathbf{c}_s : \boldsymbol{\alpha}] : (\nabla\overline{\mathbf{u}}_s) + \frac{1}{2}(\nabla\overline{\mathbf{u}}_f) : [\phi(\mathbf{c}_f - \mathbf{c}_f : \mathbf{c}_s^{-1} : \mathbf{c}_f : \boldsymbol{\alpha})] : (\nabla\overline{\mathbf{u}}_f) \\ & + (\nabla\overline{\mathbf{u}}_s) : (\phi\mathbf{c}_f : \boldsymbol{\alpha}) : (\nabla\overline{\mathbf{u}}_f) + (\nabla\overline{\mathbf{u}}_s) : (\mathbf{c}_f : \boldsymbol{\alpha}) : (\overline{\mathbf{u}}_f - \overline{\mathbf{u}}_s)\nabla\phi \\ & + (\nabla\overline{\mathbf{u}}_f) : (\mathbf{c}_f - \mathbf{c}_f : \mathbf{c}_s^{-1} : \mathbf{c}_f : \boldsymbol{\alpha}) : (\overline{\mathbf{u}}_f - \overline{\mathbf{u}}_s)\nabla\phi \\ & + \frac{1}{2}\phi^{-1}(\nabla\phi)(\overline{\mathbf{u}}_f - \overline{\mathbf{u}}_s) : (\mathbf{c}_f - \mathbf{c}_f : \mathbf{c}_s^{-1} : \mathbf{c}_f : \boldsymbol{\alpha}) : (\overline{\mathbf{u}}_f - \overline{\mathbf{u}}_s)\nabla\phi, \end{aligned} \tag{A17}$$

and

$$\mathbf{E} = -\phi\boldsymbol{\alpha} : \nabla\overline{\mathbf{u}}_s + \mathbf{c}_s^{-1} : (\mathbf{c}_s - \mathbf{c}_f : \boldsymbol{\alpha}) : \overline{\mathbf{u}}_s\nabla\phi + \mathbf{c}_s^{-1} : \mathbf{c}_f : \boldsymbol{\alpha} : \nabla(\phi\overline{\mathbf{u}}_f), \tag{A18}$$

where we have introduced the fourth-order tensor

$$\boldsymbol{\alpha} = -\phi^{-1}\boldsymbol{\alpha}_1. \tag{A19}$$

We can now see that the result (A18) is entirely consistent with (80).

APPENDIX B: SPATIAL DISCRETIZATION

As in a classical FEM, the mesh in the SEM involves a subdivision of the model volume Ω into n_{el} non-overlapping elements Ω_e, $e = 1, \ldots, n_{el}$. Each of these elements is mapped to a reference domain $[-1, 1]^{n_d}$ (a square in 2-D, $n_d = 2$, and a cube in 3-D, $n_d = 3$), such that there is a unique relationship between a point $\mathbf{x}$ within Ω_e and a GLL point $\boldsymbol{\xi} = (\xi, \eta, \zeta)$ in the reference domain. Details regarding the discretization may be found in Komatitsch & Tromp (1999) and Komatitsch *et al.* (2005). In the following we give expressions for the solid and fluid mass matrices as well as the viscous damping matrix resulting from integration at the elemental level of (224) and (225).

B1 Solid mass matrix

Using the spectral-element discretization scheme, the mass matrix for the skeleton part at the elemental level (224) may be integrated as

$$\int_{\Omega_e} \overline{\rho}\tilde{u}_k \partial_t^2 \overline{u}_{sk} \mathrm{d}^3\mathbf{x} \approx \sum_{\alpha,\beta,\gamma} \overline{\rho}^{\alpha\beta\gamma} w_\alpha w_\beta w_\gamma J_e^{\alpha\beta\gamma} \sum_{\alpha',\beta',\gamma'} l_{\alpha'}(\xi_\alpha) l_{\beta'}(\eta_\beta) l_{\gamma'}(\zeta_\gamma) \sum_{\alpha'',\beta'',\gamma''} l_{\alpha''}(\xi_\alpha) l_{\beta''}(\eta_\beta) l_{\gamma''}(\zeta_\gamma) \partial_t^2 \overline{u}_{sk}^{\alpha''\beta''\gamma''}(t), \tag{B1}$$

where $\tilde{\mathbf{u}}$ is a test vector, w_α denote the weights associated with the GLL points of integration, $J_e^{\alpha\beta\gamma} = J_e(\xi_\alpha, \eta_\beta, \zeta_\gamma)$ is the Jacobian evaluated at the GLL point $(\xi_\alpha, \eta_\beta, \zeta_\gamma)$, $\overline{\rho}^{\alpha\beta\gamma} = \overline{\rho}(\xi_\alpha, \eta_\beta, \zeta_\gamma)$ denotes the density evaluated at a GLL point, and l_α is a Lagrange polynomial. Using the property $l_\alpha(\xi_{\alpha'}) = \delta_{\alpha\alpha'}$ of the Lagrange polynomials, (B1) simplifies to

$$\int_{\Omega_e} \overline{\rho}\tilde{u}_k \partial_t^2 \overline{u}_{sk} \mathrm{d}^3\mathbf{x} \approx \sum_{\alpha,\beta,\gamma} \overline{\rho}^{\alpha\beta\gamma} w_\alpha w_\beta w_\gamma J_e^{\alpha\beta\gamma} \partial_t^2 \overline{u}_{sk}^{\alpha\beta\gamma}(t). \tag{B2}$$

Note that the term $\overline{\rho}^{\alpha\beta\gamma} w_\alpha w_\beta w_\gamma J_e^{\alpha\beta\gamma}$ is a multiplicative factor, such that the elemental mass matrix is diagonal. Note also that $\overline{\rho} = (1-\phi)\rho_s + \phi\rho_f$ can vary from one gridpoint to an other, thus allowing for material gradients within an element (Komatitsch & Tromp 2002).

The second term can also be interpreted as a mass matrix, accommodating the relative acceleration of the fluid, and may be similarly integrated as

$$\int_{\Omega_e} \rho_f \tilde{u_k} \partial_t^2 \overline{w}_k \mathrm{d}^3\mathbf{x} \approx \sum_{\alpha,\beta,\gamma} \rho_f^{\alpha\beta\gamma} w_\alpha w_\beta w_\gamma J_e^{\alpha\beta\gamma} \partial_t^2 \overline{w}_k^{\alpha\beta\gamma}(t), \tag{B3}$$

where $\rho_f^{\alpha\beta\gamma} w_\alpha w_\beta w_\gamma J_e^{\alpha\beta\gamma}$ is a simple multiplicative factor, leading to a diagonal matrix.

B2 Fluid mass matrix

The first term on the left-hand side of (225) is a mass matrix relative to the fluid. It may be integrated as

$$\int_{\Omega_e} m\tilde{w}_k \partial_t^2 \overline{w}_k \mathrm{d}^3\mathbf{x} \approx \sum_{\alpha,\beta,\gamma} m^{\alpha\beta\gamma} w_\alpha w_\beta w_\gamma J_e^{\alpha\beta\gamma} \partial_t^2 \overline{w}_k^{\alpha\beta\gamma}(t), \tag{B4}$$

where $m^{\alpha\beta\gamma} w_\alpha w_\beta w_\gamma J_e^{\alpha\beta\gamma}$ is again a simple multiplicative factor and $m = \rho_f c/\phi$ can vary from one gridpoint to an other.

The second term on the left hand side may be interpreted as a second mass matrix relative to the skeleton and is integrated as

$$\int_{\Omega_e} \rho_f \tilde{w}_k \partial_t^2 \overline{u}_{sk} \mathrm{d}^3\mathbf{x} \approx \sum_{\alpha,\beta,\gamma} \rho_f^{\alpha\beta\gamma} w_\alpha w_\beta w_\gamma J_e^{\alpha\beta\gamma} \partial_t^2 \overline{u}_{sk}^{\alpha\beta\gamma}(t). \tag{B5}$$

This mass matrix is also diagonal.

B3 Viscous damping matrix

The third term on the left hand side of (225) is the viscous damping force and may be diagonally integrated as

$$\int_{\Omega_e} \eta_f \tilde{w}_k \sum_j (k^{-1})_{kj} \partial_t \overline{w}_j \mathrm{d}^3\mathbf{x} \approx \sum_{\alpha,\beta,\gamma} \eta_f^{\alpha\beta\gamma} w_\alpha w_\beta w_\gamma J_e^{\alpha\beta\gamma} \sum_j (k^{-1})_{kj}^{\alpha\beta\gamma} \partial_t \overline{w}_j^{\alpha\beta\gamma}(t). \tag{B6}$$

APPENDIX C: GLOBAL SYSTEM MATRICES

Let us have a closer look at the global system (229) and the corresponding global system matrices (230)–(233). Denoting the elements of the global diagonal mass matrices by $\mathbf{M}_1 = [M_{1(IJ)}]$, $\mathbf{M}_2 = [M_{2(IJ)}]$, and $\mathbf{M}_3 = [M_{3(IJ)}]$, we have

$$\begin{aligned} M_{1(II)} &= \sum_{(\alpha,\beta,\gamma,\Omega_e)\to(I)} w_\alpha w_\beta w_\gamma J_e \overline{\rho}, \\ M_{2(II)} &= \sum_{(\alpha,\beta,\gamma,\Omega_e)\to(I)} w_\alpha w_\beta w_\gamma J_e \rho_f, \\ M_{3(II)} &= \sum_{(\alpha,\beta,\gamma,\Omega_e)\to(I)} w_\alpha w_\beta w_\gamma J_e \rho_f c/\phi, \end{aligned} \tag{C1}$$

where we have omitted the indices $\alpha\ \beta\ \gamma$ on the Jacobian and the model parameters to avoid clutter. As a result we find

$$\begin{aligned} M_{(II)}^s &= M_{1(II)} - M_{2(II)}^2 M_{3(II)}^{-1} = \sum_{(\alpha,\beta,\gamma,\Omega_e)\to(I)} w_\alpha w_\beta w_\gamma J_e \left(\overline{\rho} - \frac{\phi}{c}\rho_f\right), \\ M_{(II)}^f &= M_{3(II)} - M_{2(II)}^2 M_{1(II)}^{-1} = \sum_{(\alpha,\beta,\gamma,\Omega_e)\to(I)} w_\alpha w_\beta w_\gamma J_e \left(\frac{\overline{\rho}\rho_f c - \phi\rho_f^2}{\phi\overline{\rho}}\right). \end{aligned} \tag{C2}$$

Similarly, we can evaluate the elements of $\boldsymbol{\mathcal{D}}^s = \mathbf{D}^s\dot{\mathbf{W}}$ and $\boldsymbol{\mathcal{D}}^f = \mathbf{D}^f\dot{\mathbf{W}}$ as

$$\boldsymbol{\mathcal{D}}^s_{(I)} = -\sum_{(\alpha,\beta,\gamma,\Omega_e)\to(I)} \frac{\phi^{\alpha\beta\gamma}}{c^{\alpha\beta\gamma}}\eta_f w_\alpha w_\beta w_\gamma J_e \sum_j (k^{-1})_{kj}\partial_t \overline{w}_j(t), \tag{C3}$$

and

$$\boldsymbol{\mathcal{D}}^f_{(I)} = \sum_{(\alpha,\beta,\gamma,\Omega_e)\to(I)} \eta_f w_\alpha w_\beta w_\gamma J_e \sum_j (k^{-1})_{kj}\partial_t \overline{w}_j(t). \tag{C4}$$

The elements of $\boldsymbol{\mathcal{T}}^s_s = \mathbf{K}^s_s\mathbf{U}$, $\boldsymbol{\mathcal{T}}^s_f = \mathbf{K}^s_f\mathbf{W}$, $\boldsymbol{\mathcal{T}}^f_s = \mathbf{K}^f_s\mathbf{U}$, and $\boldsymbol{\mathcal{T}}^f_f = \mathbf{K}^f_f\mathbf{W}$ are:

$$\begin{aligned}
\boldsymbol{\mathcal{T}}^s_{s(I)} = \sum_{(\alpha,\beta,\gamma,\Omega_e)\to(I)} \Bigg[& w_\beta w_\gamma \sum_{\alpha'} w_{\alpha'} J_e^{\alpha'\beta\gamma} \frac{\partial l_\alpha(\xi_{\alpha'})}{\partial\xi} \sum_j G^{\alpha'\beta\gamma}_{kjil} \frac{1}{2}(\partial_i \overline{u}^{\alpha'\beta\gamma}_{sl} + \partial_l \overline{u}^{\alpha'\beta\gamma}_{si})\partial_j\xi \\
& + w_\alpha w_\gamma \sum_{\beta'} w_{\beta'} J_e^{\alpha\beta'\gamma} \frac{\partial l_\beta(\xi_{\beta'})}{\partial\eta} \sum_j G^{\alpha\beta'\gamma}_{kjil} \frac{1}{2}(\partial_i \overline{u}^{\alpha\beta'\gamma}_{sl} + \partial_l \overline{u}^{\alpha\beta'\gamma}_{si})\partial_j\eta \\
& + w_\alpha w_\beta \sum_{\gamma'} w_{\gamma'} J_e^{\alpha\beta\gamma'} \frac{\partial l_\gamma(\xi_{\gamma'})}{\partial\zeta} \sum_j G^{\alpha\beta\gamma'}_{kjil} \frac{1}{2}(\partial_i \overline{u}^{\alpha\beta\gamma'}_{sl} + \partial_l \overline{u}^{\alpha\beta\gamma'}_{si})\partial_j\zeta \Bigg] \\
& - \sum_{(\alpha,\beta,\gamma,\Omega_e)\to(I)} \frac{\phi^{\alpha\beta\gamma}}{c^{\alpha\beta\gamma}} \Bigg[w_\beta w_\gamma \sum_{\alpha'} w_{\alpha'} J_e^{\alpha'\beta\gamma} \frac{\partial l_\alpha(\xi_{\alpha'})}{\partial\xi} \sum_j C^{\alpha'\beta\gamma}\partial_i \overline{u}^{\alpha'\beta\gamma}_{si}\delta_{kj}\partial_j\xi \\
& + w_\alpha w_\gamma \sum_{\beta'} w_{\beta'} J_e^{\alpha\beta'\gamma} \frac{\partial l_\beta(\xi_{\beta'})}{\partial\eta} \sum_j C^{\alpha\beta'\gamma}\partial_i \overline{u}^{\alpha\beta'\gamma}_{si}\delta_{kj}\partial_j\eta \\
& + w_\alpha w_\beta \sum_{\gamma'} w_{\gamma'} J_e^{\alpha\beta\gamma'} \frac{\partial l_\gamma(\xi_{\gamma'})}{\partial\zeta} \sum_j C^{\alpha\beta\gamma'}\partial_i \overline{u}^{\alpha\beta\gamma'}_{si}\delta_{kj}\partial_j\zeta \Bigg],
\end{aligned} \tag{C5}$$

$$\begin{aligned}
\boldsymbol{\mathcal{T}}^s_{f(I)} = \sum_{(\alpha,\beta,\gamma,\Omega_e)\to(I)} \Bigg[& w_\beta w_\gamma \sum_{\alpha'} w_{\alpha'} J_e^{\alpha'\beta\gamma} \frac{\partial l_\alpha(\xi_{\alpha'})}{\partial\xi} \sum_j C^{\alpha'\beta\gamma}\partial_i \overline{w}^{\alpha'\beta\gamma}_i \delta_{kj}\partial_j\xi \\
& + w_\alpha w_\gamma \sum_{\beta'} w_{\beta'} J_e^{\alpha\beta'\gamma} \frac{\partial l_\beta(\xi_{\beta'})}{\partial\eta} \sum_j C^{\alpha'\beta\gamma}\partial_i \overline{w}^{\alpha'\beta\gamma}_i \delta_{kj}\partial_j\eta \\
& + w_\alpha w_\beta \sum_{\gamma'} w_{\gamma'} J_e^{\alpha\beta\gamma'} \frac{\partial l_\gamma(\xi_{\gamma'})}{\partial\zeta} \sum_j C^{\alpha'\beta\gamma}\partial_i \overline{w}^{\alpha'\beta\gamma}_i \delta_{kj}\partial_j\zeta \Bigg] \\
& - \sum_{(\alpha,\beta,\gamma,\Omega_e)\to(I)} \frac{\phi^{\alpha\beta\gamma}}{c^{\alpha\beta\gamma}} \Bigg[w_\beta w_\gamma \sum_{\alpha'} w_{\alpha'} J_e^{\alpha'\beta\gamma} \frac{\partial l_\alpha(\xi_{\alpha'})}{\partial\xi} \sum_j M^{\alpha'\beta\gamma}\partial_i \overline{w}^{\alpha'\beta\gamma}_i \delta_{kj}\partial_j\xi \\
& + w_\alpha w_\gamma \sum_{\beta'} w_{\beta'} J_e^{\alpha\beta'\gamma} \frac{\partial l_\beta(\xi_{\beta'})}{\partial\eta} \sum_j M^{\alpha\beta'\gamma}\partial_i \overline{w}^{\alpha\beta'\gamma}_i \delta_{kj}\partial_j\eta \\
& + w_\alpha w_\beta \sum_{\gamma'} w_{\gamma'} J_e^{\alpha\beta\gamma'} \frac{\partial l_\gamma(\xi_{\gamma'})}{\partial\zeta} \sum_j M^{\alpha\beta\gamma'}\partial_i \overline{w}^{\alpha\beta\gamma'}_i \delta_{kj}\partial_j\zeta \Bigg],
\end{aligned} \tag{C6}$$

$$
\begin{aligned}
\boldsymbol{\mathcal{T}}^{f}_{s(I)} = \sum_{(\alpha,\beta,\gamma,\Omega_e)\to(I)} \Bigg[& w_\beta w_\gamma \sum_{\alpha'} w_{\alpha'} J_e^{\alpha'\beta\gamma} \frac{\partial l_\alpha(\xi_{\alpha'})}{\partial \xi} \sum_j C^{\alpha'\beta\gamma} \partial_i \overline{u}_{si}^{\alpha'\beta\gamma} \delta_{kj} \partial_j \xi \\
& + w_\alpha w_\gamma \sum_{\beta'} w_{\beta'} J_e^{\alpha\beta'\gamma} \frac{\partial l_\beta(\xi_{\beta'})}{\partial \eta} \sum_j C^{\alpha'\beta\gamma} \partial_i \overline{u}_{si}^{\alpha'\beta\gamma} \delta_{kj} \partial_j \eta \\
& + w_\alpha w_\beta \sum_{\gamma'} w_{\gamma'} J_e^{\alpha\beta\gamma'} \frac{\partial l_\gamma(\xi_{\gamma'})}{\partial \zeta} \sum_j C^{\alpha'\beta\gamma} \partial_i \overline{u}_{si}^{\alpha'\beta\gamma} \delta_{kj} \partial_j \zeta \Bigg] \\
& - \sum_{(\alpha,\beta,\gamma,\Omega_e)\to(I)} \frac{\rho_f^{\alpha\beta\gamma}}{\overline{\rho}^{\alpha\beta\gamma}} \Bigg[w_\beta w_\gamma \sum_{\alpha'} w_{\alpha'} J_e^{\alpha'\beta\gamma} \frac{\partial l_\alpha(\xi_{\alpha'})}{\partial \xi} \sum_j G^{\alpha'\beta\gamma}_{kjil} \frac{1}{2} (\partial_i \overline{u}_{sl}^{\alpha'\beta\gamma} + \partial_l \overline{u}_{si}^{\alpha'\beta\gamma}) \partial_j \xi \\
& + w_\alpha w_\gamma \sum_{\beta'} w_{\beta'} J_e^{\alpha\beta'\gamma} \frac{\partial l_\beta(\xi_{\beta'})}{\partial \eta} \sum_j G^{\alpha\beta'\gamma}_{kjil} \frac{1}{2} (\partial_i \overline{u}_{sl}^{\alpha\beta'\gamma} + \partial_l \overline{u}_{si}^{\alpha\beta'\gamma}) \partial_j \eta \\
& + w_\alpha w_\beta \sum_{\gamma'} w_{\gamma'} J_e^{\alpha\beta\gamma'} \frac{\partial l_\gamma(\xi_{\gamma'})}{\partial \zeta} \sum_j G^{\alpha\beta\gamma'}_{kjil} \frac{1}{2} (\partial_i \overline{u}_{sl}^{\alpha\beta\gamma'} + \partial_l \overline{u}_{si}^{\alpha\beta\gamma'}) \partial_j \zeta \Bigg],
\end{aligned} \tag{C7}
$$

and

$$
\begin{aligned}
\boldsymbol{\mathcal{T}}^{f}_{f(I)} = \sum_{(\alpha,\beta,\gamma,\Omega_e)\to(I)} \Bigg[& w_\beta w_\gamma \sum_{\alpha'} w_{\alpha'} J_e^{\alpha'\beta\gamma} \frac{\partial l_\alpha(\xi_{\alpha'})}{\partial \xi} \sum_j M^{\alpha'\beta\gamma} \partial_i \overline{w}_i^{\alpha'\beta\gamma} \delta_{kj} \partial_j \xi \\
& + w_\alpha w_\gamma \sum_{\beta'} w_{\beta'} J_e^{\alpha\beta'\gamma} \frac{\partial l_\beta(\xi_{\beta'})}{\partial \eta} \sum_j M^{\alpha'\beta\gamma} \partial_i \overline{w}_i^{\alpha'\beta\gamma} \delta_{kj} \partial_j \eta \\
& + w_\alpha w_\beta \sum_{\gamma'} w_{\gamma'} J_e^{\alpha\beta\gamma'} \frac{\partial l_\gamma(\xi_{\gamma'})}{\partial \zeta} \sum_j M^{\alpha'\beta\gamma} \partial_i \overline{w}_i^{\alpha'\beta\gamma} \delta_{kj} \partial_j \zeta \Bigg] \\
& - \sum_{(\alpha,\beta,\gamma,\Omega_e)\to(I)} \frac{\rho_f^{\alpha\beta\gamma}}{\overline{\rho}^{\alpha\beta\gamma}} \Bigg[w_\beta w_\gamma \sum_{\alpha'} w_{\alpha'} J_e^{\alpha'\beta\gamma} \frac{\partial l_\alpha(\xi_{\alpha'})}{\partial \xi} \sum_j C^{\alpha'\beta\gamma} \partial_i \overline{w}_i^{\alpha'\beta\gamma} \delta_{kj} \partial_j \xi \\
& + w_\alpha w_\gamma \sum_{\beta'} w_{\beta'} J_e^{\alpha\beta'\gamma} \frac{\partial l_\beta(\xi_{\beta'})}{\partial \eta} \sum_j C^{\alpha\beta'\gamma} \partial_i \overline{w}_i^{\alpha\beta'\gamma} \delta_{kj} \partial_j \eta \\
& + w_\alpha w_\beta \sum_{\gamma'} w_{\gamma'} J_e^{\alpha\beta\gamma'} \frac{\partial l_\gamma(\xi_{\gamma'})}{\partial \zeta} \sum_j C^{\alpha\beta\gamma'} \partial_i \overline{w}_i^{\alpha\beta\gamma'} \delta_{kj} \partial_j \zeta \Bigg].
\end{aligned} \tag{C8}
$$

This requires knowledge of the partial derivatives of $\overline{\mathbf{u}}_s$ and $\overline{\mathbf{w}}$ at the GLL points. We have

$$
\partial_i \overline{u}_{sj}(\mathbf{x}(\xi_\alpha, \eta_\beta, \zeta_\gamma), t) = \left[\sum_\sigma \overline{u}_{sj}^{\sigma\beta\gamma}(t) \frac{\partial l_\sigma(\xi_\alpha)}{\partial \xi} \right] \partial_i \xi + \left[\sum_\sigma \overline{u}_{sj}^{\alpha\sigma\gamma}(t) \frac{\partial l_\sigma(\eta_\beta)}{\partial \eta} \right] \partial_i \eta + \left[\sum_\sigma \overline{u}_{sj}^{\alpha\beta\sigma}(t) \frac{\partial l_\sigma(\zeta_\gamma)}{\partial \zeta} \right] \partial_i \zeta, \tag{C9}
$$

and

$$
\partial_i \overline{w}_j(\mathbf{x}(\xi_\alpha, \eta_\beta, \zeta_\gamma), t) = \left[\sum_\sigma \overline{w}_j^{\sigma\beta\gamma}(t) \frac{\partial l_\sigma(\xi_\alpha)}{\partial \xi} \right] \partial_i \xi + \left[\sum_\sigma \overline{w}_j^{\alpha\sigma\gamma}(t) \frac{\partial l_\sigma(\eta_\beta)}{\partial \eta} \right] \partial_i \eta + \left[\sum_\sigma \overline{w}_j^{\alpha\beta\sigma}(t) \frac{\partial l_\sigma(\zeta_\gamma)}{\partial \zeta} \right] \partial_i \zeta. \tag{C10}
$$

The elements for the source vectors are

$$
\begin{aligned}
F^s_{(I)} = \left(1 - \frac{\phi^{\alpha_s\beta_s\gamma_s}}{c^{\alpha_s\beta_s\gamma_s}} \right) S(t) \sum_{\sigma,\tau,\nu}^{n_l} & l_\sigma(\xi_{\alpha_s}) l_\tau(\eta_{\beta_s}) l_\nu(\zeta_{\gamma_s}) [Q_{k1}^{\sigma\tau\nu} l'_\alpha(\xi_{\alpha_s}) l_\beta(\eta_{\beta_s}) l_\gamma(\zeta_{\gamma_s}) + Q_{k2}^{\sigma\tau\nu} l_\alpha(\xi_{\alpha_s}) l'_\beta(\eta_{\beta_s}) l_\gamma(\zeta_{\gamma_s}) \\
& + Q_{k3}^{\sigma\tau\nu} l_\alpha(\xi_{\alpha_s}) l_\beta(\eta_{\beta_s}) l'_\gamma(\zeta_{\gamma_s})],
\end{aligned} \tag{C11}
$$

and

$$
\begin{aligned}
F^f_{(I)} = \left(1 - \frac{\rho_f^{\alpha_s\beta_s\gamma_s}}{\overline{\rho}^{\alpha_s\beta_s\gamma_s}} \right) S(t) \sum_{\sigma,\tau,\nu}^{n_l} & l_\sigma(\xi_{\alpha_s}) l_\tau(\eta_{\beta_s}) l_\nu(\zeta_{\gamma_s}) [Q_{k1}^{\sigma\tau\nu} l'_\alpha(\xi_{\alpha_s}) l_\beta(\eta_{\beta_s}) l_\gamma(\zeta_{\gamma_s}) + Q_{k2}^{\sigma\tau\nu} l_\alpha(\xi_{\alpha_s}) l'_\beta(\eta_{\beta_s}) l_\gamma(\zeta_{\gamma_s}) \\
& + Q_{k3}^{\sigma\tau\nu} l_\alpha(\xi_{\alpha_s}) l_\beta(\eta_{\beta_s}) l'_\gamma(\zeta_{\gamma_s})],
\end{aligned} \tag{C12}
$$

where $\mathbf{x}(\xi_{\alpha_s}, \eta_{\beta_s}, \zeta_{\gamma_s}) = \mathbf{x}_s$ and $Q_{ki} = \sum_j M_{kj} \partial_j \xi_i$. The system (229) thus reduces to

$$
\mathbf{M}^s \ddot{\mathbf{U}} = \mathrm{RHS}^s, \tag{C13}
$$

$$
\mathbf{M}^f \ddot{\mathbf{W}} = \mathrm{RHS}^f, \tag{C14}
$$

where

$$\mathrm{RHS}^s_{(I)} = F^s_{(I)} - \left[\boldsymbol{\mathcal{D}}^s_{(I)} + \boldsymbol{\mathcal{T}}^s_{s(I)} + \boldsymbol{\mathcal{T}}^s_{f(I)}\right], \tag{C15}$$

$$\mathrm{RHS}^f_{(I)} = F^f_{(I)} - \left[\boldsymbol{\mathcal{D}}^f_{(I)} + \boldsymbol{\mathcal{T}}^f_{s(I)} + \boldsymbol{\mathcal{T}}^f_{f(I)}\right]. \tag{C16}$$

The mass matrices being diagonal, these linear equations may be solved by simple division:

$$\ddot{U}_{(I)} = M^{s-1}_{(II)}\mathrm{RHS}^s_{(I)}, \tag{C17}$$

$$\ddot{W}_{(I)} = M^{f-1}_{(II)}\mathrm{RHS}^f_{(I)}. \tag{C18}$$